

Rinc

(NASA-CR-181548) AN INTEGRATED STUDY OF
STRUCTURES, AERODYNAMICS AND CONTROLS ON THE
FORWARD SWEPT WING X-29A AND THE OBLIQUE
WING RESEARCH AIRCRAFT Final Report (Kansas
Univ. Center for Research) 128 p CSCL 01C G3/05

N88-12466

Unclass
0111212

THE UNIVERSITY OF KANSAS CENTER FOR RESEARCH, INC.
2291 Irving Hill Drive-Campus West
Lawrence, Kansas 66045

FINAL CONTRACTOR REPORT

For

NASA COOPERATIVE AGREEMENT
NCC 2 - 396

AN INTEGRATED STUDY OF STRUCTURES, AERODYNAMICS
AND CONTROLS ON THE FORWARD SWEPT WING X-29A and
THE OBLIQUE WING RESEARCH AIRCRAFT

by

KENNETH S. DAWSON

PAUL E. FORTIN

UNIVERSITY OF KANSAS
CENTER FOR RESEARCH

DECEMBER 87

ABSTRACT

This report presents the results of an integrated study of structures, aerodynamics, and controls using the STARS program on two advanced airplane configurations, the Forward Swept Wing X-29A, and the Oblique Wing Research Aircraft. The results of various analyses performed for this project are compared to other verified results to illustrate the effectiveness of an integrated approach.

The results presented for the X-29A include finite element modeling, free vibration analyses, unsteady aerodynamic calculations, flutter/divergence analyses, and an aeroservo-elastic controls analysis. The STARS analytical free vibration results and the results of the ground vibration survey performed at NASA are presented and compared for the symmetric and anti-symmetric cases of the X-29A. Good correlation is shown between the STARS' and the ground vibration survey's natural frequencies, as most differences were less than 8%. For example, the wing first bending mode for the symmetric case was analytically calculated at 8.96 hz, a 4.1% difference of the 8.61 hz ground vibration test value. Subsonic generalized forces were then obtained by unsteady aerodynamic calculations using a doublet lattice method. Utilizing the STARS analytical generalized force, stiffness, and mass matrices, flutter and divergence analyses were performed for the symmetric and anti-symmetric cases of the X-29A. The flutter/divergence results are correlated and illustrated in V-g diagrams and root-locus plots for three solution techniques, the k-method, the p-k method, and a state-space method. The flutter solutions for the symmetric case correlate well for all three solution techniques. For example, all three methods predict the symmetric canard pitch mode to diverge: the k method at 913 kts, the p-k method at 920 kts, and the state-space method at 918 kts. The solutions for the anti-symmetric case, however, show good correlation only for the k and state-space methods. The anti-symmetric canard pitch was predicted to diverge by all three methods, however, the p-k method was 49% higher than the k method, and 67% higher than the state-space method. Additional flutter analyses were performed on the X-29A to determine the effect, if any, of including the rigid body modes in the solutions. Results are graphed and presented for a select few modes of the anti-symmetric case. The latter analysis indicates that coupling occurred between the rigid body modes and the elastic modes, effecting the flutter and divergence characteristics.

The aeroservoelastic controls analysis performed on the X-29A include open and closed loop responses using the analog reversion mode of the longitudinal flight control system. The open loop analyses are performed to check the dynamic stability of the airplane, while the

primary purpose of the closed loop analyses is to determine if any adverse airframe/control coupling occurs. The STARS results, which utilize analytical mode shapes to account for the flexible effects, are presented and compared to results which utilize ground vibration mode shapes. The open loop analyses are performed including and excluding the notch filters. Without the notch filters in the analysis using the ground vibration mode shapes, the airplane does not meet the requirements of 'no gain crossovers at resonance frequencies and a gain margin of 6 dB past the first natural frequency,' as expected. The STARS results (using the analytical mode shapes), however, show that this requirement is met. Beyond this, the STARS and ground test results show good gain and phase margin correlation for all analyses.

Additionally, the STARS analytical closed loop damping and frequency values showed very good correlation to the flight test results performed at NASA.

The tasks performed on the Oblique Wing Research Aircraft include finite element modeling and free vibration analyses. The finite element model was generated by the conversion of a contractor's NASTRAN model to a STARS model. An unique attempt has been made to solve the OWRA free vibration problem by utilizing the detailed finite element model, thus circumventing the approximate dynamic reduction procedure. Extensive steps were taken to minimize the bandwidth of the problem since this involves the solution of a very large order eigenvalue problem. An attempt to renumber the nodes by hand showed that the STARS minimization technique was more efficient in minimizing the bandwidth due to the complexity of the wing and pivot. The STARS minimization technique arrived at a half-bandwidth of 648. The results of the finite element modeling, and a limited free vibration analysis are then presented.

TABLE OF CONTENTS

	<u>Page</u>
ABSTRACT.....	i
ACKNOWLEDGEMENTS.....	ii
LIST OF FIGURES.....	vi
LIST OF TABLES.....	x
LIST OF SYMBOLS AND ACRONYMS.....	xi
1. INTRODUCTION.....	1
1.1 BACKGROUND.....	1
1.2 PROJECT OBJECTIVE.....	2
1.3 PROJECT OVERVIEW.....	2
2. PROJECT ELEMENTS AND BACKGROUND.....	5
2.1 INTRODUCTION.....	5
2.2 STARS DESCRIPTION.....	5
2.3 DESCRIPTION OF THE X-29A.....	9
2.4 INTRODUCTION TO THE OWRA.....	12
3. X-29A ANALYSES AND RESULTS.....	16
3.1 INTRODUCTION.....	16
3.2 STRUCTURAL ANALYSIS OF THE X-29A.....	17
3.3 AERODYNAMIC MODELING OF THE X-29A.....	30
3.4 FLUTTER AND DIVERGENCE ANALYSES.....	34
3.4.1 <u>Theory</u>	34
3.4.2 <u>Correlation of Flutter/Divergence Analyses</u>	42
3.4.2.1 Symmetric Analyses.....	42
3.4.2.2 Anti-symmetric Analyses.....	56
3.4.2 <u>Conclusions</u>	74
3.5 AEROSERVOELASTIC CONTROLS ANALYSIS.....	75
3.5.1 <u>X-29A Flight Control System Description</u>	75

PRECEDING PAGE BLANK NOT FILMED

TABLE OF CONTENTS (Continued)

	Page
3.5.2 <u>Theory of Response Analyses</u>	78
3.5.3 <u>ASE Controls Analysis Results</u>	79
4. OBLIQUE WING RESEARCH AIRCRAFT ANALYSES AND RESULTS.....	93
4.1 INTRODUCTION.....	93
4.2 THE OWRA FINITE ELEMENT MODEL.....	93
4.3 OWRA BANDWIDTH MINIMIZATION.....	97
4.4 OWRA FREE VIBRATION RESULTS.....	98
5. PROJECT MANAGEMENT.....	100
5.1 INTRODUCTION.....	100
5.2 PROJECT MANAGEMENT.....	100
5.3 PROJECT SCOPE AND SCHEDULING.....	104
5.4 PROJECT BUDGET.....	106
6. CONCLUSIONS AND RECOMMENDATIONS.....	109
6.1 PROJECT REVIEW.....	109
6.2 X-29A CONCLUSIONS.....	110
6.3 PROPOSED FUTURE RESEARCH FOR THE X-29A.....	112
6.4 OWRA CONCLUSIONS.....	112
6.5 PROPOSED FUTURE RESEARCH FOR THE OWRA.....	113
7. REFERENCES.....	114

LIST OF FIGURES

<u>Number</u>	<u>Title</u>	<u>Page</u>
2.1	Major Modules of STARS Computer Program.....	6
2.2	Simplified Flow Chart of STARS Computer Program.....	7
2.3	X-29A in Flight.....	9
2.4	Relaxed Static Stability of the X-29A.....	11
2.5	Artist's Rendition of the Proposed OWRA.....	12
2.6	Fundamental Aerodynamic Advantages of an Oblique Wing.....	15
2.7	Structural Advantage of an Oblique Wing.....	15
3.1	Finite Element Dynamics Model of the X-29A.....	18
3.2	X-29A Symmetric W1B Structural Mode Shape.....	21
3.3	X-29A Symmetric F1B Structural Mode Shape.....	22
3.4	X-29A Symmetric F2B Structural Mode Shape.....	23
3.5	X-29A Symmetric CP Structural Mode Shape.....	24
3.6	X-29A Symmetric W2B Structural Mode Shape.....	25
3.7	X-29A Anti-symmetric W1B Structural Mode Shape.....	26
3.8	X-29A Anti-symmetric Fin 1B Structural Mode Shape.....	27
3.9	X-29A Anti-symmetric CP Structural Mode Shape.....	28
3.10	X-29A Anti-symmetric W3B Structural Mode Shape.....	29
3.11	Aerodynamic Model Showing the Interpolating Lines of the Anti-symmetric X-29A.....	31
3.12	Doublet Lattice Unsteady Aerodynamic Paneling Idealization of the Symmetric and Anti-symmetric X-29A.....	32
3.13	Vertical Tail Interpolating Lines of the Anti-symmetric X-29A.....	33
3.14	Doublet Lattice Unsteady Aerodynamic Paneling Idealization for the X-29A Vertical Tail, Anti-symmetric Case.....	33
3.15	Comparative V-g Plot of the Symmetric X-29A W1B Mode.....	45

LIST OF FIGURES (Continued)

<u>Number</u>	<u>Title</u>	<u>Page</u>
3.16	Comparative V-g Plot of the Symmetric X-29A F1B Mode.....	46
3.17	Comparative V-g Plot of the Symmetric X-29A F2B Mode.....	47
3.18	Comparative V-g Plot of the Symmetric X-29A CP Mode.....	48
3.19	Comparative V-g Plot of the Symmetric X-29A W2B Mode.....	49
3.20	Comparative V-g Plot of the Symmetric X-29A W1T Mode.....	50
3.21	Comparative V-g Plot of the Symmetric X-29A CBP Mode.....	51
3.22	Comparative V-g Plot of the Symmetric X-29A W3B Mode.....	52
3.23	Symmetric X-29A Structural Root-Locus, State-space Method..	53
3.24	Symmetric X-29A Structural Root-Locus, k Method.....	54
3.25	Symmetric X-29A Structural Root-Locus, p-k Method.....	55
3.26	Comparative V-g Plot of the Anti-symmetric X-29A W1B Mode...	59
3.27	Comparative V-g Plot of the Anti-symmetric X-29A F1B Mode....	60
3.28	Comparative V-g Plot of the Anti-symmetric X-29A Fin 1B Mode..	61
3.29	Comparative V-g Plot of the Anti-symmetric X-29A CP Mode.....	62
3.30	Comparative V-g Plot of the Anti-symmetric X-29A W2B Mode....	63
3.31	Comparative V-g Plot of the Anti-symmetric X-29A W3B Mode....	64
3.32	Anti-symmetric X-29A Structural Root-Locus, Elastic Modes Only, State-space Method.....	65
3.33	Anti-symmetric X-29A Structural Root-Locus, Elastic Modes Only, k Method.....	66
3.34	Anti-symmetric X-29A Structural Root-Locus, Elastic Modes Only, p-k Method.....	67
3.35	Comparative V-g Plot of Anti-symmetric X-29A W1B Mode, Rigid Body Modes Included in Analysis.....	68
3.36	Comparative V-g Plot of Anti-symmetric X-29A CP Mode, Rigid Body Modes Included in Analysis.....	69

LIST OF FIGURES (Continued)

<u>Number</u>	<u>Title</u>	<u>Page</u>
3.37	Comparative V-g Plot of Anti-symmetric X-29A W3B Mode, Rigid Body Modes Included in Analysis.....	70
3.38	Anti-symmetric X-29A Structural Root-Locus, Rigid and Elastic Modes, State-space Method.....	71
3.39	Anti-symmetric X-29A Structural Root-Locus, Rigid and Elastic Modes, k Method.....	72
3.40	Anti-symmetric X-29A Structural Root-Locus, Rigid and Elastic Modes, p-k Method.....	73
3.41	X-29A Flight Control System.....	76
3.42	Analog Reversion Mode of the Longitudinal Flight Control System of the X-29A.....	77
3.43	Simplified Aircraft Feedback Control System.....	79
3.44	Frequency Response for STARS Rigid Body Open Loop Analysis.....	83
3.45	Frequency Plots for STARS Flexible Open Loop Analysis.....	84
3.46	Frequency Plots for SAEL Flexible Open Loop Analysis.....	85
3.47	Frequency Response for STARS Flexible Open Loop Analysis, Excluding Notch Filters.....	86
3.48	Frequency Response for SAEL Flexible Open Loop Analysis, Excluding Notch Filters.....	87
3.49	Frequency Response for STARS Rigid Body Closed Loop Analysis from Stick Position to Sensed Normal Force.....	88
3.50	Frequency Response for STARS Flexible Closed Loop Analysis from Stick Position to Sensed Normal Force.....	89
3.51	Frequency Plots for STARS Rigid Body Closed Loop Analysis from Stick Position to Sensed Pitch Rate, Excluding Notch Filters.....	90
3.52	Frequency Plots for STARS Flexible Closed Loop Analysis from Stick Position to Sensed Pitch Rate, Excluding Notch Filters.....	91
3.53	Frequency Plots for SAEL Flexible Closed Loop Analysis from Stick Position to Sensed Pitch Rate, Excluding Notch Filters.....	92

LIST OF FIGURES (Continued)

<u>Number</u>	<u>Title</u>	<u>Page</u>
4.1	STARS OWRA Finite Element Model of the Fuselage.....	94
4.2	STARS OWRA Finite Element Model of the Pivot Structure....	95
4.3	STARS OWRA Finite Element Model of the Wing.....	95
4.4	STARS Complete Finite Element Model of the OWRA.....	96
5.1	NASA Ames Research Center Organizational Chart.....	101
5.2	Project Management Organizational Chart.....	102
5.3	Project Schedule, Proposed and Actual.....	105

LIST OF TABLES

<u>Number</u>	<u>Title</u>	<u>Page</u>
2.1	Major Capabilities of the STARS Computer Program.....	6
2.2	Potential Advantages of a Forward Swept Wing.....	10
2.3	Technologies Incorporated on the X-29A.....	10
2.4	Characteristics of the Proposed OWRA.....	14
3.1	Free Vibration Results of the Symmetric X-29A.....	19
3.2	Free Vibration Results of the Anti-symmetric X-29A.....	20
3.3	Comparison of X-29A Flutter/Divergence Solutions, Symmetric Case.....	44
3.4	Comparison of X-29A Flutter/Divergence Solutions, Anti-symmetric Case.....	58
3.5	Comparison of X-29A Flutter/Divergence Solutions, Anti-symmetric Case, Including Rigid Body Modes.....	58
4.1	Results of the OWRA Free Vibration Analysis.....	99
5.1	Project Budget.....	107
5.2	Project Extension Budget.....	108

LIST OF SYMBOLS AND ACRONYMS

<u>Symbol</u>	<u>Definition</u>	<u>Dimension</u>
A	Aerodynamic influence coefficient matrix	ft ² /rad
AC	Aerodynamic center	% MAC
b	Wing span	ft
b	Reference semi-chord	ft, inches
C_D	Damping matrix	lb·sec/in
C_{D₀}	Zero lift drag coefficient	-----
g	Acceleration of gravity	ft/sec ²
k	Reduced frequency	rad
K	Generalized stiffness matrix	lb/in
L	Lift	lbs
M	Mach number	-----
M	Generalized mass matrix	lb·sec ² /in
p	Non-dimensional operator	-----
P	External forcing function matrix	lbs
q	Dynamic pressure	lbs/ft ²
q	Displacement vector	inches
Q	Generalized force matrix	lbs
s	Laplace variable	sec ⁻¹
S	Wing area	ft ²
V	Velocity	ft/sec
X	Length of wing	ft

LIST OF SYMBOLS AND ACRONYMS (Cont.)

GREEK SYMBOLS

β_j	Pade pole location	-----
δ	Control surface deflection	rad, deg
γ	Rate of decay (see Eqn 3.7)	-----
η	Generalized coordinate	-----
ρ	Air density	slugs/ft ³
ϕ	Mode shape eigenvector	-----
ω	Frequency	rad/sec

ACRONYMS

ARC	Ames Research Center
ASE	AeroServoElastic
CRINC	University of Kansas Center for Research, Inc.
DARPA	Defense Advanced Research Project Agency
DFRF	Dryden Flight Research Facility
FCS	Flight Control System
FEM	Finite Element Model
FSW	Forward Swept Wing
GAC	Grumman Aerospace Corporation
GM	Gain Margin
GVS	Ground Vibration Survey
HMC	Harvey Mudd College

LIST OF SYMBOLS AND ACRONYMS (Cont.)

ACRONYMS (Cont.)

NASA	National Aeronautics and Space Administration
NASTRAN	NASA Structural Analysis computer program
OWRA	Oblique Wing Research Aircraft
PM	Phase Margin
SAEL	Servo-Aero-ELastic analysis program (Grumman Aerospace Corp.)
STARS	STructures, Aerodynamics, and Related aeroServoelastic systems analysis

1. INTRODUCTION

1.1 Background

The Vehicle Technology Branch of the Research Engineering Division at NASA's Ames-Dryden Flight Research Facility (DFRF) is primarily involved in the synthesis and flight testing of novel advanced aerospace vehicles, often in cooperation with such agencies as the U.S. Air Force, U.S. Navy, and Defense Advanced Research Project Agency (DARPA). Due to the increasing occurrence of aeroservoelastic (ASE) instabilities in such aircraft development programs, the Division is also engaged in related research activities, including the development of tools to investigate performance characteristics, and most importantly, to ensure the safety of these aircraft. The trend toward more efficient, flexible structures and higher gain, control configured flight control systems is the basis for one such tool. This tool, STARS (STructures, Aerodynamics, and Related aeroServoelastic systems analysis), integrates the often separated areas of structures, aerodynamics, and controls, enabling analyses to be efficiently and effectively conducted, even on complex advanced aircraft. Thus, the need for advanced analytical tools is being met by NASA's research and development, which, in part, includes this project. Specifically, this project performs various analyses using the integrated STARS program on two advanced airplane configurations, the Forward Swept Wing (FSW) X-29A Airplane, and the Oblique Wing Research Aircraft (OWRA). The results of these analyses are then compared to other results.

In the area of structural dynamics, it is vital to predict the flutter and divergence characteristics to ensure flight safety. Time consuming efforts, such as free vibration analyses and unsteady aerodynamic calculations must be performed prior to such predictions. This work is often followed by a complete aeroservoelastic (ASE) controls analysis, which further relates to the safe performance of the aircraft within the designed flight flutter envelope. In connection with the FSW X-29A, flight testing is being conducted at NASA Ames Dryden Flight Research Facility, and exhaustive analyses have been performed to support the project. The results of these tests and analyses provide the opportunity to validate analytical techniques in various disciplines, is as done in this project.

The asymmetrical configuration of the Oblique Wing Research Aircraft (OWRA) poses a

challenge to the analytical capabilities in existence. Special capabilities are evolving in order to handle this unusual situation, such as the development of a potential gradient aerodynamic code. The OWRA provides the opportunity to perform complex analyses using the STARS program. The tasks involved in the research of these two airplanes are outlined in Section 1.3, while the scope of this project is presented in Section 1.2.

1.2 Project Objective

Due to the trend towards more flexible and complex aircraft, an efficient analytical tool to quickly assess the performance characteristics and to verify the stability of such aircraft is necessary. The objective of this project is to use such a tool to perform integrated analyses of structures, aerodynamics, and controls. The results of these analyses are then to be correlated and compared to other existing verified results. This objective is achieved by using the STARS program to predict analytically the performance characteristics of the two advanced airplanes mentioned above, the FSW X-29A and the OWRA. The tasks associated with these analyses are described in detail in the next section.

1.3 Project Overview

Using the STARS program, various analyses were performed on the X-29A and the OWRA. Finite element modeling, free vibration analyses, unsteady aerodynamic calculations, flutter and divergence analyses, and an ASE controls analysis were all performed on the X-29A. Some of the earlier analyses presented in this project were performed prior to the start of this project by NASA STARS - Team engineers, however, the review of this material was required to continue further analyses. In connection with the OWRA, finite element modeling and free vibration analyses were performed. An attempt has been made in solving the OWRA free vibration problem by utilizing the detailed finite element model (FEM), thus circumventing the approximate dynamic reduction procedure. Although this involves the solution of a much higher order eigenvalue problem, the attempt was made to determine if this approach can provide more accurate and reliable results. The

tasks associated with this project are delineated below.

- 1) Review of the X-29A finite element modeling, free vibration results, and aerodynamic grids prepared by the NASA STARS - Team.
- 2) Flutter analyses of the symmetric and anti-symmetric cases of the X-29A using three analytical techniques. The results are then correlated.
- 3) Aer servoelastic controls analysis of the X-29A longitudinal analog reversion control mode. The results are then compared to existing results.
- 4) Finite element modeling of the OWRA, including the conversion of the NASTRAN FEM to a STARS FEM. Also, the node numbers of the OWRA FEM are renumbered to minimize the bandwidth, and the validity of the FEM is checked.
- 5) Free vibration analysis of the OWRA.

The remainder of this report is described by the following paragraphs. Chapter Two briefly discusses the background of this project. This includes a description of the STARS program, as well as descriptions of the two advanced aircraft, the X-29A and the OWRA, analyzed in this project.

Chapter Three contains the results of the analyses performed on the FSW X-29A. A brief review of the finite element modeling and vibration analyses is presented. Three solution techniques, namely the k, p-k, and ASE (state-space) methods, are discussed, and the results of each are correlated and compared. Also, an ASE controls analysis solution technique is described, and the results are correlated.

Chapter Four contains a brief description of the OWRA, presenting its history and merit as a research project. The finite element model is detailed, and the free vibration analysis attempt is reviewed. A discussion is presented detailing the advantages and disadvantages of using the detailed FEM over a dynamic reduction scheme.

In Chapter Five, the management of the project is presented. The project's organizational structure, schedule, and budget are discussed, as are the management techniques employed.

Chapter Six summarizes the results obtained, and presents recommendations for further research.

Chapter Seven contains the literature references.

2. PROJECT ELEMENTS AND BACKGROUND

2.1 Introduction

The Vehicle Technology Branch of the Research Engineering Division of NASA at the Dryden Flight Research Facility has developed a computer program, STARS (STructures, Aerodynamics, and Related aeroServoelastic systems analysis), to perform integrated structural modeling, and free vibration and flutter/divergence analyses, in addition to aeroservoelastic (ASE) stability analyses (References 1 and 2). Several computer routines are readily available to perform various facets of the analyses; however, it was deemed advantageous to integrate the current and advanced analytical formulations into a single, compact computer program. The modular STARS program is interactive and graphics oriented, and due to its compactness, it is highly efficient. For these reasons, STARS was judged to be an effective tool in the study of two modern high-performance, complex airplane configurations. In this chapter, in addition to a description of STARS, features of the two forementioned airplanes, the Forward Swept Wing X-29A and the Oblique Wing Research Aircraft, are presented.

2.2 STARS Description

The STARS program consists of six major modules (see Figure 2.1): the preprocessor, postprocessor, graphics, the analytical capabilities for FEM structures, unsteady aerodynamics, and aeroservoelastic controls. The major capabilities of STARS are listed in Table 2.1, and a simplified flow chart is shown in Figure 2.2.

The preprocessor module is an interactive graphics program used for the automatic generation of finite element mesh for any structure. The preprocessor is able to generate complex structures through interpolation, duplication, mirror-imaging, and cross-sectioning of representative structures by the use of either menu or command options.

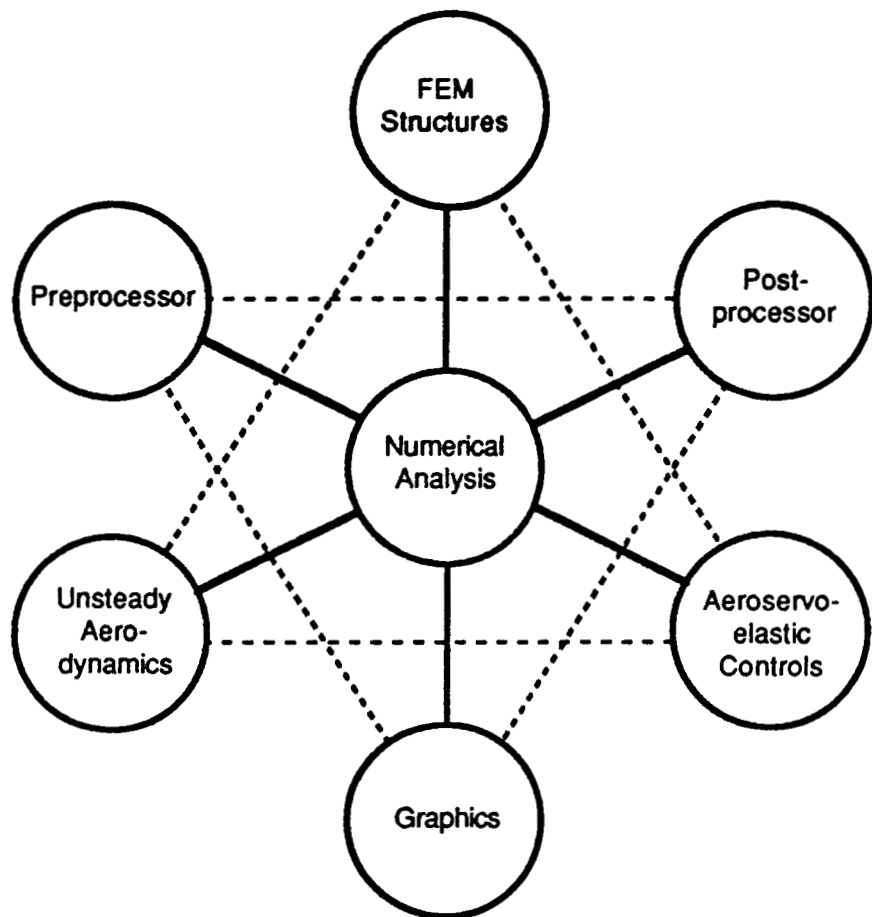


Figure 2.1 Major Modules of STARS Computer Program

Table 2.1 Major Capabilities of STARS

- >>Finite element modeling
- >>Spinning structures
- >>Mechanical and thermal loading
- >>General and composite materials
- >>Vibration
- >>Dynamic response
- >>Buckling
- >>Statics
- >>Unsteady aerodynamics
- >>Flutter/divergence analysis
- >>Padé and least squares approximations
- >>Open and closed loop aeroservoelastic controls analyses

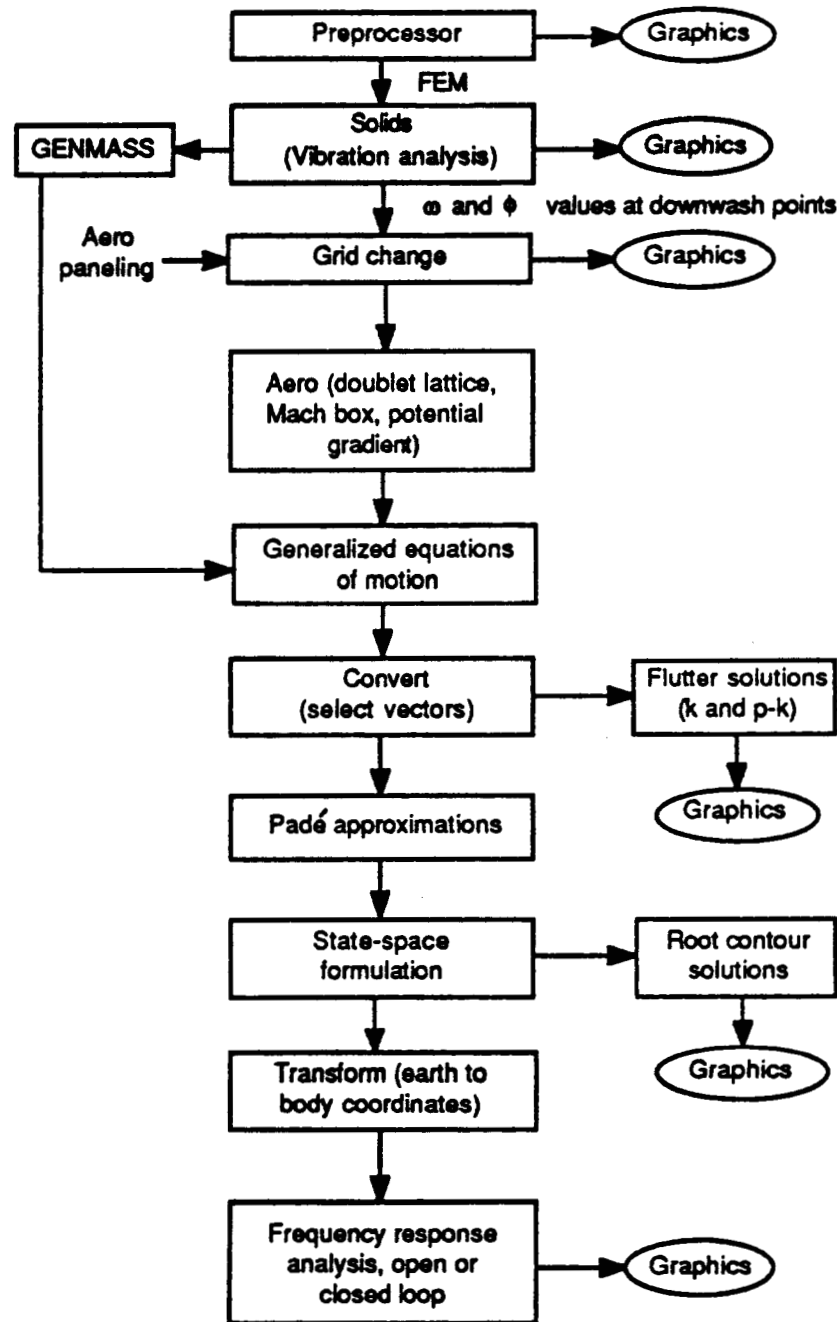


Figure 2.2 Simplified Flow Chart of STARS Computer Program

The finite element module allows structures to be modeled using any combination of one-, two-, or three-dimensional elements. The one-dimensional elements include bars, beams, and rods. The two-dimensional elements consist of triangular and quadrilateral membranes, plate bending, shear, and shell elements including sandwiches and composites. The three-dimensional elements include lines, tetrahedrons, hexadrons, and prisms. Special features of the finite element module include random data input (meaning non-sequential data input is allowed), automatic node and element generation, a matrix bandwidth minimizer, general nodal deflection boundary conditions, and multiple sets of static loads. A global-local coordinate system exists, with the capability of multiple local coordinate systems. Along with the numerical analysis module, the FEM module can perform analyses for statics, vibration, buckling, and dynamic responses of structures, including those with spinning or prestressed components.

The unsteady aerodynamics module (Reference 3) is used to calculate the unsteady aerodynamic forces in the frequency domain, and for calculating flutter/divergence solutions. This module utilizes the doublet lattice technique to determine subsonic forces, while supersonic forces are calculated using the Mach box and the potential gradient techniques. The flutter and divergence analysis can be performed by either the k or the p-k method, as well as by the ASE method. The flutter and divergence techniques will be discussed in detail in a Chapter 3.

The aeroservoelastic controls module considers the aerostructural problem in the Laplace domain. The unsteady aerodynamic forces are curve-fit using a Padé and least squares approximation, generating the appropriate state-space matrices (see References 4, 5, and 6) including the flight control system. This module then performs a coordinate transformation from an earth-fixed to a body-fixed system, which allows the control laws and a feedback system to be incorporated.

The postprocessor module, along with the graphics module, provides the plotting capabilities for the appropriate STARS modules. The plotting capabilities include mode shapes, nodal deformations, contour lines of deformations and stresses. Also, flutter and divergence plots, and frequency responses from the ASE module are available.

ORIGINAL PAGE IS
OF POOR QUALITY

2.3 Description of the X-29A

The X-29A is a forward swept wing (FSW) airplane sponsored by DARPA and supported by NASA. The X-29A shown in Figure 2.3 is a single-seat fighter-type aircraft, with a wingspan of 27 ft, length of 48 ft, and with a lightweight fuel loading it has a weight of 14,931 lbs (Reference 7). The potential advantages of a FSW that led DARPA to the development of the X-29 are summarized in Table 2.2. During the preliminary design phase of the X-29, it was decided to incorporate other advanced technologies to maximize the available experimental flight test data. Thus, in addition to the forward swept wing concept, the X-29A integrates several advanced technologies which are outlined in Table 2.3.

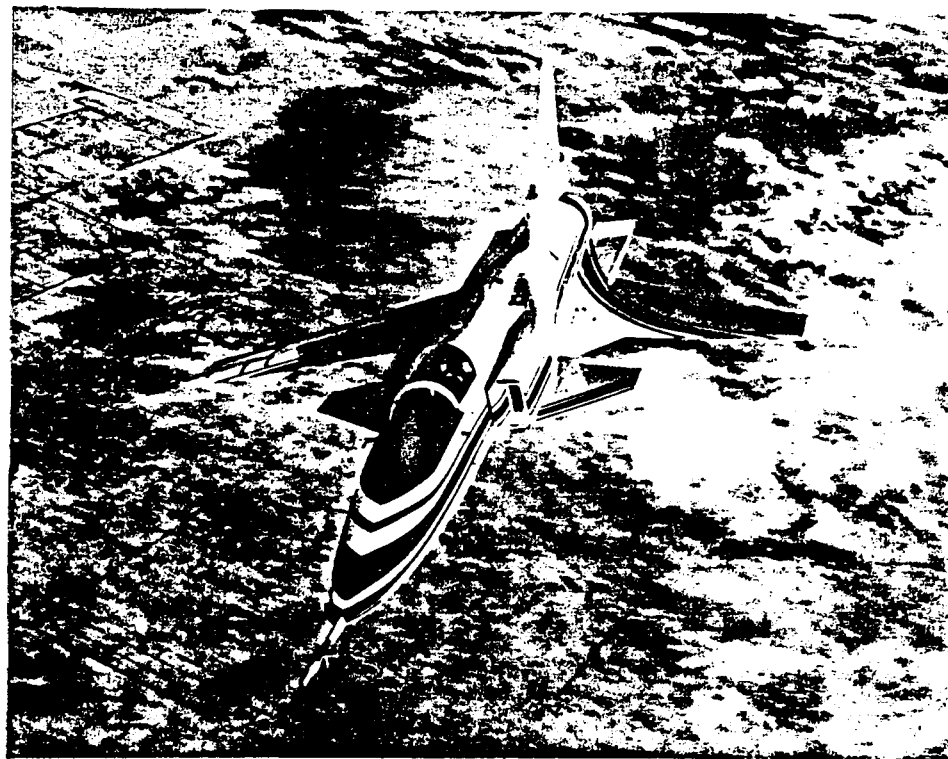


Figure 2.3 X-29A In Flight

Table 2.2 Potential Advantages of a Forward Swept Wing

1. Improved lateral control at high angles of attack resulting from inboard spanwise flow and subsequent delayed wingtip stall.
2. A reduction in wing profile drag as compared with an aft swept wing with the same shock sweep angle.
3. A decrease in wing structural box weight or an increase in aerodynamic efficiency resulting from the geometric differences in the forward swept wing and the aft swept wing for designs with the same shock sweep angle.
4. Increased fuselage design freedom due to aft placement of the wingbox that permits more effective fuselage contouring to minimize wave drag.
5. Reduced trim drag resulting from less wing twist required with a FSW.

Table 2.3 Technologies Incorporated on the X-29A

1. Thin supercritical airfoil for aerodynamic efficiency.
2. Aeroelastically-tailored composite wing structure.
3. Variable incidence close-coupled canard.
4. Three-surface longitudinal control.
5. Relaxed static stability (up to 35-percent statically unstable).
6. Triplex digital fly-by-wire control system.
7. Discrete variable camber control.

The X-29A aeroelastic wing tailoring is utilized to control the divergence typically associated with FSW designs. Aerodynamic efficiency over the flight envelope is optimized through the use of dual-hinged, trailing edge flaperons. This optimization provides high lift during takeoff and landing, and during lateral control and programmed variable-camber operations. As mentioned in Table 2.3, the X-29A has highly relaxed longitudinal static stability. Specifically, the addition of the canard to the wing-body results in a negative static margin of 35%. As the airplane reaches supersonic speed, the shift in static margin is +40%, as shown in Figure 2.4 (Reference 8). This is partly due to the center of pressure shift and partly due to the loss of the wing upwash on the canard. Longitudinal control is provided by the combination of the all-movable canards, the full-span flaperons, and the strake flaps. The single vertical fin that employs a rudder for directional control provides directional stability. The digital fly-by-wire flight control systems, in addition to the forementioned technologies, results in a highly maneuverable airplane over its Mach number range.

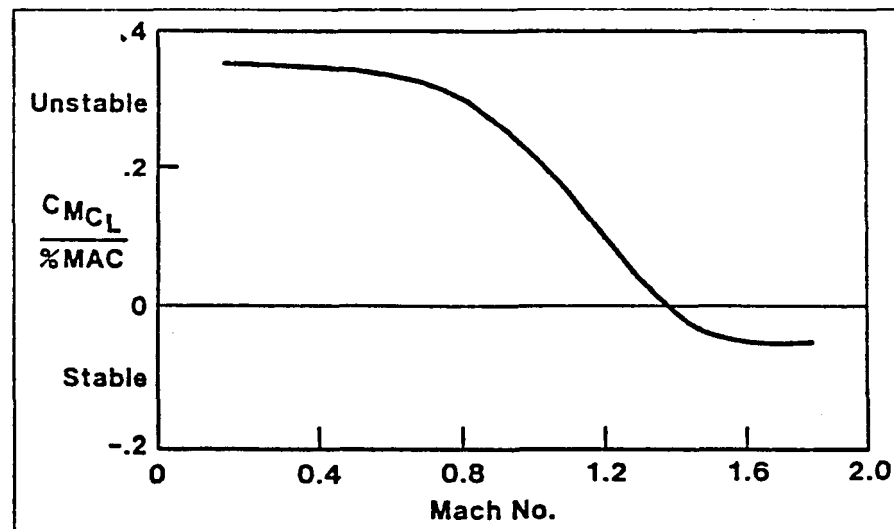


Figure 2.4 Relaxed Static Stability of the X-29A (from Ref. 8)

2.4 Introduction to Oblique Wing Research Aircraft

The potential benefits resulting from an oblique wing configuration has led NASA in a proposed program to design, fabricate, and flight test a full-scale demonstrator vehicle. Currently under study is a 300 ft² oblique wing mounted on an F-8 fuselage as shown in Figure 2.5. Because of their asymmetry, oblique wings present unique aerodynamic and structural development and analytical challenges. Thus, the OWRA program will provide an excellent opportunity to expand oblique wing technology and to study the integrated analyses using the STARS program. A description of the proposed OWRA follows.

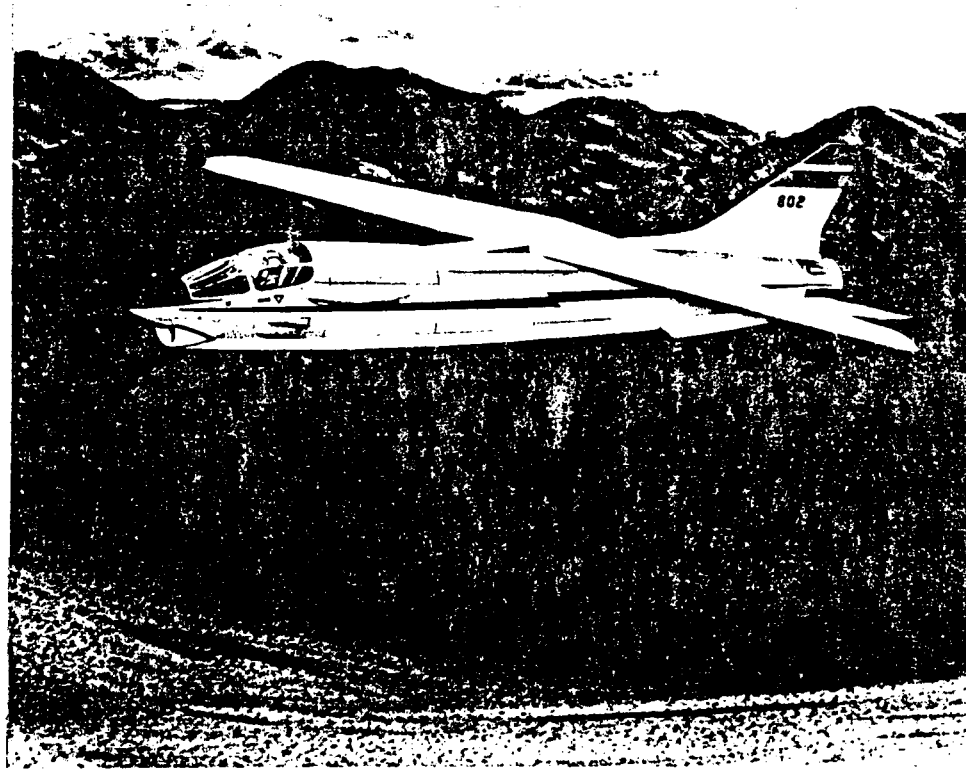


Figure 2.5 Artist's Rendition of the Proposed OWRA

The characteristics of the OWRA are given in Table 2.4 (Reference 9). The OWRA is designed for five in-flight sweep angles: 0, 30, 45, 55, and 65 degrees. The various sweep angles of the oblique wing offer several different mission capabilities. The oblique wing, in the unskewed position, offers the benefits of a straight wing for low-speed, high lift flight. In the skewed position, the OWRA offers efficient supersonic cruise capability (as compared to airplanes with symmetric swept wing configurations.) Thus, the OWRA's mission requirements are supersonic cruise, loiter, supersonic dash, and transonic cruise. Figure 2.6 illustrates fundamental aerodynamic advantages (Reference 10) showing the capability of the OWRA to efficiently meet the mission requirements. This is shown quantitatively in the drag equation, Equation 2.1, as given by linear theory (Reference 11).

$$\text{Drag} = C_{D_0} q S + \frac{L^2}{\pi q b^2} + \frac{M^2 - 1}{2 \pi q} \frac{L^2}{X_1^2} + \frac{128q}{\pi} \frac{\text{Vol.}^2}{X_2^4} \quad (2.1)$$

Here, C_{D_0} is the zero lift drag coefficient, q is the dynamic pressure, S is the wing area, L is the lift, b is the span, and M is the Mach number. X_1 and X_2 are averaged lengths $X(\theta)$ of the wing as projected by characteristic planes (Mach planes) set at different angles θ around the X axis. The lengths X_1 and X_2 are defined by Equations 2.2 and 2.3 below.

$$\frac{1}{X_1^2} = \frac{1}{\pi} \int_0^{2\pi} \frac{\sin^2 \theta}{X(\theta)^2} d\theta \quad (2.2)$$

$$\frac{1}{X_2^4} = \frac{1}{2\pi} \int_0^{2\pi} \frac{d\theta}{X(\theta)^4} \quad (2.3)$$

X_1 and X_2 , at low supersonic Mach numbers and large angles of sweep, are approximately the actual length of the wing. Thus, the wave drag due to lift diminishes as the inverse square of the length, while the wave drag due to volume decreases as the inverse fourth power of the length.

In addition to the fundamental aerodynamic advantages, the oblique wing avoids the aerodynamic center (AC) shift that occurs on the symmetric variable sweep airplanes. Avoiding the AC shift reduces trim drag penalties, and results in lighter fuselage and horizontal tail structural designs due to reduced tail loads.

A final major advantage of the oblique wing over the symmetric variable sweep airplanes comes from lift forces that are balanced (for symmetric loads) about a single pivot, as shown in Figure 2.7. This results in structural savings by the elimination of one of the dual pivots that are utilized on symmetric variable sweep airplanes, and by the reduction of the structure required to carry the bending and torque loads that are inherent with the dual pivot arrangement.

Table 2.4 Characteristics of the Proposed OWRA

PERFORMANCE

Maximum normal acceleration	-2, +4 g's
Maximum dynamic pressure	1200 psf
Maximum Mach at altitude	1.8 at 65 degrees
Takeoff gross weight	25,585 lbs
Wing loading	85.3 psf

WING CHARACTERISTICS

Reference area	301.1 ft ²
Span	55.3 ft
Aspect ratio	10.2
Taper ratio	0.385
Thickness/chord ratio	14 percent, constant
Variable incidence	0 to 8 degrees
Bank angle	10 degrees at 65 degree wing skew

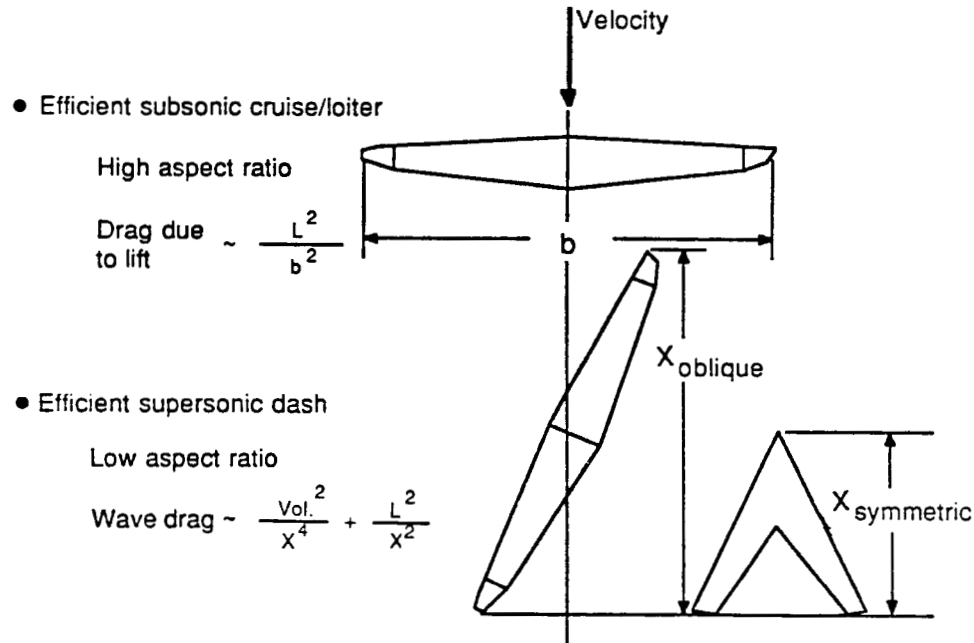
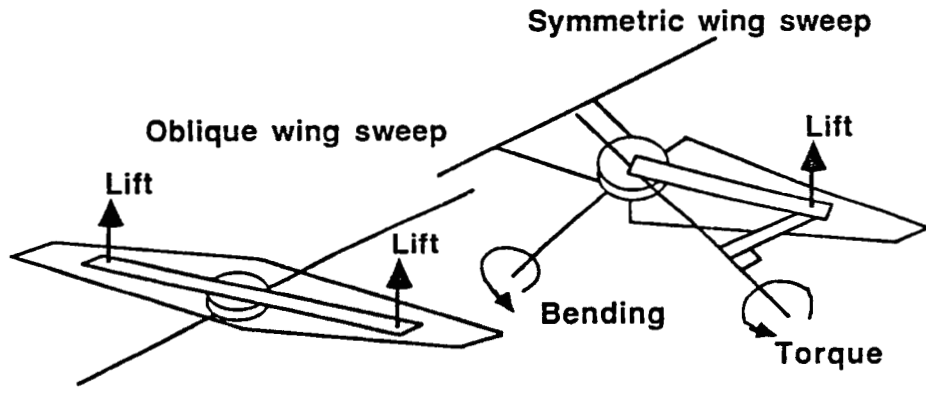


**Figure 2.6 Fundamental Aerodynamic Advantages of Oblique Wing
(from Reference 10)**



- Pivot torque and bending loads avoided
- Inboard wing torque loads avoided
- Single pivot

**Figure 2.7 Structural Advantage of the OWRA Shown by Avoidance of
Torque and Bending Loads (from Reference 10)**

3. X-29A ANALYSES AND RESULTS

3.1 Introduction

The increase of aeroservoelastic instabilities in recent aircraft development programs, as in the X-29A, has led to the development of needed validated and efficient analytical tools. In the area of structural dynamics, analytical analyses are vital for the prediction of flutter and divergence characteristics to ensure flight safety. Following this analysis, a complete aeroservoelastic (ASE) controls analysis is often performed, which further relates to the safe performance of the aircraft within the designed flight flutter envelope. Currently, the X-29A flight testing is being conducted at NASA Ames Dryden Flight Research Facility, and exhaustive analyses have been performed to support the project. This flight test program has given NASA the opportunity to check integrated analytical analyses to an extensive flight test data base. The NASA STARS - Team has already performed many analyses on the X-29A, and are continuing with this project, as described below.

In Section 3.2, the finite element model and free vibration analysis results, the first steps of the structural dynamics analyses, are reviewed briefly. Section 3.3 presents the aerodynamic grids prepared for the symmetric and anti-symmetric X-29A. The aerodynamic grid preparation is needed for use in the STARS unsteady aerodynamics module. This work was completed by the NASA - STARS Team, but its presentation and review are necessary for continuing further analyses. Section 3.4 presents a complete flutter/divergence analysis using the STARS unsteady aerodynamics module. Theories for the three different solution techniques of the flutter equation (the k, the p-k, and the state-space methods) are presented before the comparison of the results. The results are divided into two sections, the symmetric and anti-symmetric analyses. In each section, the results obtained by the three techniques are compared. Also, the anti-symmetric results illustrate the effect of including the rigid body modes in the analyses. In Section 3.5, the aeroservoelastic response characteristics for the longitudinal case of the X-29A are presented for a few select states. Open and closed loop gain and phase plots are presented and compared with existing results.

3.2 Structural Analysis of the X-29A

Figure 3.1 depicts the finite element model (FEM) developed and used for the STARS vibration analysis. This symmetric half-plane FEM consists of a beam fuselage, and a two-dimensional canard, wing, and vertical tail. The FEM has 513 nodes and 1241 elements using 110 different material types. This reduced-order model (3078 degrees of freedom) was derived by the equivalent shell method from the contractor's (Grumman Aerospace Corporation) full-stress model (approximately 7000 degrees of freedom). Specifically, the major airframe equivalent thin shell idealization was accomplished by evaluating the stiffness of the individual finite elements in the major directions. This was achieved by considering the effect of the skin, webs, spars, and beams. The stiffness of the webs, spars, and beams were then added to the appropriate skin elements. The wing skin composite material properties were considered to be anisotropic, and were determined for each layer of composite fiber orientation. These layers were then combined in equivalent shell elements in a local coordinate system by a suitable coordinate transformation. This was performed using a program written specifically for this task at NASA. The actuators and connecting linkages were modeled by truss and beam elements (Reference 2).

The analyses presented here were performed on the X-29A FEM described above for a lightweight fuel loading of 1320 lbs, or a total weight of 14,931 lbs (Reference 12). The vibration analysis was decoupled, as is usually done, into the symmetric/longitudinal and anti-symmetric/lateral-directional cases. Tables 3.1 and 3.2 compare the free vibration analysis results with the ground vibration survey (GVS) results and the Grumman Aerospace Corporation (GAC) analysis results for the symmetric and anti-symmetric cases, respectively. Figures 3.2 through 3.6 show typical mode shapes for the symmetric case, while Figures 3.7 through 3.10 show mode shapes for the anti-symmetric case. The STARS FEM and the GAC model did not include the modeling of the noseboom, unlike the airplane in the GVS. Thus, the noseboom mode identified from the GVS was not identified in the STARS analytical results. Apart from this, Tables 3.1 and 3.2 show good correlation between the STARS mode shapes and the GVS and GAC mode shapes from Reference 12. There are some discrepancies between the analytical and ground test generalized mass calculations, however, since neither method is completely accurate, these differences are assumed to

be acceptable. Thus, it is concluded that the STARS analytical results form a high quality data base for further flutter and ASE investigations.

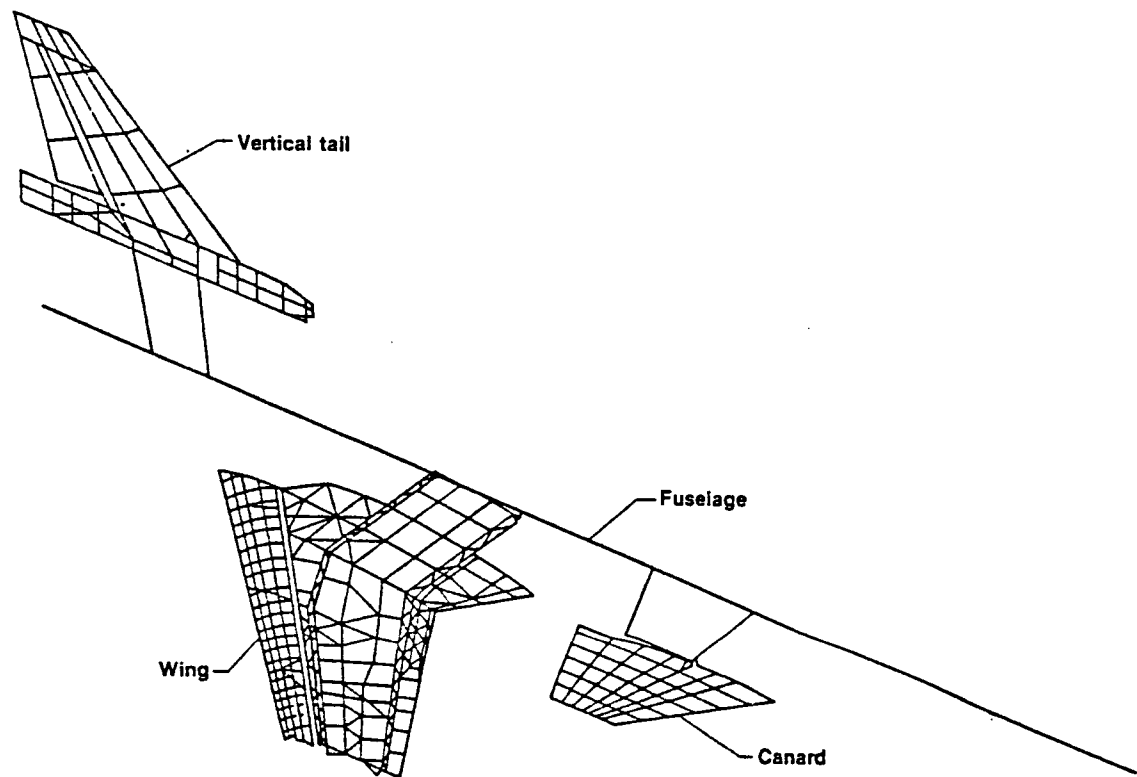


Figure 3.1 Finite Element Model of the X-29A

Table 3.1 Free Vibration Analysis Results for Symmetric X-29A

Primary Motion	STARS		GAC		GVS	
	Freq (hz)	Gen Mass (lb)	Freq (hz)	Gen Mass (lb)	Freq (hz)	Gen Mass (lb)
Rigid Body	0.0	7802.3*	n/a	7245.3*	n/a	7465.5*
W1B	8.96	246.8	8.11	146.0	8.61	140.3
F1B	12.87	954.5	10.02	518.0	11.65	617.8
F2B	19.03	104.6	19.62	1034.0	24.30	281.2
NB	—	—	—	—	20.50	3.3
CP	21.02	16.7	22.51	18.0	21.70	14.2
W2B	26.28	132.6	26.36	67.0	26.30	23.1
W1T	30.30	134.4	37.09	65.0	36.70	14.9
CBP	47.70	35.9	41.91	21.0	42.20	17.3
W3B	49.52	104.0	45.86	87.0	51.50**	4.9

* Half-aircraft weight and lightweight fuel condition

** GVS mode named Wing Inboard Flap Torsion

G A C : Grumman Aerospace Corporation
 G V S : Ground Vibration Survey

W1B : Wing First Bending
 F1B : Fuselage First Bending
 F2B : Fuselage Second Bending
 NB : Nose Boom
 CP : Canard Pitch
 W2B : Wing Second Bending
 W1T : Wing First Torsion
 CBP : Canard Bending Pitch
 W3B : Wing Third Bending

Table 3.2 Free Vibration Analysis Results for Anti-Symmetric X-29A

Primary Motion	STARS		GAC		GVS	
	Freq (hz)	Gen Mass (lb)	Freq (hz)	Gen Mass (lb)	Freq (hz)	Gen Mass (lb)
Rigid Body	0.0	7802.3*	n/a	7455.0*	n/a	7465.5*
W1B	10.08	57.7	13.11	483.7	11.3	75.1
F1B	12.35	757.7	9.22	688.5	12.5	426.1
Fin 1B	17.18	47.6	16.12	16.3	15.2	18.6
NB	—	—	—	—	20.6	2.0
CP	21.52	21.5	22.07	34.1	21.9	14.0
W1T	27.15	84.6	24.85	116.7	26.8	41.1
W2B	32.88	51.0	35.95	49.9	34.8	31.1
Fin 2B	41.58	7.1	50.23	9.8	45.2	6.8
W3B	45.85	275.4	52.80	**	51.7	11.1
Fin 1T	48.95	21.6	44.09	39.1	50.0	4.6
IFT	50.83	39.5	61.00	**	51.0	4.6

* Half-aircraft weight and lightweight fuel condition

** Not presented in full aircraft vibration analysis

W1B	:	Wing First Bending
F1B	:	Fuselage First Bending
Fin 1B	:	Vertical Fin First Bending
NB	:	Nose Boom
CP	:	Canard Pitch
W1T	:	Wing First Torsion
W2B	:	Wing Second Bending
Fin 2B	:	Fin Second Bending
W3B	:	Wing Third Bending
Fin 1T	:	Vertical fin First Torsion
IFT	:	Inboard Flap Torsion

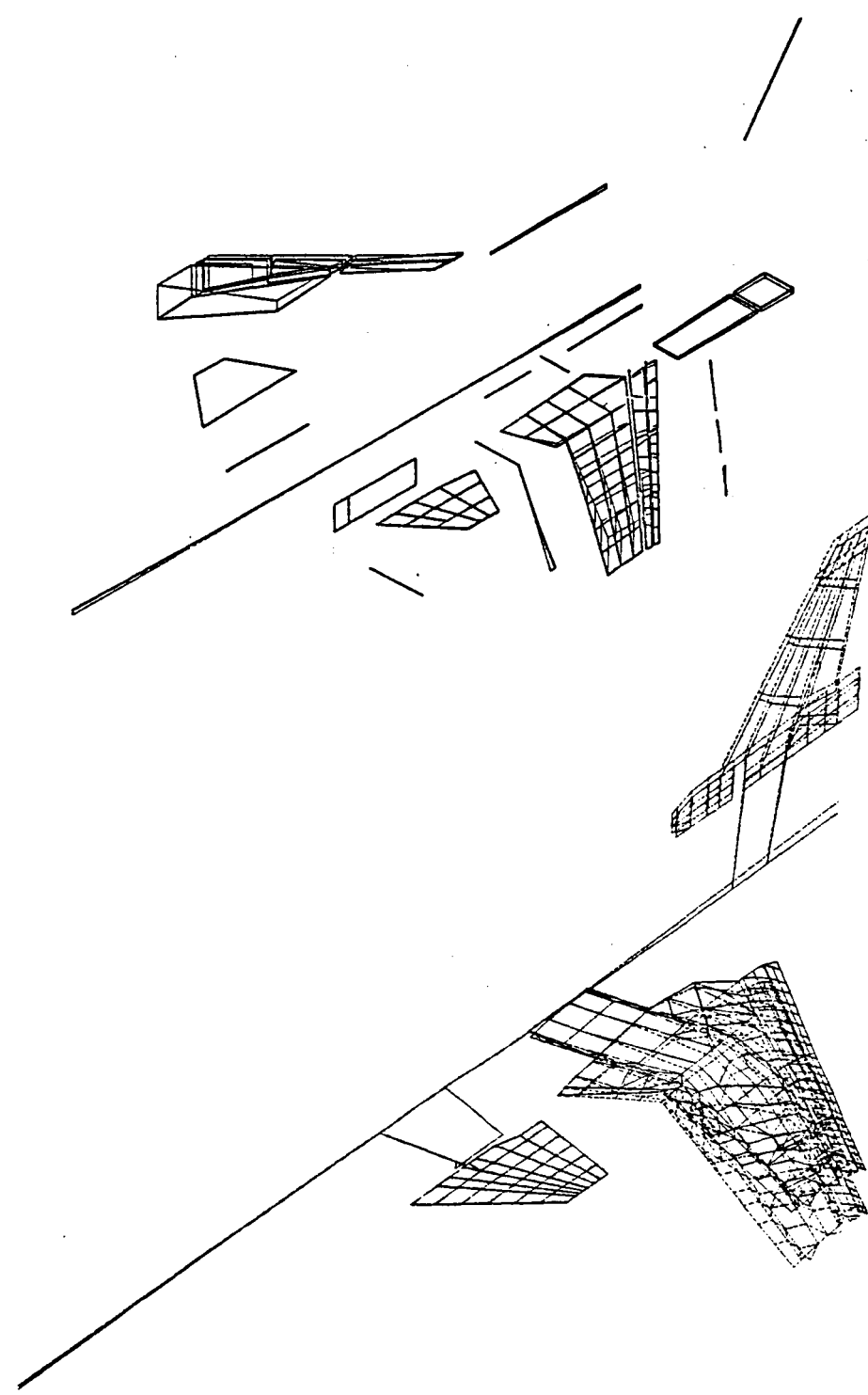


Figure 3.2 X-29A Symmetric Wing First Bending Mode (W1B)
Top: GVS Mode at 8.61 Hz
Bottom: STARS Mode at 8.96 Hz

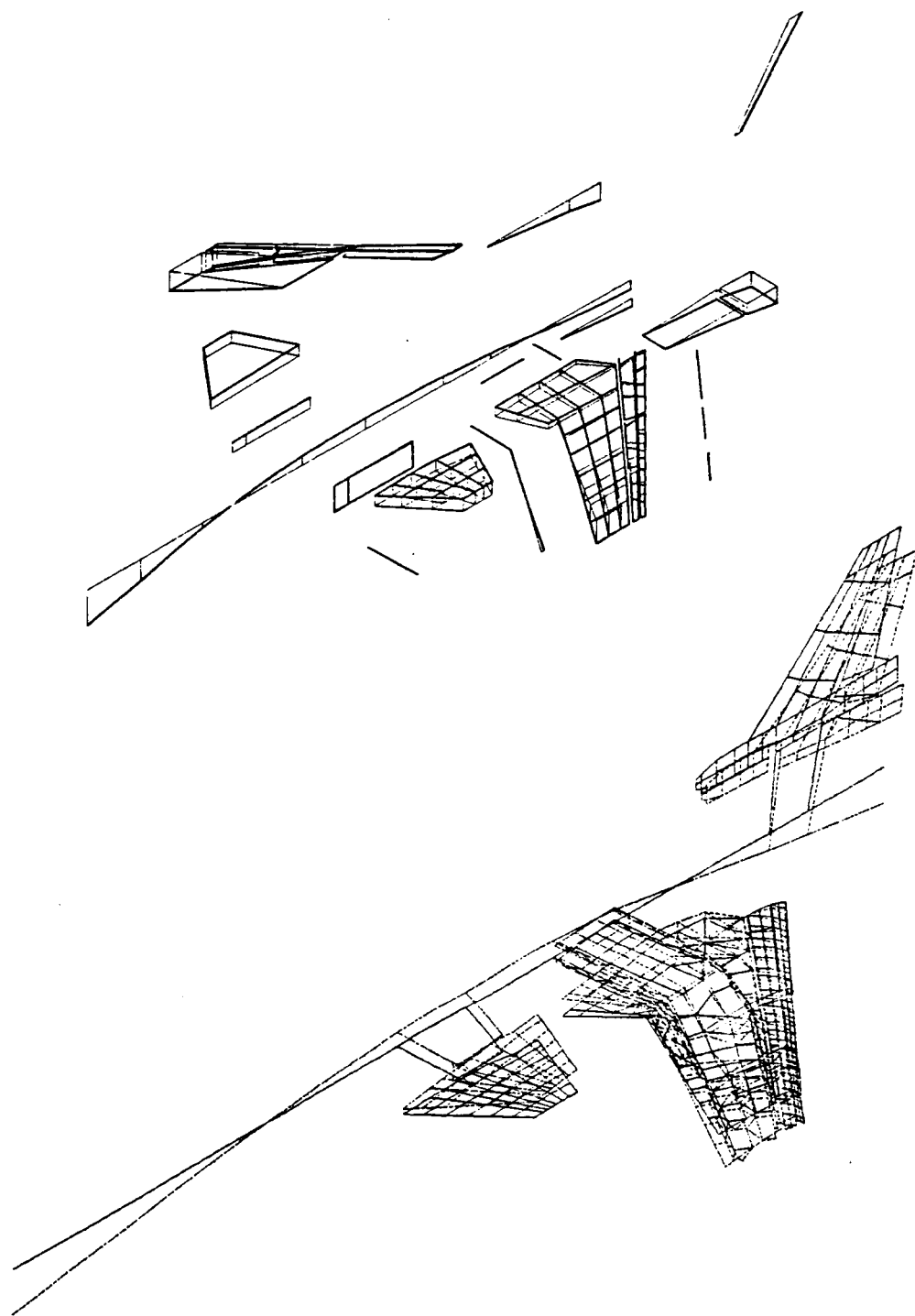


Figure 3.3 X-29A Symmetric Fuselage First Bending Mode (F1B)
Top: GVS Mode at 11.65 Hz
Bottom: STARS Mode at 12.87 Hz

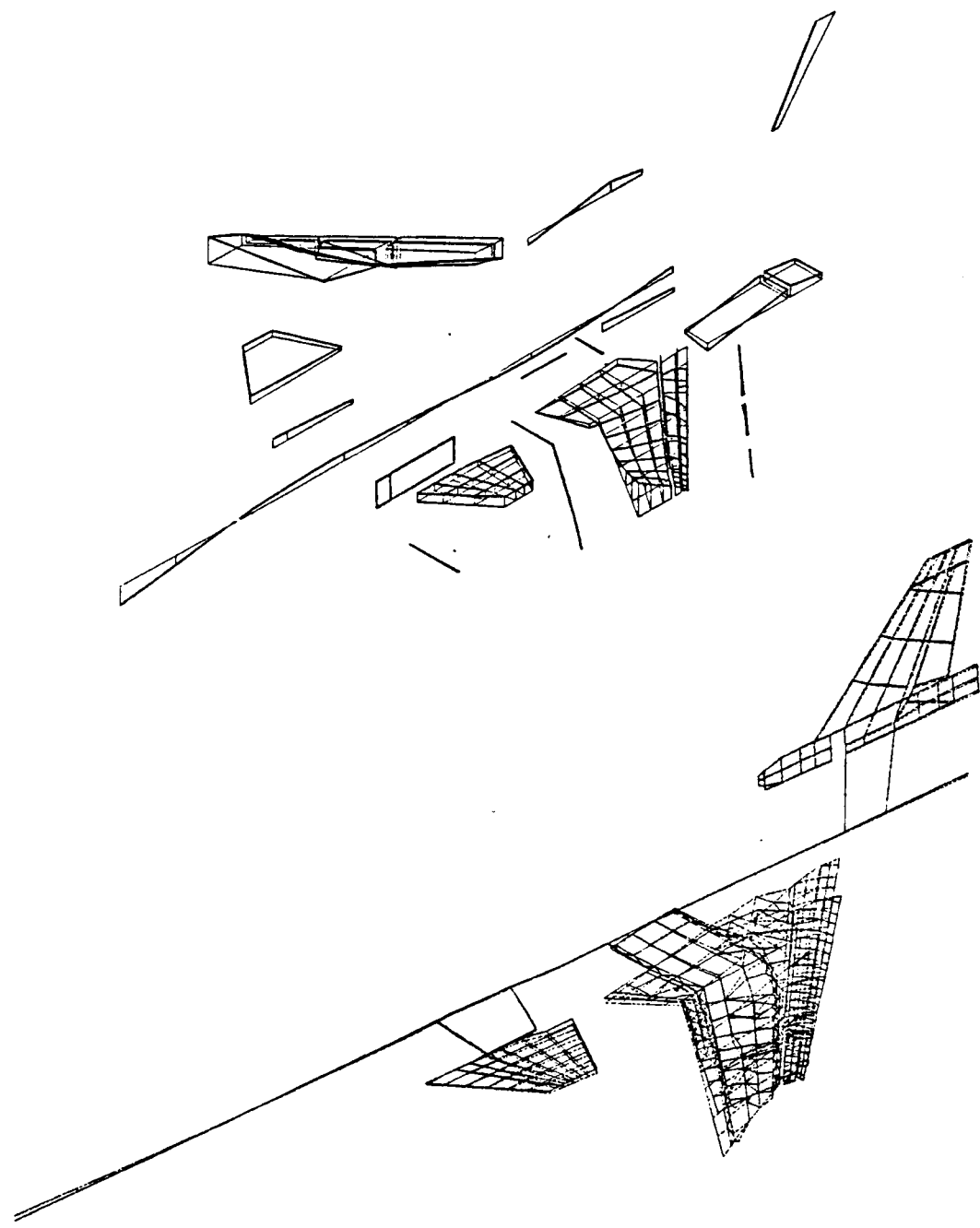


Figure 3.4 X-29A Symmetric Fuselage Second Bending Mode (F2B)
Top: GVS Mode at 24.3 Hz
Bottom: STARS Mode at 19.03 Hz

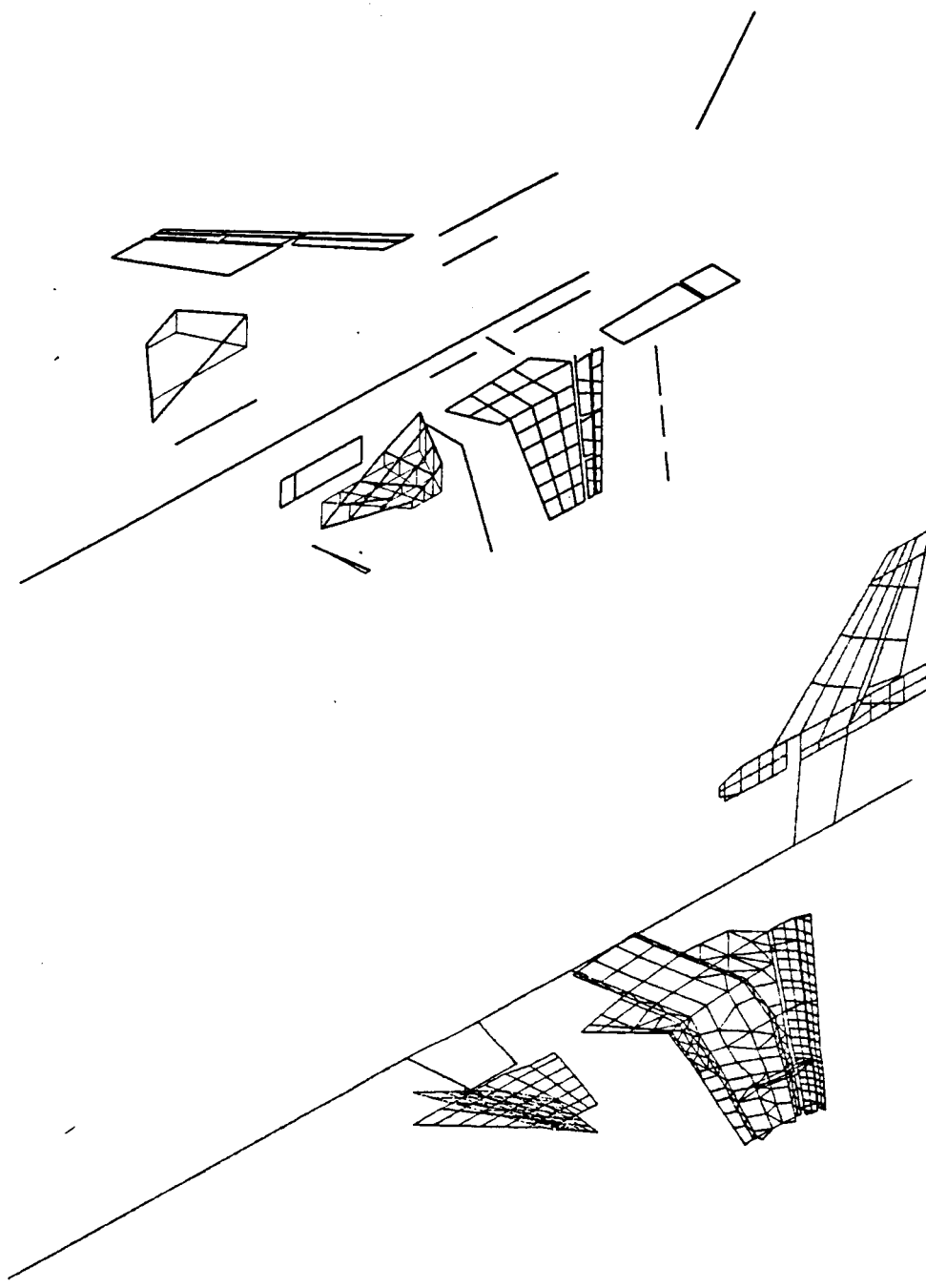


Figure 3.5 X-29A Symmetric Canard Pitch Mode (CP)
Top: GVS Mode at 21.7 Hz
Bottom: STARS Mode at 21.02 Hz

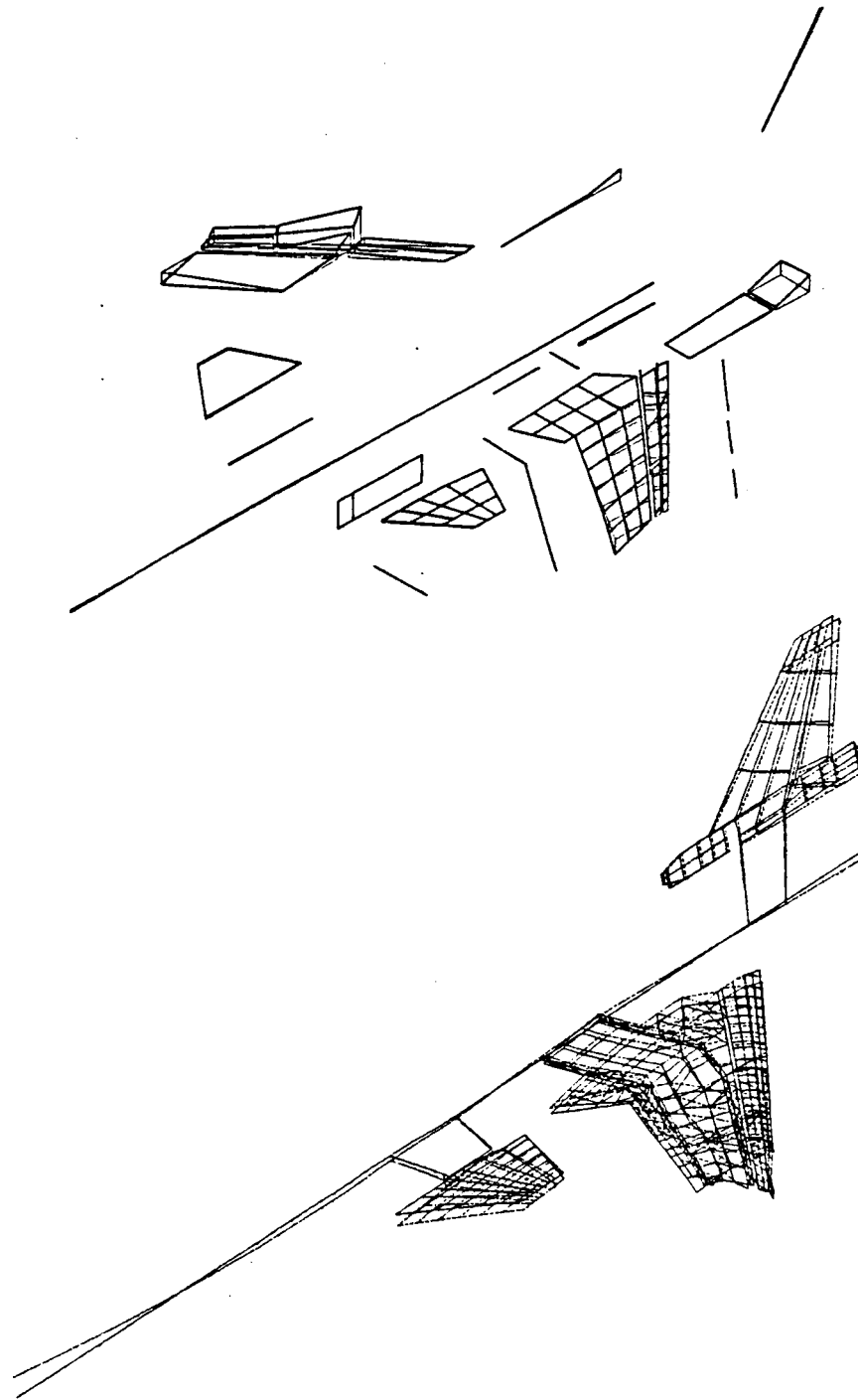


Figure 3.6 X-29A Symmetric Wing Second Bending Mode (W2B)
Top: GVS Mode at 26.3 Hz
Bottom: STARS Mode at 26.28 Hz

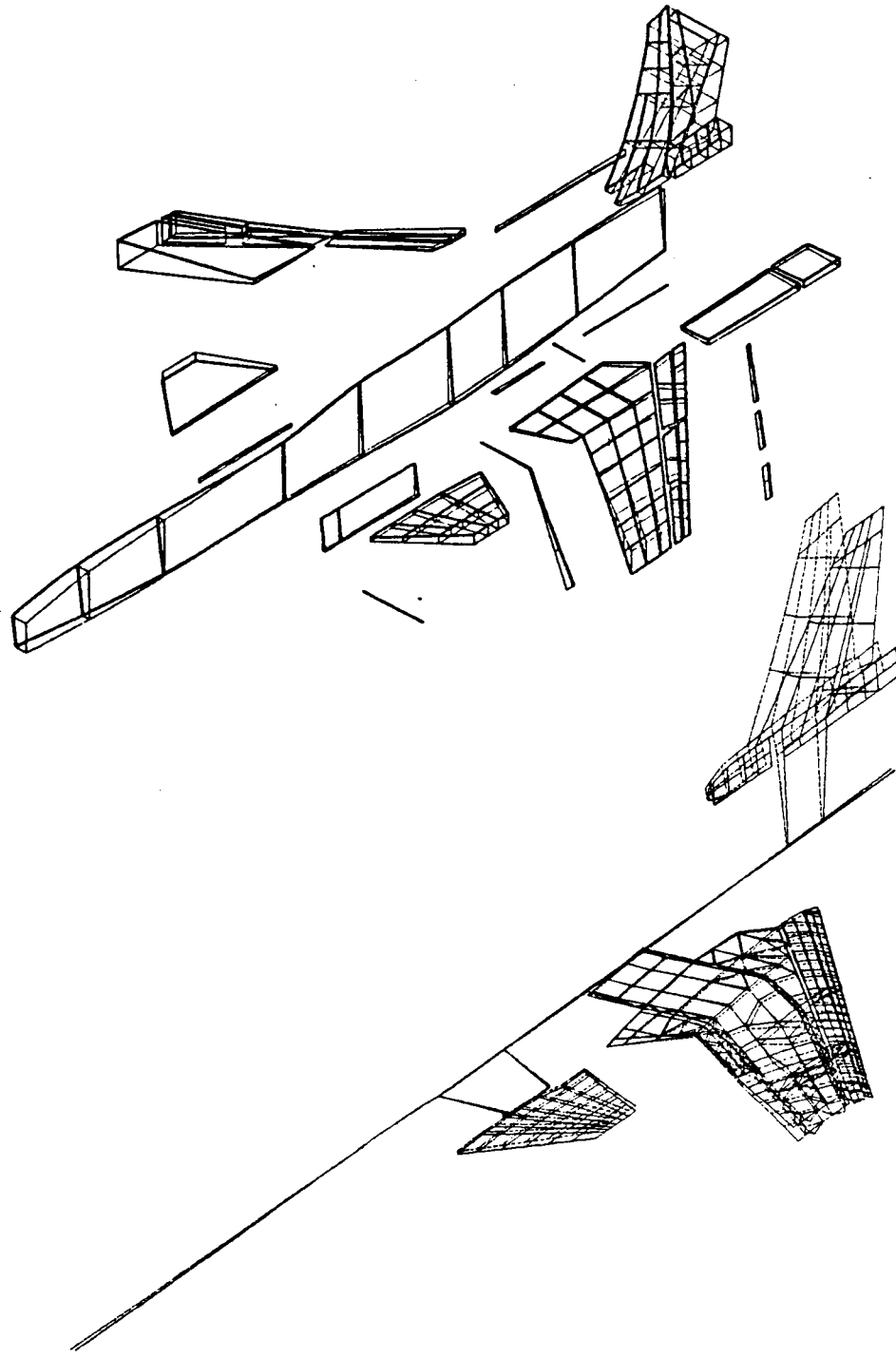


Figure 3.7 X-29A Anti-symmetric Wing First Bending Mode (W1B)
Top: GVS Mode at 11.3 Hz
Bottom: STARS Mode at 10.08 Hz

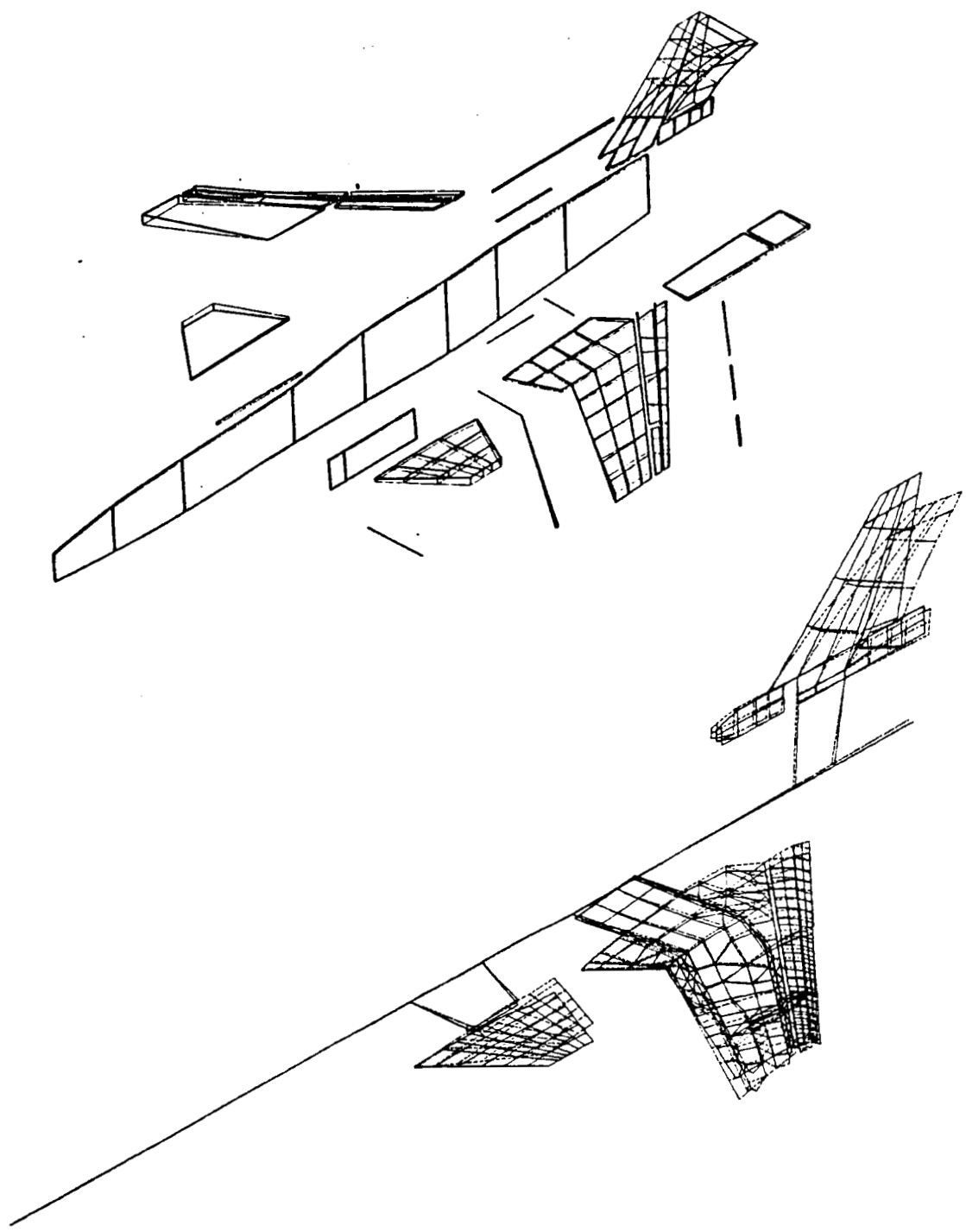


Figure 3.8 X-29A Anti-symmetric Fin First Bending Mode (Fin 1B)
Top: GVS Mode at 15.2 Hz
Bottom: STARS Mode at 17.18 Hz

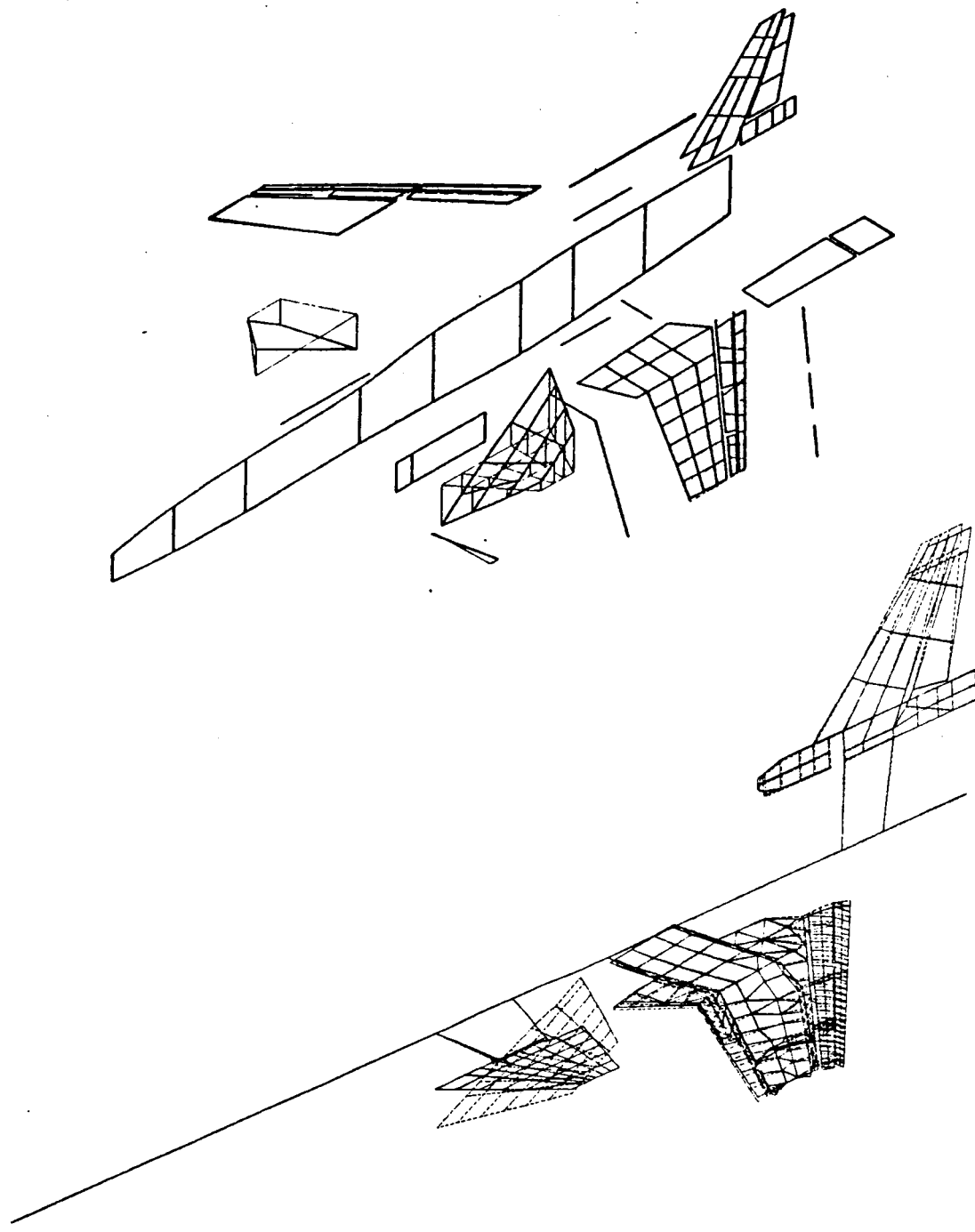


Figure 3.9 X-29A Anti-symmetric Canard Pitch Mode (CP)
Top: GVS Mode at 21.9 Hz
Bottom: STARS Mode at 21.52 Hz

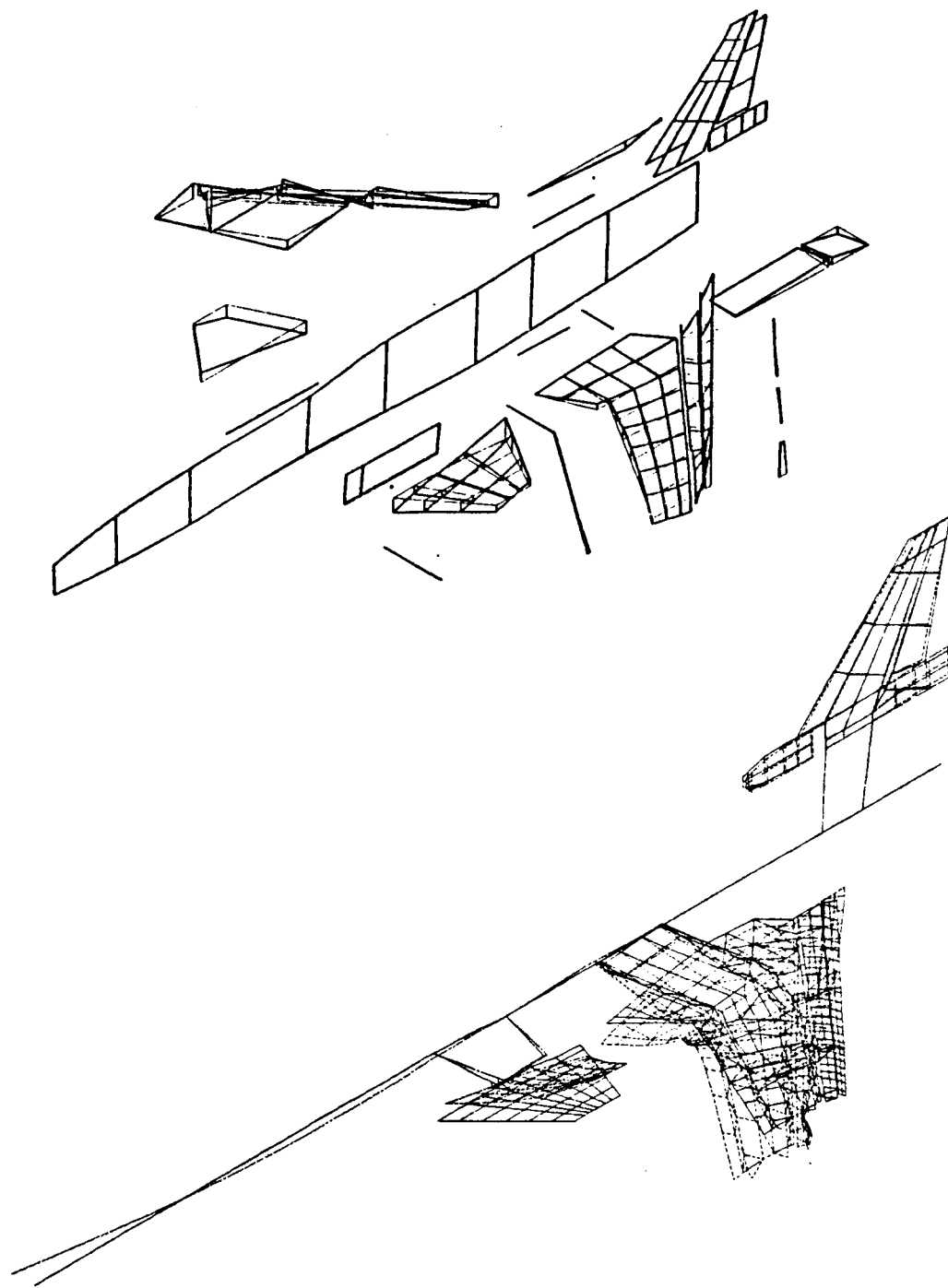


Figure 3.10 X-29A Anti-symmetric Wing Third Bending Mode (W3B)
Top: GVS Mode at 51.7 Hz
Bottom: STARS Mode at 45.85 Hz

3.3 Aerodynamic Modeling of the X-29A

This section presents the aerodynamic models prepared for the X-29A. Although this work was initially prepared by members of the NASA STARS - Team, review of this material was necessary for continuing the flutter/divergence analyses discussed in the next section.

Referring to the flowchart in Figure 2.2, it is seen that the aero paneling and vibration analysis are required for the unsteady aerodynamics calculations. The "Grid change" step is to relate the deflections from the vibration analysis to the aerodynamic grid. Reviewing the methodology briefly, the modal deflections from the vibration analysis are related to interpolating line points input to the STARS-Aero module. The spanwise deflections of the interpolation line points are determined (from the vibration data) first by using a Lagrangian interpolation scheme (Reference 13). The chordwise points of the interpolating lines are then calculated using the same technique. From the interpolation scheme, the deflections of the 1/4-chord of each aerodynamic element is calculated. The 1/4-chord point is used for the doublet lattice calculations, as the pressure is assumed to arise from a loaded line at this point.

Following this methodology, aerodynamic models were formed for the symmetric and anti-symmetric X-29A. Figure 3.11 shows the anti-symmetric X-29A canard, wing, and body interpolation lines. The interpolation lines used for the symmetric case are similar to Figure 3.11, however the vertical tail is excluded. Figure 3.12 shows the doublet lattice aerodynamic paneling idealization for the X-29A canard, wing, and body. Figures 3.13 and 3.14 show the interpolating lines and aerodynamic modeling for the anti-symmetric X-29A vertical tail.

For the purpose of this study, all unsteady aerodynamic calculations were performed at 0.90 Mach number and sea-level conditions. The aerodynamic forces used for the flutter/divergence analyses were calculated using the STARS analytical mode shapes by the doublet lattice technique described above. Also, it should be noted that this aerodynamic model does not include the strake, however, modifications were made for later analyses not included in this project.

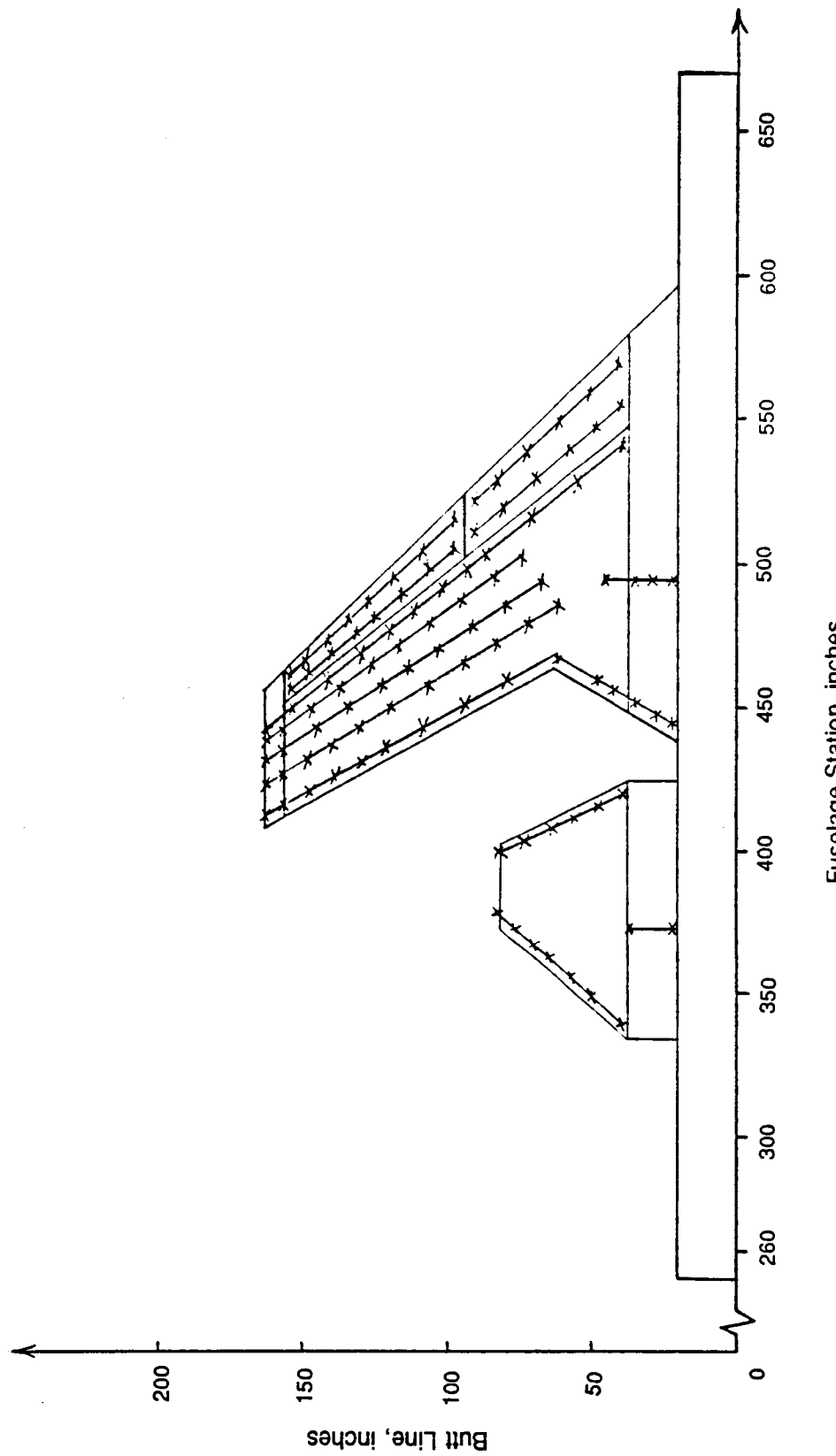
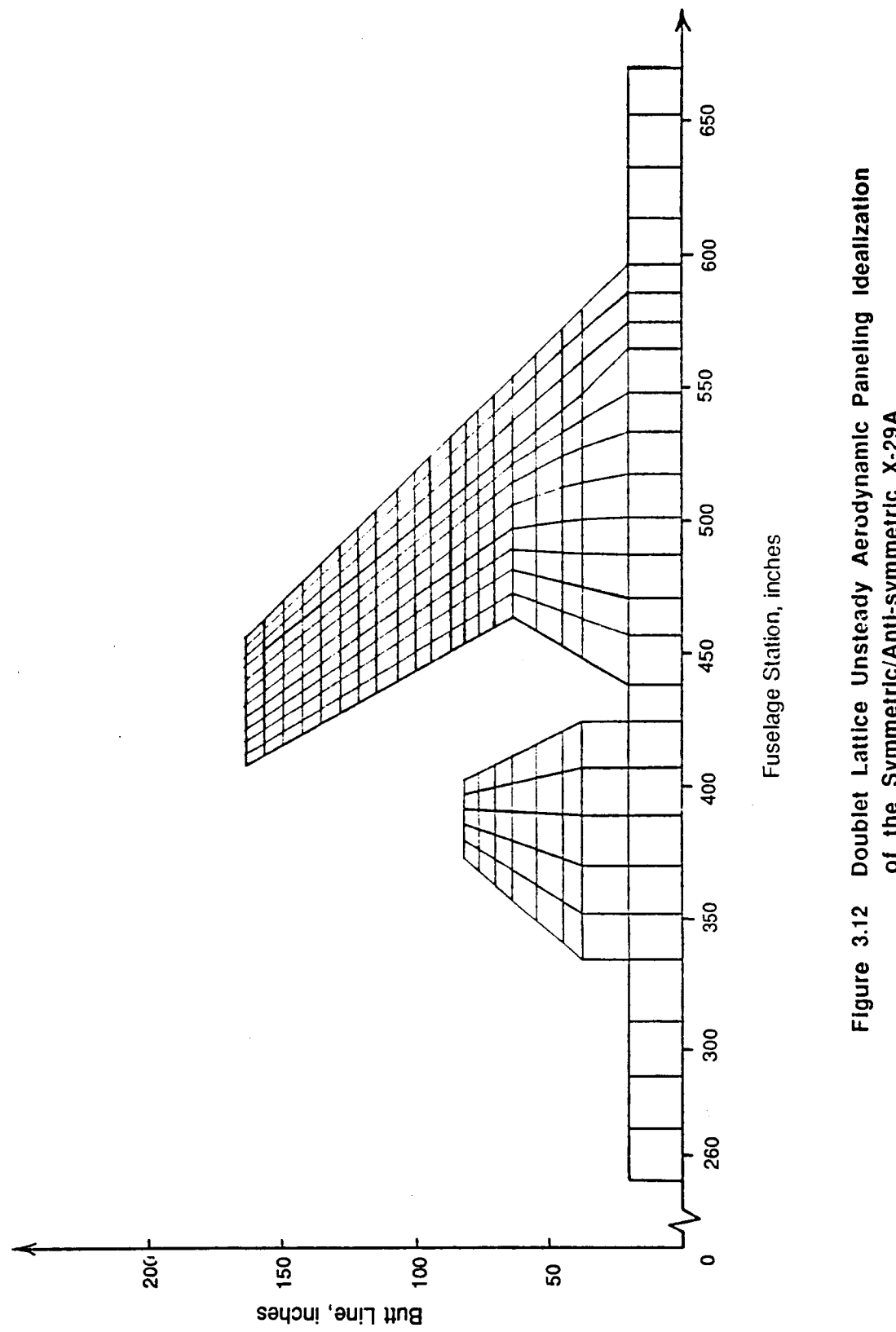


Figure 3.11 Anti-symmetric X-29A Canard, Wing, and Fuselage Aerodynamic Model, Showing Interpolating Lines



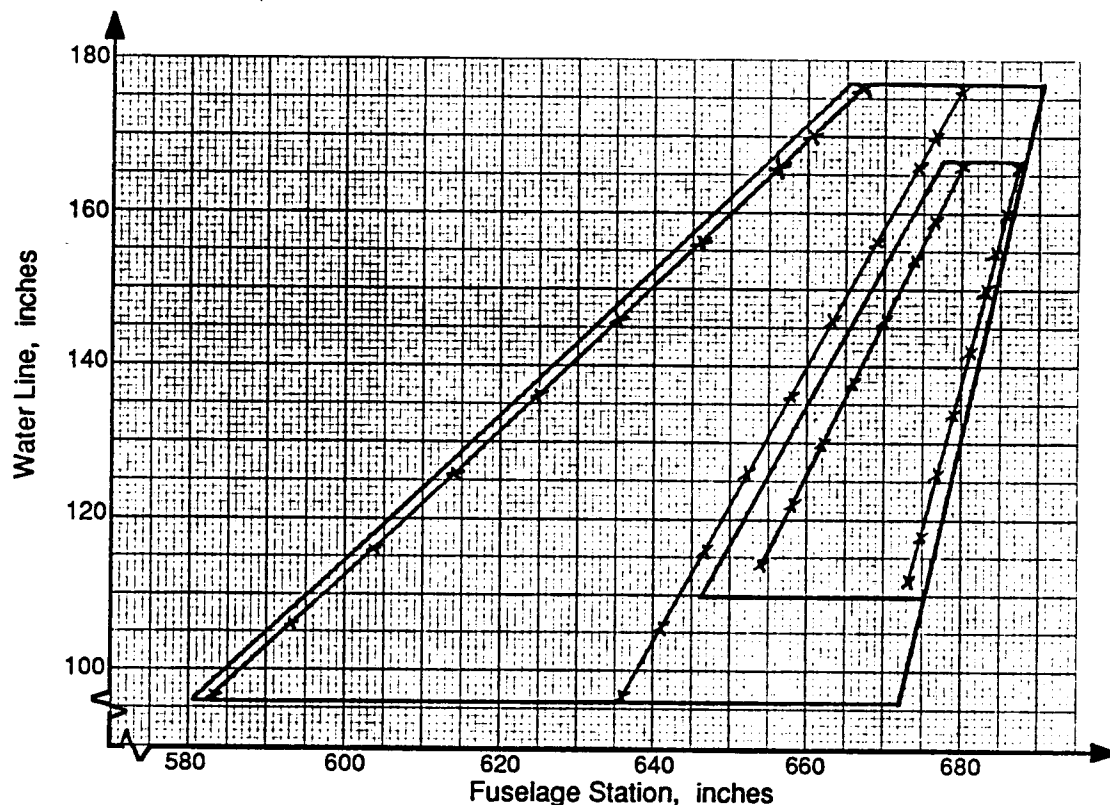


Figure 3.12 Vertical Tail Interpolating Lines for X-29A

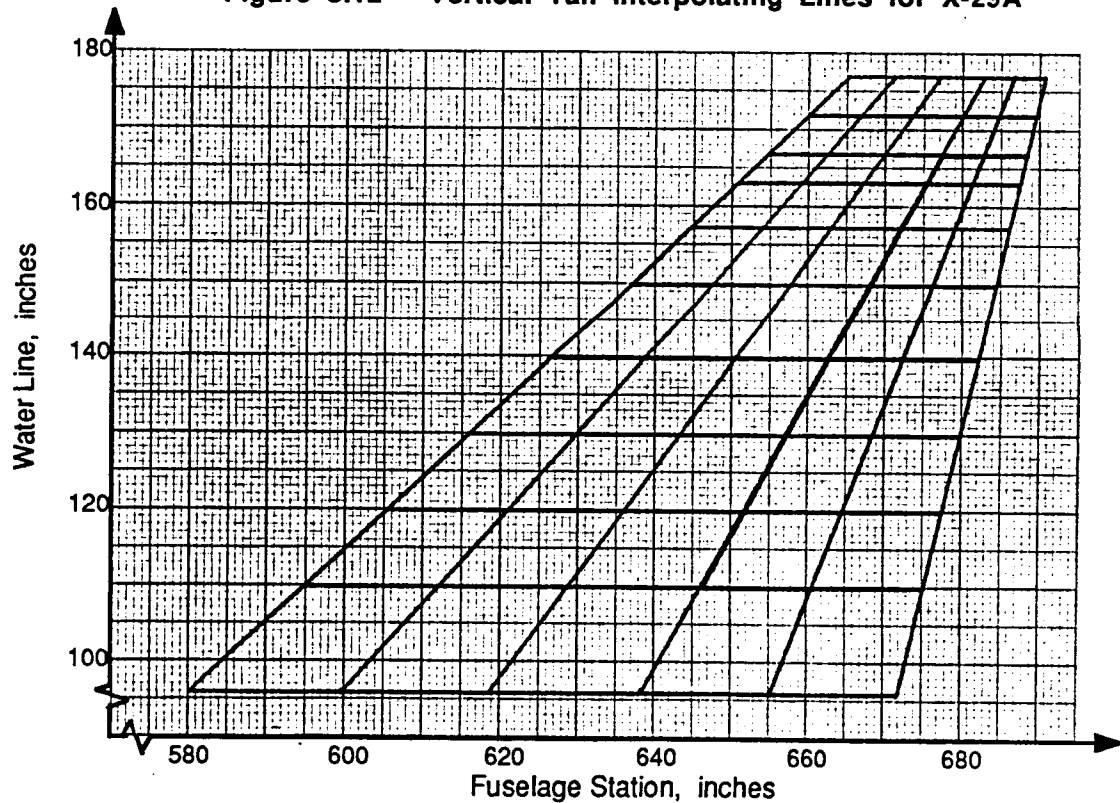


Figure 3.13 Doublet Lattice Unsteady Aerodynamic Paneling Ideализation for the X-29A Vertical Tail

3.4 Flutter and Divergence Analyses

In this section, the flutter/divergence analyses performed on the FSW X-29A are described. Three different techniques were used for the analyses: the k, p-k, and ASE methods. A discussion of the theory for each solution technique is given in sub-section 3.4.1, the results are presented in sub-section 3.4.2, and the conclusions are presented in sub-section 3.4.3.

3.4.1 Theory

Flutter can be defined as the dynamic instability of an elastic body in an airstream (Reference 14). Thus, such an analysis is vital for revealing any potential flutter mechanisms within the flight envelope. Three different flutter analysis techniques were performed on the X-29A--the k, or "American" method; the p-k, or "British" method; and an ASE, or state-space, method. The theory of each technique is presented briefly below.

The general flutter equation can be written in the matrix form as seen in Equation 3.1. Both the k and p-k methods of solution (References 15, 16, and 17) can be derived from this starting point.

$$M\ddot{q} + Kq - (1/2)\rho V^2 Aq = 0 \quad (3.1)$$

where M , K , and A represent the generalized mass, stiffness, and aerodynamics matrices, respectively; q is a vector of generalized displacements. The term $(1/2)\rho V^2$ is the dynamic pressure where ρ is the density and V is the freestream velocity. The matrix K defines the elastic characteristics by relating the vector of generalized forces, Q , to generalized displacements q , as shown below.

$$Kq = Q \quad (3.2)$$

In Equation 3.3, the matrix M defines the inertia characteristics by relating the inertia forces, Q_{in} , to the generalized accelerations.

$$\mathbf{Q}_{in} = -\mathbf{M}\ddot{\mathbf{q}} \quad (3.3)$$

The matrix \mathbf{A} defines the unsteady aerodynamic forces in Equation 3.4.

$$\mathbf{Q}_{aero} = (1/2) \rho V^2 \mathbf{A} \dot{\mathbf{q}} \quad (3.4)$$

Now, using a non-dimensional operator, $p = (b/V)(d/dt)$, where b represents the reference semi-chord, Equation 3.1 can be recast as shown below.

$$[(V/b)^2 M p^2 + K - (1/2) \rho V^2 A(p)] q = 0 \quad (3.5)$$

For non-zero solutions of q , the determinant formed by the matrix coefficients in Equation 3.5 must be equal to zero. Thus, for a given value of V , the velocity, the determinant can be solved directly for p . This leads to conjugate complex roots as shown in Equation 3.6.

$$p = \gamma k \pm ik \quad (3.6)$$

where k defines the non-dimensional reduced frequency $\omega b/V$, where ω is the frequency, i represents the imaginary number $\sqrt{-1}$, and γ defines a rate of decay as in Equation 3.7.

$$\gamma = [1/(2\pi)] \ln(a_{n+1}/a_n) \quad (3.7)$$

In the above equation, a_{n+1} and a_n are the amplitudes of successive cycles. For the k -method solution technique, the motion is assumed to be simple harmonic, i.e.,

$$p = ik \quad (3.8)$$

Also, for the k-method, an artificial damping term, g, is introduced by multiplying the stiffness matrix by the complex scalar $(1 + i\cdot g)$. Thus, Equation 3.5 can be recast as below.

$$[\{(k/b)^2 M + (1/2) \rho A(i\cdot k)\} \{-V^2/(1+i\cdot g)\} + K] q = 0 \quad (3.9)$$

This is the traditional "American" form, or k-method form of the flutter equation. With this formulation, the unknown eigenvalue $\{-V^2/(1+i\cdot g)\}$ (see Equation 3.10) can be determined for chosen values of k. Results from this determination can then be plotted in the familiar V-g format.

$$\lambda_r + i\lambda_i = (1/V^2)(1+i\cdot g) \quad (3.10)$$

The p-k, or "British" method assumes a response of the form $q \cdot e^{pt}$ where p is complex as shown in Equation 3.6. No artificial damping term is included in the p-k method as is done for the k-method, however, the imaginary part of the aerodynamic matrix is multiplied arbitrarily by p/ω . Thus, the aerodynamic forces can be rewritten as shown in Equation 3.11.

$$(1/2) \rho V^2 A = (1/2) \rho V^2 A^R + \{(\rho b V)/(2k)\} A^I p \quad (3.11)$$

where A^R and A^I denote the real and imaginary matrices, respectively. Then, using the above formulation, Equation 3.1 can be rewritten as shown below.

$$(M p^2 - \{(\rho b V)/(2k)\} A^I p + K - (1/2) \rho V^2 A^R) q = 0 \quad (3.12)$$

Equation 3.12 is solved by first specifying V, and then iteratively solving the equations until the imaginary part of the solution equals the k value of the aerodynamics.

Since the p-k method does not require the inclusion of the artificial damping term, and because it partially accounts for non-oscillatory behavior, it is thought that this method does a better job than the k-method in predicting subcritical behavior. The advantage of the k-method is that the solution technique is more direct, and thus less expensive in terms of solution time. However, both methods should predict the same dynamic instability speeds.

The following is the development of the flutter solution technique using the aeroservoelastic method (References 2, 4, 5 and 6). This technique is a state-space formulation, which is obtained by approximating the aerodynamic influence coefficient matrix. The development (Reference 2) starts with the basic equations of motion for an elastic airplane, as seen in Equation 3.13.

$$M\ddot{q} + C_D\dot{q} + Kq + QA_e(k_i)q = P(t) \quad (3.13)$$

where

K is the elastic stiffness matrix

M is the inertia matrix

C_D is the damping matrix

Q is the dynamic pressure, $Q = \rho V^2/2$

k_i is the reduced frequency $\omega b/V$, ω and b being the natural frequency and wing semi-chord length, respectively

A_e is the aerodynamic matrix, calculated for given Mach number and k_i

q is the displacement vector, and

P(t) is the external forcing function.

Using the STARS program, the associated free vibration problem is solved, yielding the desired eigenvalues, ω , and mode shape vectors, ϕ . A coordinate transformation as shown in Equation 3.14 is then applied to Equation 3.13. The result is Equation 3.15.

$$q = \phi\eta \quad (3.14)$$

$$\phi^T M \ddot{\eta} + \phi^T C_D \dot{\eta} + \phi^T K \eta + Q \phi^T A_e(k_i) \phi \eta = \phi^T P(t) \quad (3.15)$$

Rearranging, Equation 3.15 now becomes:

$$\hat{M} \ddot{\eta} + \hat{C}_D \dot{\eta} + \hat{K} \eta + Q \hat{A}_e(k_i) \eta = \hat{P}(t) \quad (3.16)$$

where the generalized coordinate $\eta = [\eta_R \ \eta_\varepsilon \ \eta_\delta]$ and the modal matrix $\phi = [\phi_R \ \phi_\varepsilon \ \phi_\delta]$, incorporate rigid-body, elastic, and control surface motions, respectively.

Each coefficient of the generalized aerodynamic force matrix in the Laplace domain may next be expressed as Pade polynomials in $i\omega$ (or sV/b) as in Equation 3.17.

$$\hat{A}_e(k_i) = \hat{A}_0 + \frac{sb}{V} \hat{A}_1 + \frac{sb^2}{V} \hat{A}_2 + \sum_{j=1}^{NL} \frac{\hat{A}_{2+j} s}{s + \frac{V}{b} \beta_j} \quad \dots \quad (3.17)$$

where

$\hat{A}_0, \hat{A}_1, \hat{A}_2$ are the equivalent aerodynamic stiffness, damping, and inertia matrices, respectively.

\hat{A}_{2+j} are the forces due to the aerodynamic lag terms.

i is the imaginary number, $\sqrt{-1}$.

s is the Laplace variable ($i\omega$).

$(V/b)\beta_j$ is the location of the Pade pole.

NL is the order of the Pade polynomials.

The coefficients $\hat{A}_0, \hat{A}_1, \hat{A}_2, \dots$, are determined by a least squares solution using the aerodynamic coefficient data ($A_0(k_i)$) for a number of k_i values. Now, substituting Equation 3.17 into the free-vibration form of Equation 3.16, collecting like terms, and assuming two lag terms results in Equation 3.18.

$$\begin{aligned} & (\hat{M} + \left(\frac{b}{V}\right)^2 \hat{A}_2) \ddot{\eta} + (\hat{C}_D + Q \frac{b}{V} \hat{A}_1) \dot{\eta} + (Q\hat{A}_0) \eta + \\ & + Q\hat{A}_3 \frac{s}{s + \frac{V}{b} \beta_1} \eta + Q\hat{A}_4 \frac{s}{s + \frac{V}{b} \beta_2} \eta = 0 \end{aligned} \quad (3.18)$$

Equations 3.19 and 3.20 show how Equation 3.18 may be rewritten.

$$\tilde{M} \ddot{\eta} + \tilde{C}_D \dot{\eta} + \tilde{K} \eta + Q\hat{A}_3 x_1 + Q\hat{A}_4 x_2 = 0 \quad (3.19)$$

$$\begin{bmatrix} I & 0 & 0 & 0 \\ 0 & \tilde{M} & 0 & 0 \\ 0 & 0 & I & 0 \\ 0 & 0 & 0 & I \end{bmatrix} \begin{bmatrix} \dot{\eta} \\ \ddot{\eta} \\ x_1 \\ \dot{x}_2 \end{bmatrix} = \begin{bmatrix} 0 & I & 0 & 0 \\ -\tilde{K} & -\tilde{C}_D & -Q\hat{A}_3 & -Q\hat{A}_4 \\ 0 & I & -\frac{V}{b} \beta_1 & 0 \\ 0 & 0 & 0 & -\frac{V}{b} \beta_2 \end{bmatrix} \begin{bmatrix} \eta \\ \dot{\eta} \\ x_1 \\ x_2 \end{bmatrix} \quad (3.20)$$

where I is the identity matrix. Rewriting Eqn. 3.20 in simple terms yields Equation 3.21.

$$M' \dot{X}' = K' X' \quad (3.21)$$

Premultiplying both sides by the inverse of M' yields:

$$\dot{X}' = (M')^{-1} K' X' \quad (3.22a)$$

or

$$\dot{X}' = R X' \quad (3.22b)$$

The state-space vector X' is now written as below.

$$X' = [(\eta_R \ \eta_\epsilon \dot{\eta}_R \dot{\eta}_\epsilon \ x_1 \ x_2) \ (\eta_\delta \dot{\eta}_\delta)] \quad (3.23a)$$

or

$$X' = [\tilde{x} \ u] \quad (3.23b)$$

The result of expanding Equation 3.22b is shown in Equation 3.24.

$$\begin{bmatrix} \dot{\tilde{x}} \\ \dot{u} \end{bmatrix} = \begin{bmatrix} R_{I,I} & R_{I,II} \\ R_{II,I} & R_{II,II} \end{bmatrix} \begin{bmatrix} \tilde{x} \\ u \end{bmatrix} \quad (3.24)$$

The first set of equations in the above matrix equation denotes the dynamics of the plant, while the second set represents the dynamics of the control modes. Considering only the plant dynamics, the state-space equation can be written in the form as in Equation 3.25.

$$\dot{\tilde{x}} = \tilde{A} \tilde{x} + \tilde{B} u \quad (3.25)$$

In the above equation, A represents the plant dynamics matrix, and B is the control surface influence matrix. A coordinate transformation (Ref. 18) is next performed to

transform the state-space matrices from an earth-fixed coordinate system to a body-fixed coordinate system to enable the incorporation of control laws and feedback. The result is Equation 3.26.

$$\dot{\mathbf{x}} = \mathbf{A}\mathbf{x} + \mathbf{B}\mathbf{u} \quad (3.26a)$$

where

$$\mathbf{A} = [\mathbf{T}^T \mathbf{T}]^{-1} [\mathbf{T}^T \tilde{\mathbf{A}} \mathbf{T}] \quad (3.26b)$$

$$\mathbf{B} = [\mathbf{T}^T \mathbf{T}]^{-1} [\mathbf{T}^T \tilde{\mathbf{B}}] \quad (3.26c)$$

In Equation 3.26, \mathbf{T} represents the relevant transformation matrix. Finally, the aeroelastic stability analysis can be solved over various dynamic pressures, with the solution of the eigenvalue problem as seen in Equation 3.27.

$$|\mathbf{A} - \lambda \mathbf{I}| = 0 \quad (3.27)$$

The roots of which are complex, as below in Equation 3.28.

$$\lambda = -\alpha \pm i\beta \quad (3.28)$$

An instability of the system, i.e., flutter, is indicated by a change in sign (from negative to positive) of the real part, α , of an eigenvalue, λ . Divergence is noticed if the corresponding frequency, the imaginary part, β , of the eigenvalue, λ , approaches zero. Since modal damping is proportional to $\tan(\alpha / \beta)$, (Ref. 6), the eigenvalue solution as in Equation 3.28 can be used to plot the results in a typical V-g diagram. These plots are useful in qualitatively assessing the nature of flutter onset, and will be discussed in detail in the next section.

3.4.2 Correlation of Flutter/Divergence Analyses

In this section, the results of extensive flutter/divergence analyses performed for the symmetric and anti-symmetric cases of the X-29A are presented. All analyses were performed with doublet lattice unsteady aerodynamics, assuming 0.90 Mach number and sea level air density. The results are presented in two parts. The symmetric results are presented first, followed by the anti-symmetric results. Both parts compare the various solution techniques described earlier by V-g diagrams and root-locus plots.

3.4.2.1 Symmetric Analyses

The symmetric results comparing the STARS k, p-k, and ASE analytical methods to the Ground Vibration Survey (GVS) performed at NASA are shown in Table 3.3. As can be seen, good correlation exists between the GVS and the three analytical techniques. Figures 3.15 through 3.22 show comparative V-g diagrams for the k-method, p-k method, and the state-space (ASE) method flutter analyses of the X-29A. The V-g diagrams indicate oncoming divergence when both the damping, g , and frequency, ω , approach zero. Flutter is indicated when there is positive frequency, but the damping term crosses the imaginary axis, becoming unstable. In comparing the k-method to the p-k and state-space methods, it is generally found that the p-k damping term is consistent with that of the k-method, while the state-space damping term is more conservative. This could be explained since modal damping, g , is plotted for the k and p-k methods, while the proportional term (α / β) is plotted as damping for the state-space method. This is shown on Figure 3.15, and is the same for all V-g plots. Usually, the slope of the damping curve is the most observed result, though, as this indicates how fast the onset of the flutter or divergence instability will occur.

Figure 3.15 shows the primary mode leading to wing divergence (W1B). The ASE method predicts divergence at 834 kts, a 0.5% difference from the k-method, while the p-k method predicts divergence at 900 kts, a 7.4% difference. In the ASE and p-k solutions, the frequencies become zero before the damping goes unstable, indicating a non-oscillatory motion before divergence. The ASE frequency becomes zero at approximately 800 kts, while the p-k frequency becomes zero at approximately 890 kts.

The k method predicts oscillatory motion up to the point of divergence. Thus, at this point, the k and p-k results are consistent with the theory described earlier. Figure 3.16 shows the F1B V-g plot. The ASE method predicts a 6% lower flutter speed than the k-method, while the p-k predicts a 5.5% higher flutter speed. All methods show relatively low damping for the fuselage mode. The V-g plot for the F2B mode is shown in Figure 3.17. The k, p-k, and state-space damping curves are similar in shape, however, the frequency for the p-k and state-space methods differs slightly at higher velocities. Figure 3.18 shows the primary mode (CP) leading to canard divergence. The ASE method predicts divergence at 918 kts, 0.5% higher than the k-method. The p-k method also shows good correlation to the k-method, predicting divergence at 920 kts, a 0.7% difference. Again, as in the W1B divergence, non-oscillatory motion occurs in the state-space and p-k methods slightly before divergence, at 900 and 915 kts, respectively. Figure 3.19 shows the V-g plot for the W2B mode. The ASE method predicts flutter at 1,157 kts, or 1.2% lower than the k-method, while the p-k method predicts flutter at 1,216 kts, 6.4% higher than the k-method. Figures 3.20 through 3.22 show the V-g plots for the W1T, CBP, and W3B modes, respectively. These plots show good correlation of the damping and frequency terms, and no flutter or divergence is indicated at the conditions tested. While there is a difference in the magnitude of the damping term between the state-space method and the k and p-k methods, the slope of the curves at the instabilities for all three methods are similar.

Using a root-locus type plot, the modes can easily be traced, showing any flutter or divergence characteristics. Figure 3.23 shows the root-locus of the symmetric modes, taken from the state-space method results. The real (α) and imaginary (β) parts of the eigenvalue problem, as in Equation 3.28, are plotted for various dynamic pressures. Figures 3.24 and 3.25 show the root-locus plots for the k and p-k methods, respectively. On the real axis the damping term $g \cdot \omega$ (damping x frequency) is plotted, while the frequency is plotted on the imaginary axis. Note, in Figure 3.24, the k method results show the frequency and damping terms simultaneously approaching zero values for the W1B and CP modes, indicating divergence. In Figures 3.23 and 3.25, the ASE and p-k methods, respectively, the frequency becomes zero first, then the roots split on the x-axis, with one root going unstable, indicating divergence. This is consistent with the theory for the k and p-k methods, and with the V-g diagrams presented earlier. The k, p-k, and state-space

methods, however, all have similar results for the other roots. Again, note, for the F1B and W2B modes, the roots change signs, becoming 'positive', indicating an instability. Since the frequency is not approaching zero, the instability is flutter.

Table 3.3 Comparison of X-29A Flutter/Divergence Solutions,
Symmetric Case

<u>Mode</u>	<u>Instability</u>	<u>STARS (k)</u>	<u>STARS (p-k)</u>	<u>STARS (ASE)</u>	<u>GVS</u>
W1B	Div.	838	900	834	808
CP	Div.	913	920	918	980
F1B	Flutter	848	895	797	924
W2B	Flutter	1143	1216	1157	1315

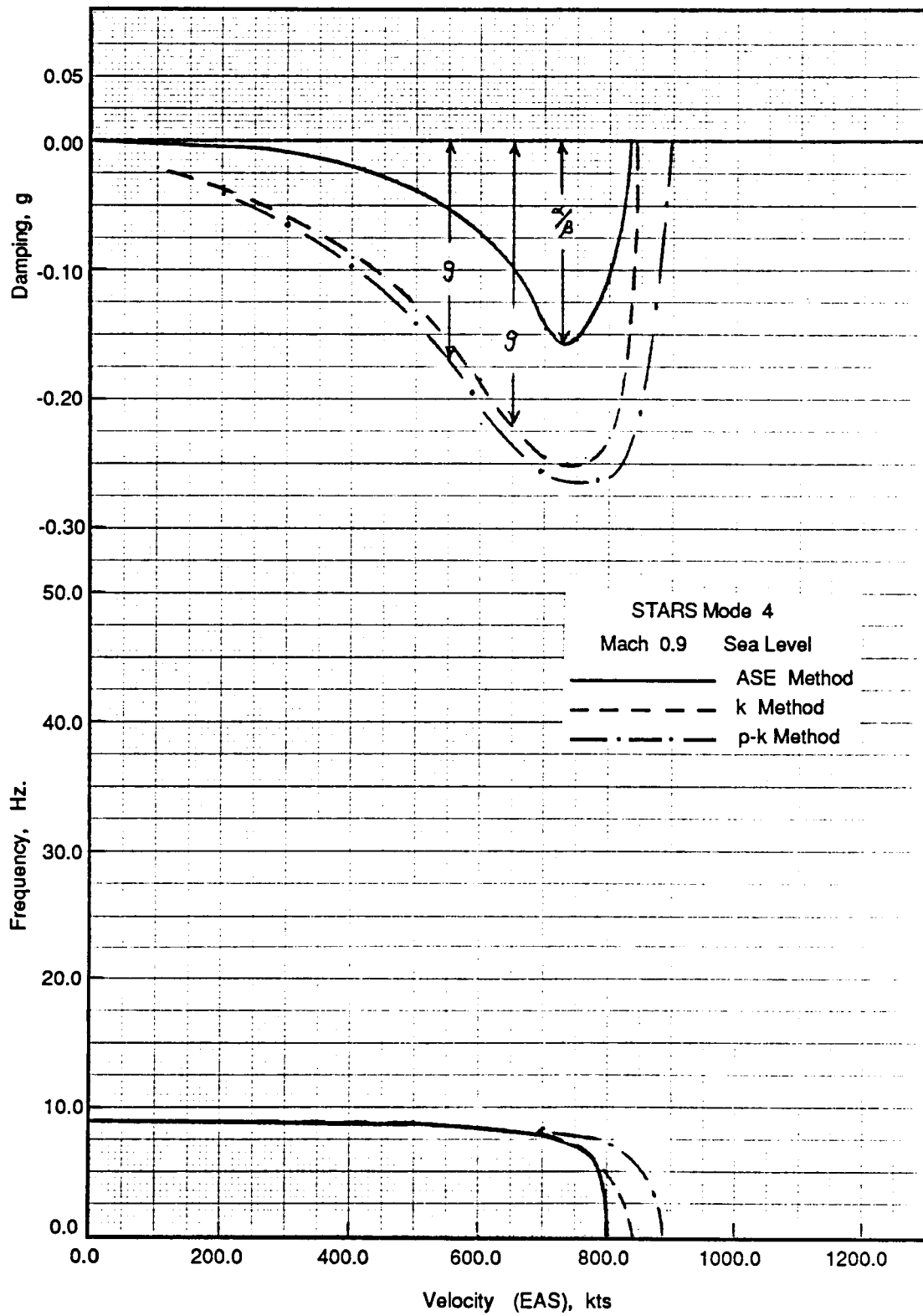


Figure 3.15 V-g Plot of k, p-k, and ASE Methods for Symmetric X29A, W1B

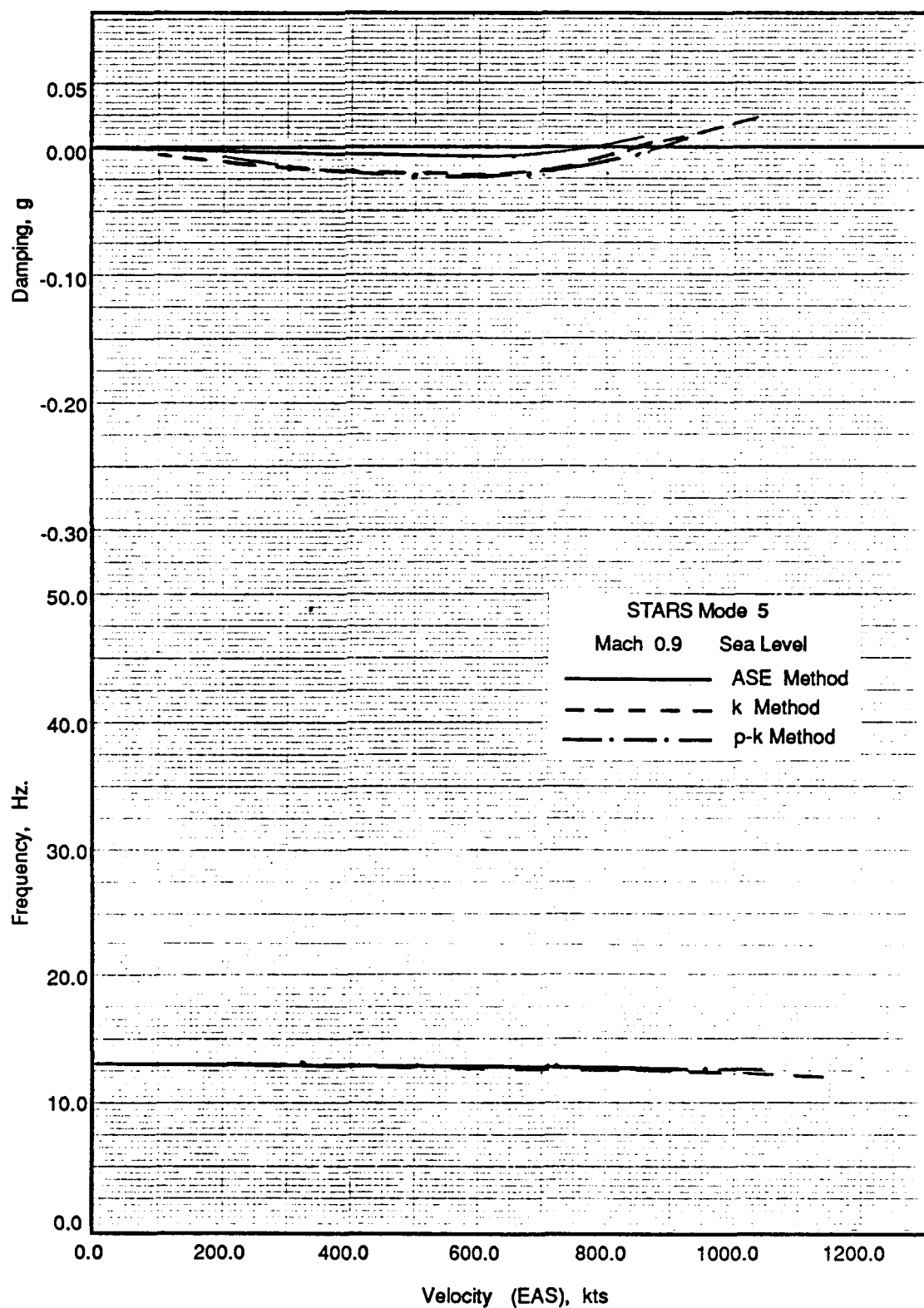


Figure 3.16 V-g Plot of k, p-k, and ASE Methods for Symmetric X29A, F1B

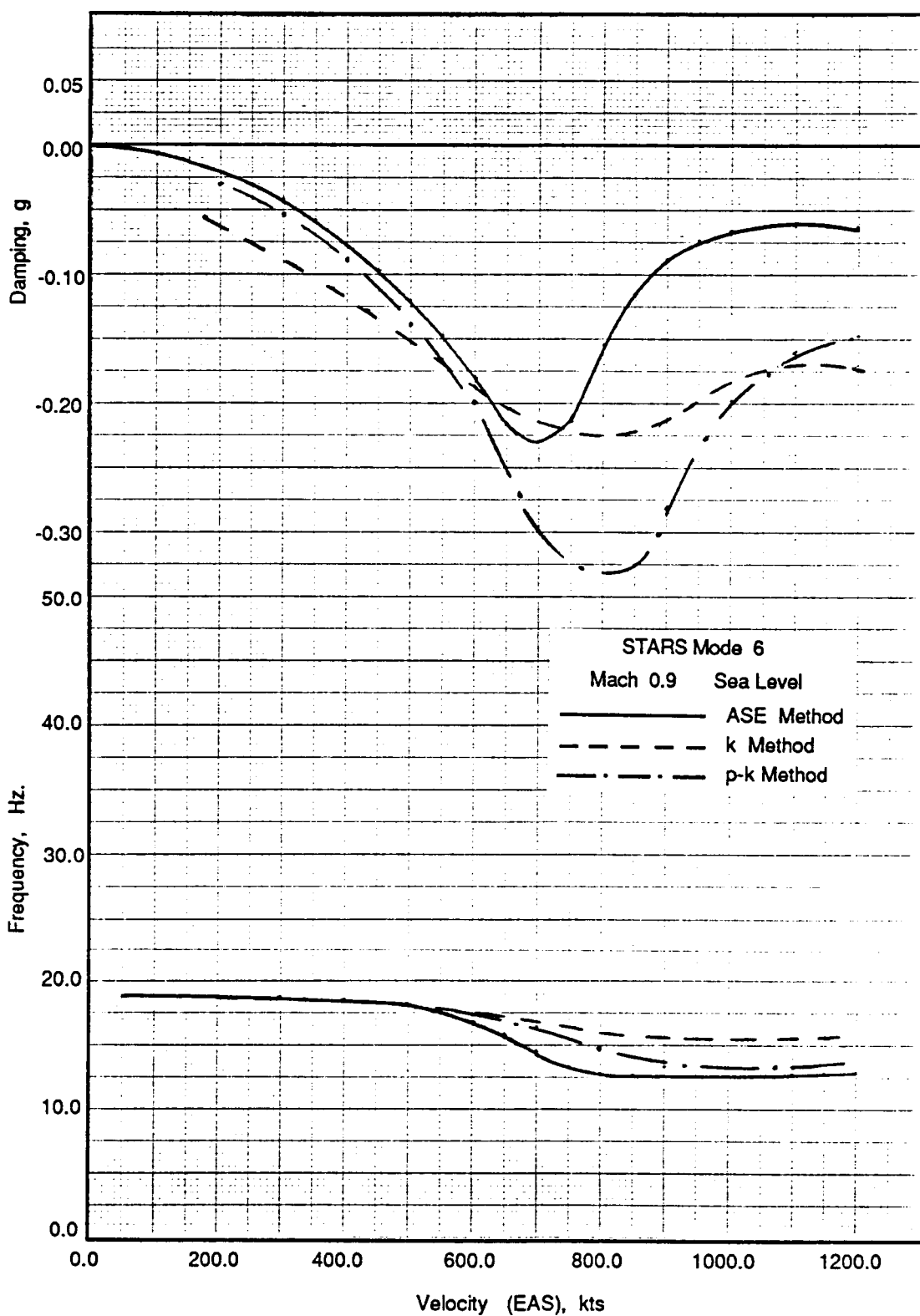


Figure 3.17 V-g Plot of k, p-k, and ASE Methods for Symmetric X29A, F2B

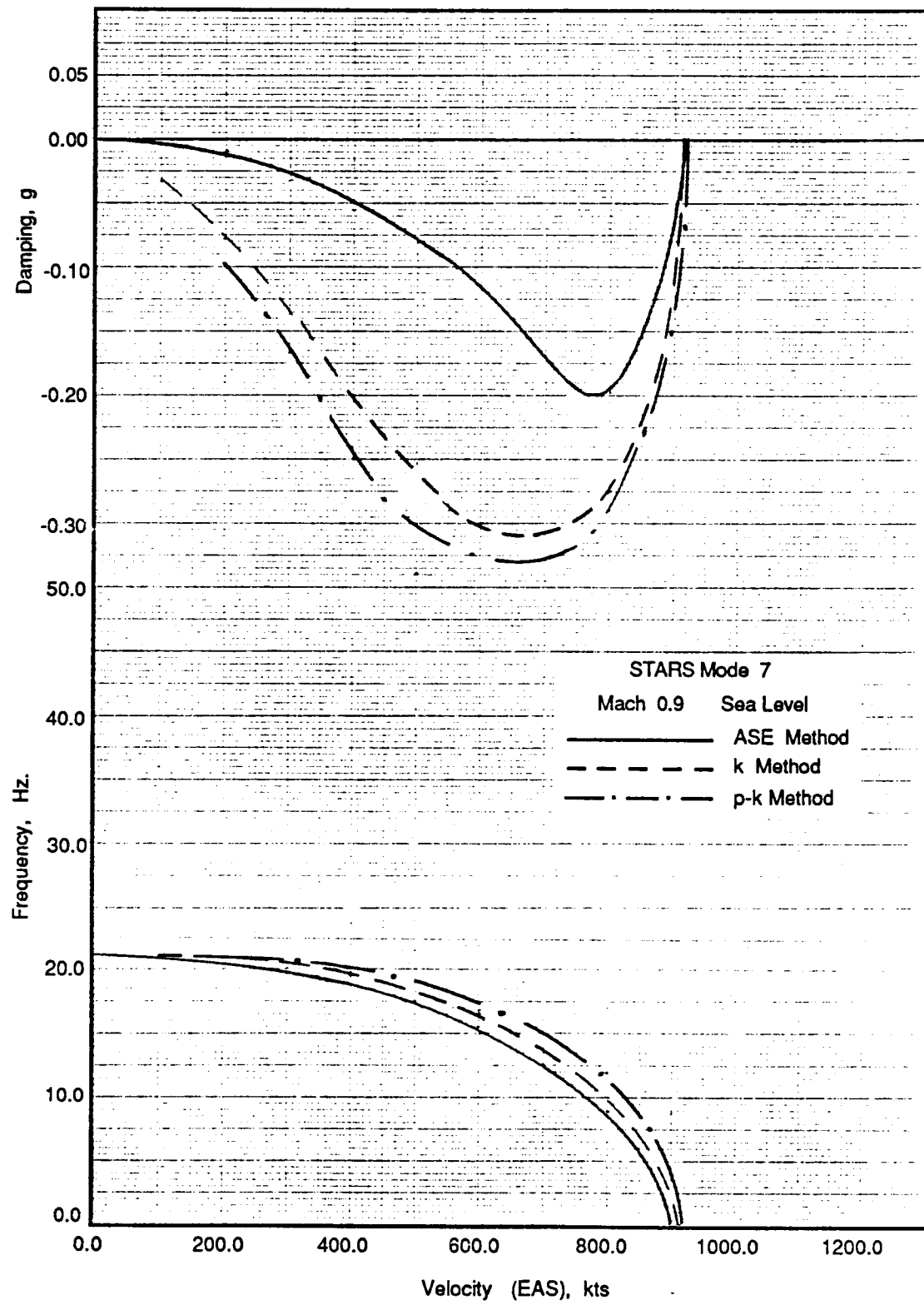


Figure 3.18 V-g Plot of k, p-k, and ASE Methods for Symmetric X29A, CP

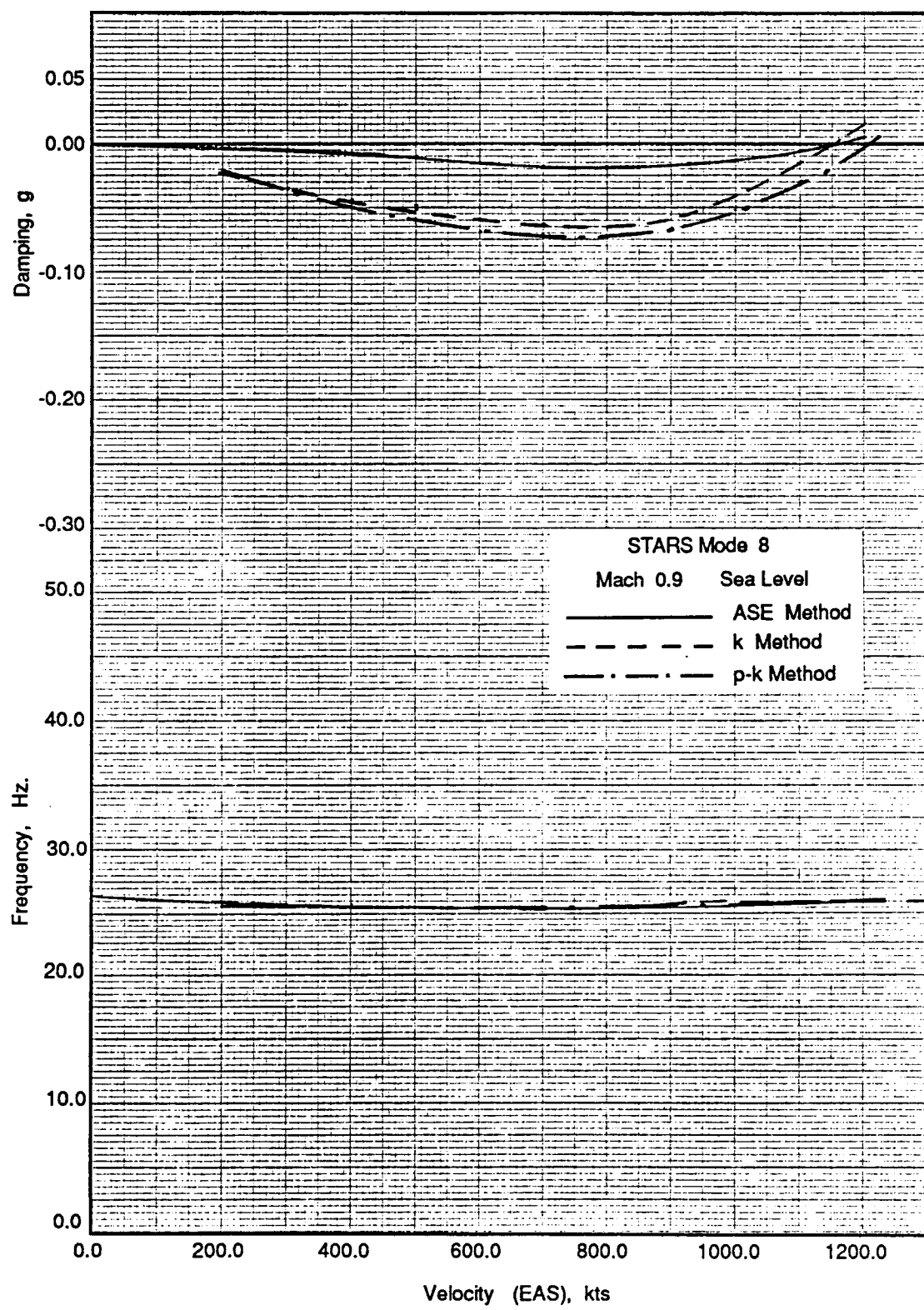


Figure 3.19 V-g Plot of k, p-k, and ASE Methods for Symmetric X29A, W2B

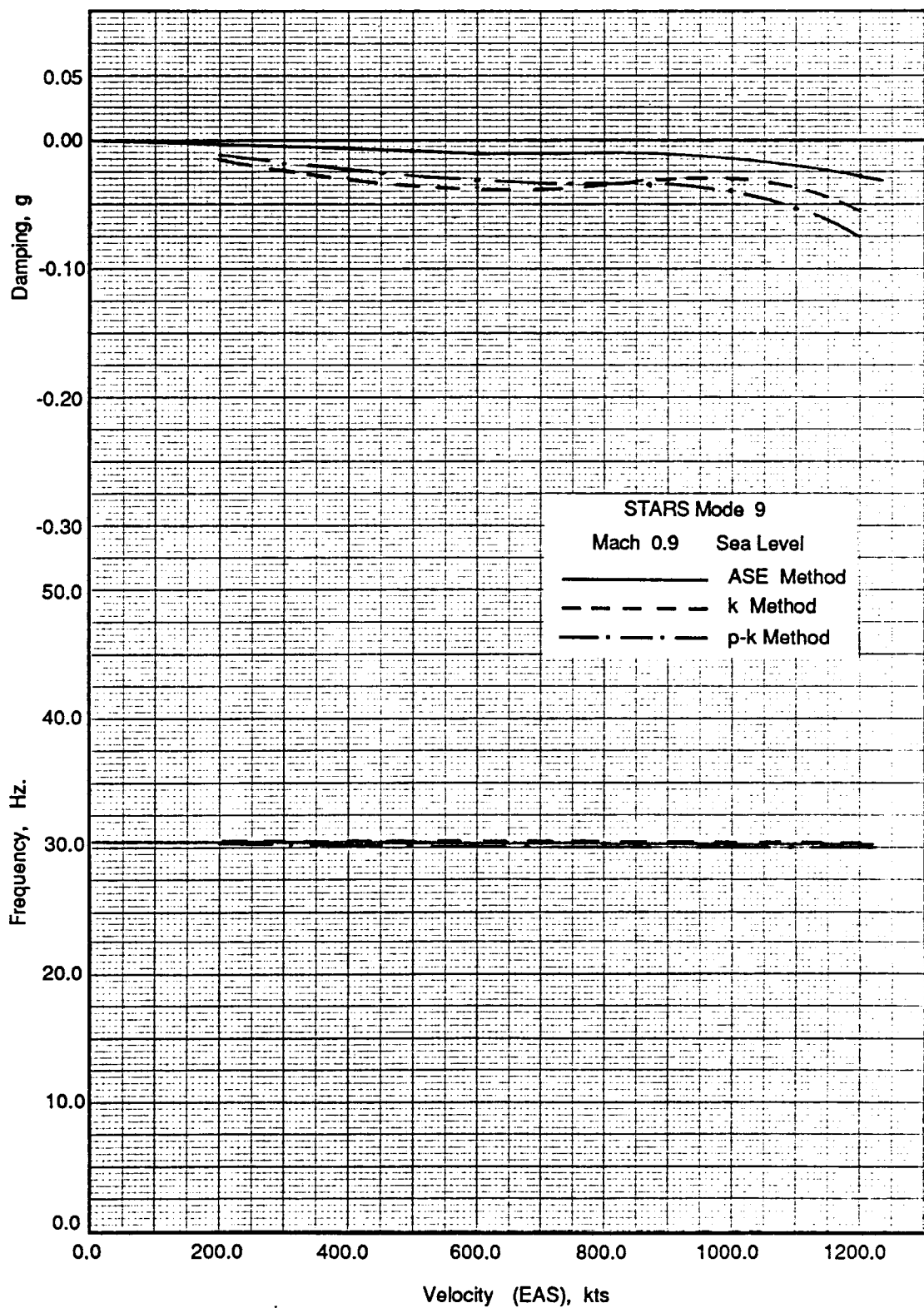


Figure 3.20 V-g Plot of k, p-k, and ASE Methods for Symmetric X29A, W1T

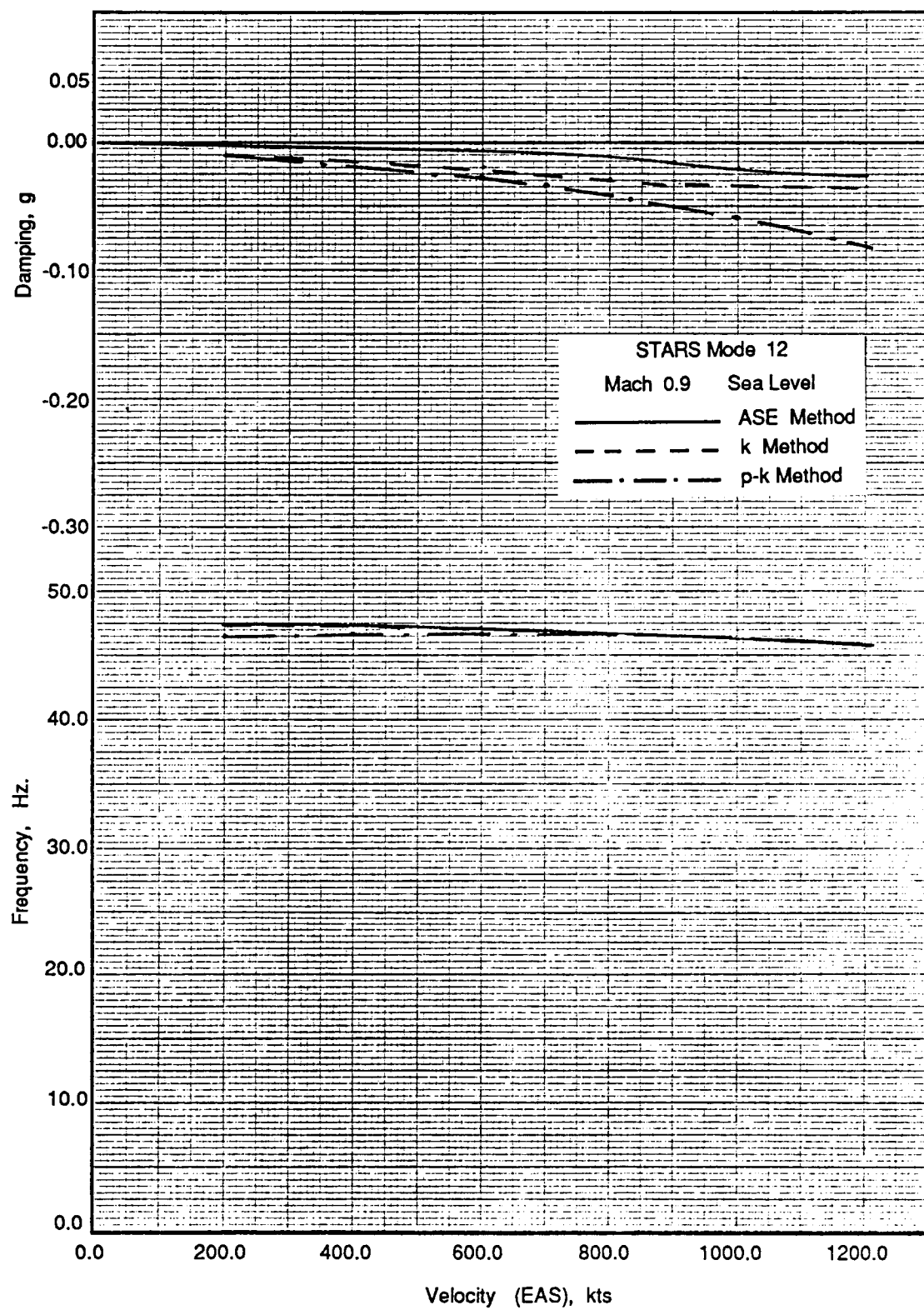


Figure 3.21 V-g Plot of k, p-k, and ASE Methods for Symmetric X29A, CBP

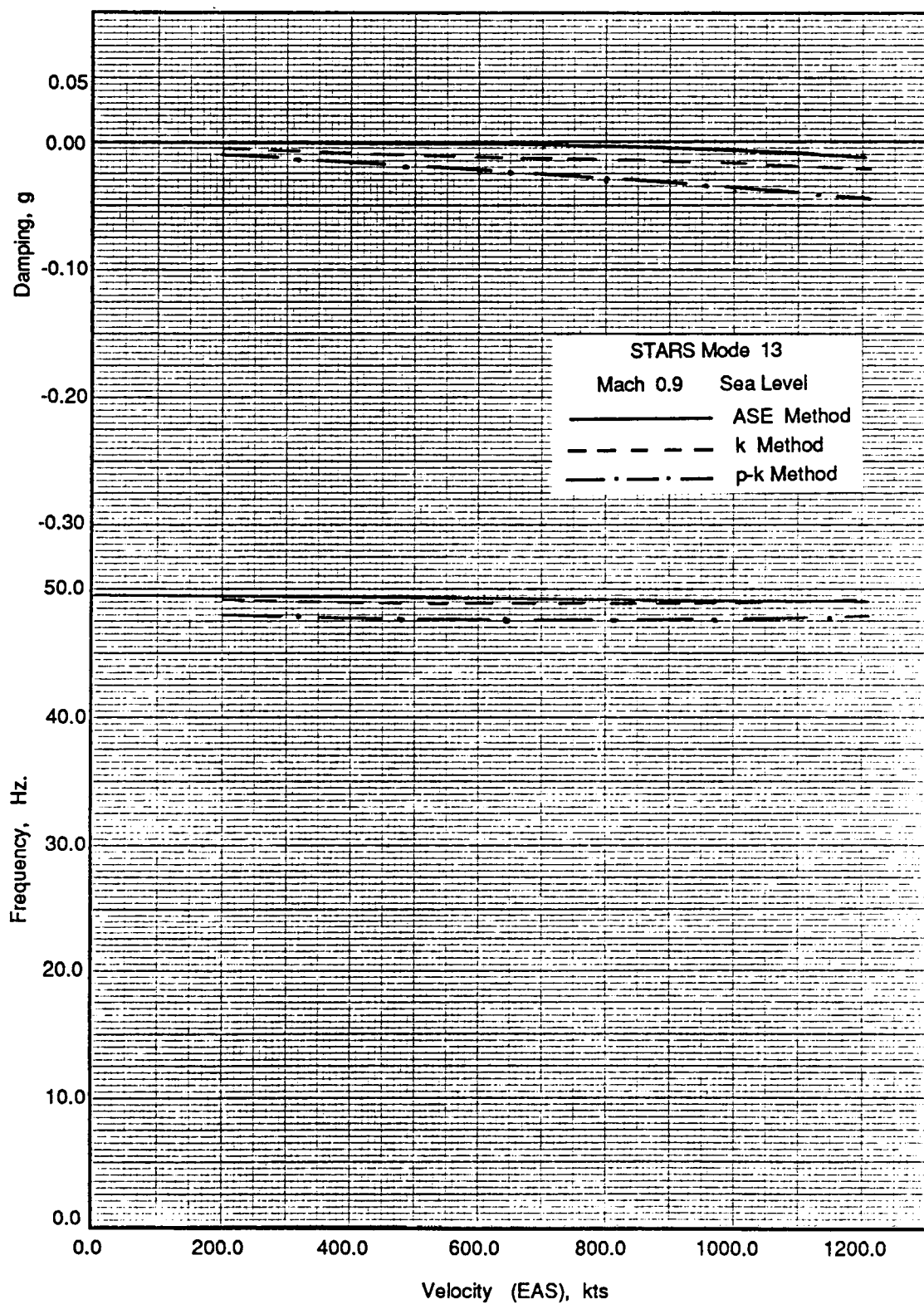


Figure 3.22 V-g Plot of k, p-k, and ASE Methods for Symmetric X29A, W3B

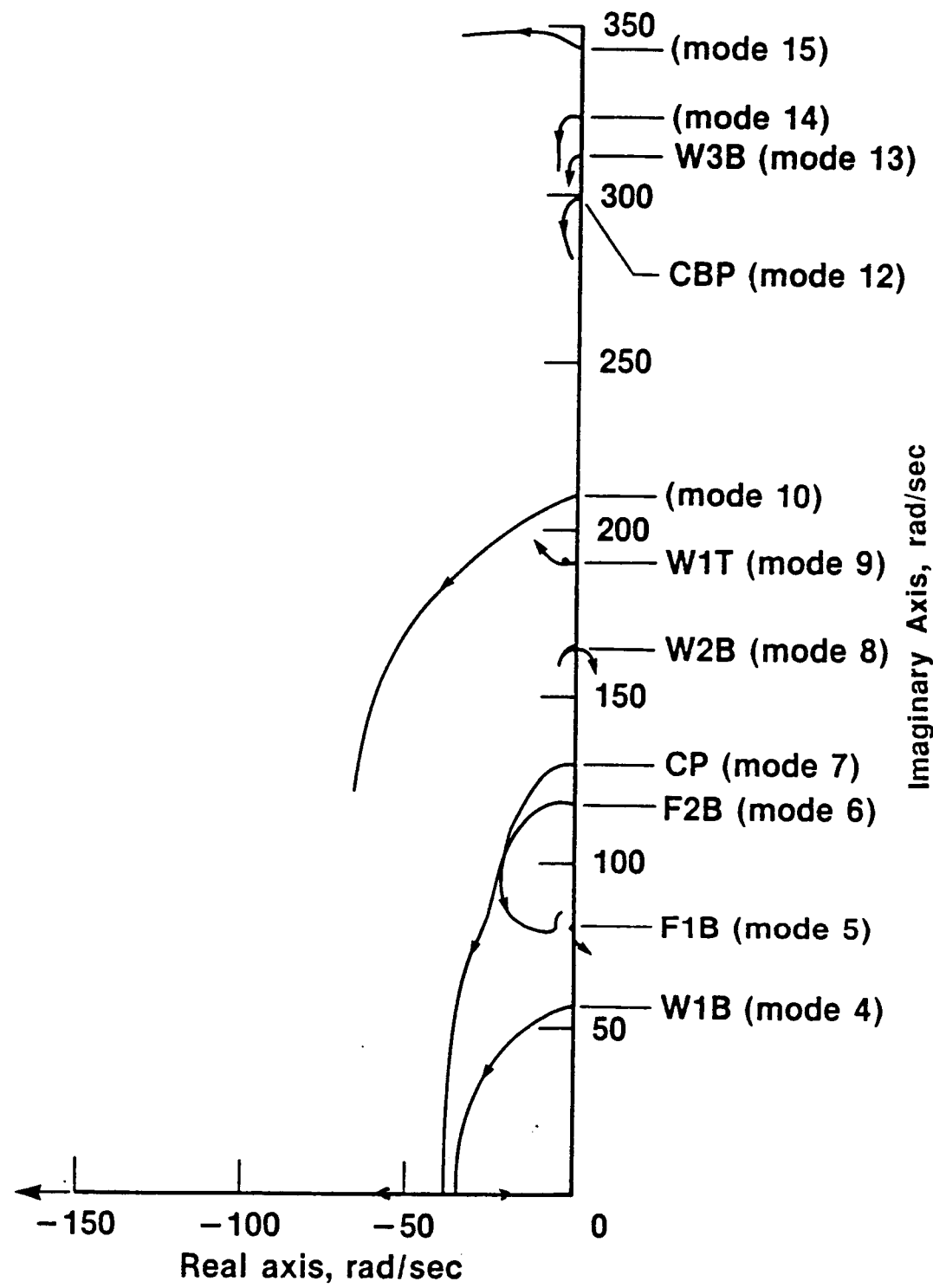


Figure 3.23 Symmetric X-29A Structural Root-Locus -- State-space Method, Arrows Indicate Increasing Dynamic Pressure

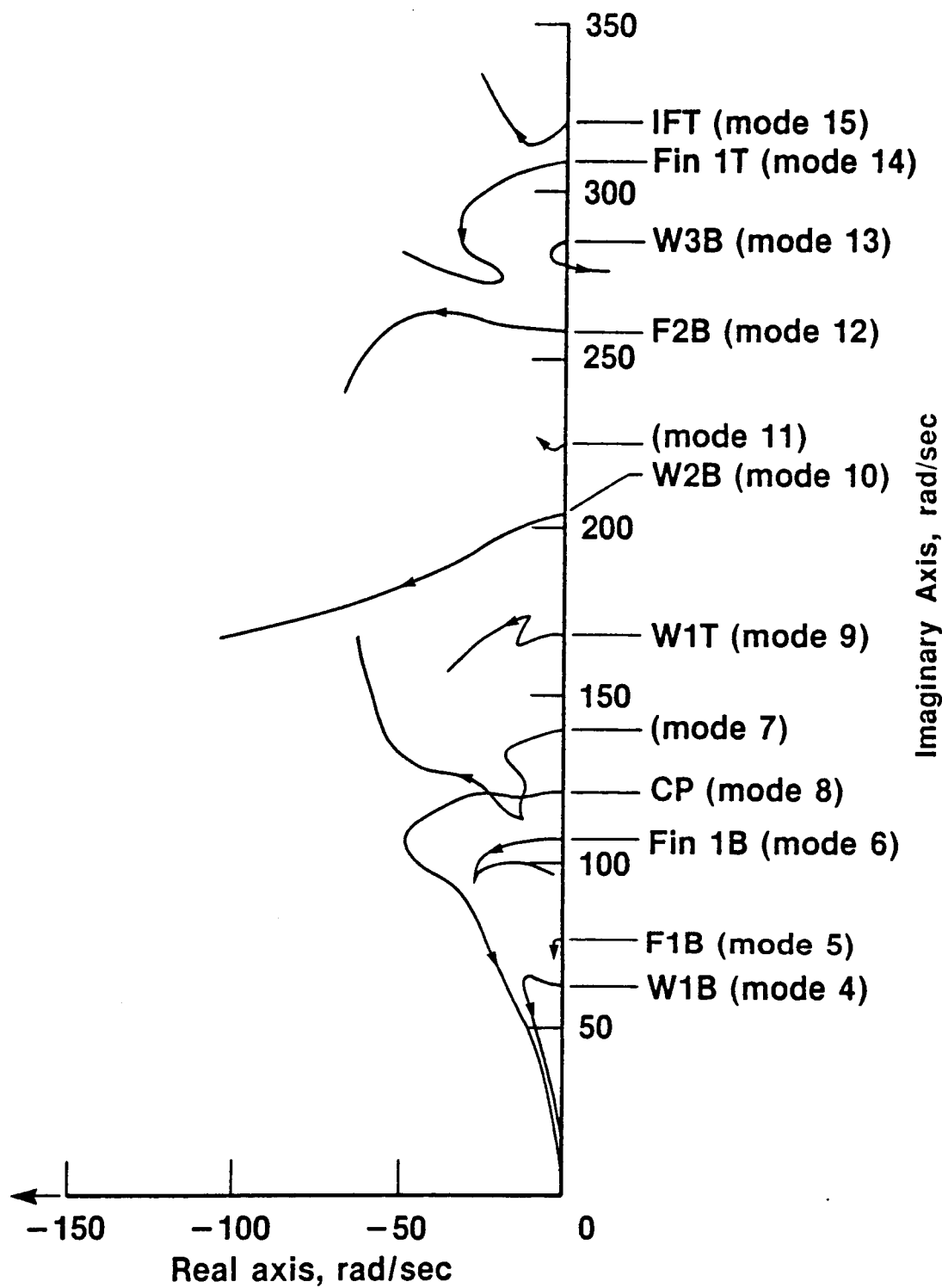


Figure 3.24 Symmetric X-29A Structural Root-Locus -- k Method,
Arrows Indicate Increasing Dynamic Pressure

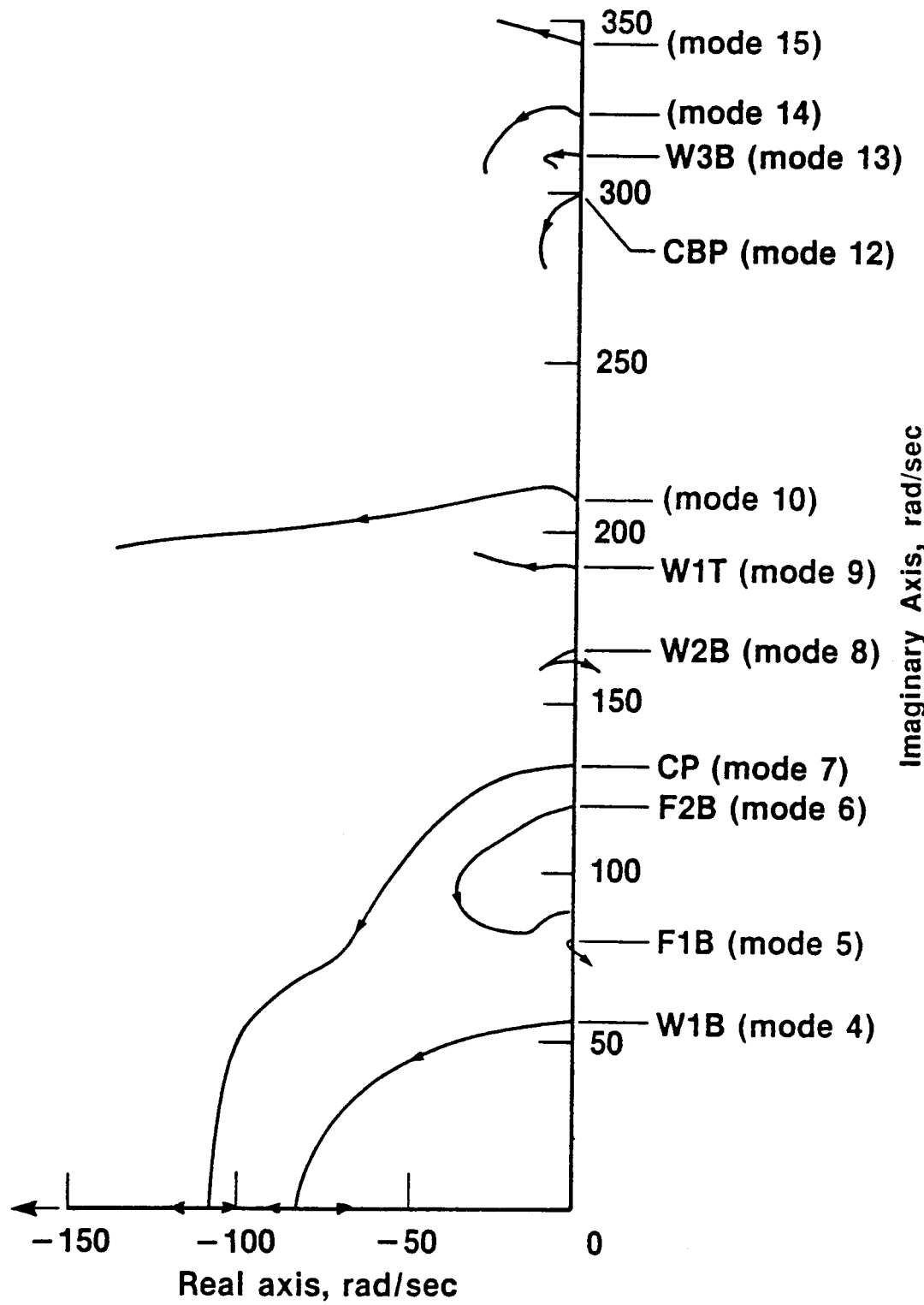


Figure 3.25 Symmetric X-29A Structural Root-Locus -- p-k Method,
Arrows Indicate Increasing Dynamic Pressure

3.4.2.2 Anti-symmetric Analyses

In this section, the results of two distinct analyses performed on the anti-symmetric X-29A are presented. In the first analysis, the three flutter solution techniques discussed earlier were performed on the elastic X-29A, i.e., only the elastic mode shapes and forces were included in the analyses, as was done in the symmetric case. The results of this flutter analysis are summarized in Table 3.4. Figures 3.26 through 3.31 show V-g diagrams comparing the analyses performed, the k, p-k, and the state-space methods for this analysis. In the second analysis, the three flutter solution techniques were performed on the X-29A in which the elastic and rigid body mode shapes and forces were included in the calculations. Figures 3.35 through 3.37 show a few of these results in comparative V-g diagrams. A complete description of the the results follow.

Figure 3.26 shows the comparative V-g plot for the anti-symmetric W1B mode. The state-space method predicts divergence at 900 kts, 8.0% higher than the k-method, while the p-k method predicts divergence at 920 kts, 10.4% higher than the k-method. The ASE and p-k methods both predict non-oscillatory motion at approximately 2 kts before divergence. The non-oscillatory motion occurs much closer to the instability speed in the anti-symmetric case than in the symmetric case. This could be due to subtle differences in the aero modeling, however, a detailed study would need to be conducted to determine the causes. Figure 3.27 shows the V-g plot for the anti-symmetric F1B mode. The k and state-space methods do not predict flutter, as the GVS, however the p-k method predicts flutter at 1,273 kts. The damping for all three analytical analyses is shallow, and minor differences in modeling or numerical solutions could show the instability. Figure 3.28 shows the anti-symmetric Fin 1B mode. The damping and frequency curves follow each other very well in shape, however, in the state-space method the damping is considerably less than that experienced in the symmetric case. Figure 3.29 shows the divergent CP mode for the anti-symmetric case. The ASE method predicts divergence at 814 kts, 10.7% lower than the k-method. The p-k method predicts divergence at 1360 kts, 49.1% higher than the k-method. This large discrepancy may be attributed to the coupling of modes, as will be discussed shortly. Figure 3.30 shows the anti-symmetric W2B mode. The frequency curves agree well for all three solution techniques, however the p-k damping curve differs significantly from the state-space and k methods. Figure 3.31 shows the W3B mode. Both

the k and ASE methods predict flutter, the ASE method predicting flutter at 1,338 kts, 4.9% higher than the k method. However, in the p-k analysis, no instability was detected.

Figures 3.32 through 3.34 show the structural root-locus plots for the anti-symmetric analysis in which only the elastic modes are included. The root-locus plots are shown for the ASE, k, and p-k methods in Figures 3.32, 3.33, and 3.34, respectively. In the ASE and p-k root-locus plots, the W1B mode shows non-oscillatory divergence, while the k method indicates oscillatory motion up to divergence, as the damping and frequency curves simultaneously approach zero. The shape of the F1B mode shows flutter, however the k and state-space methods do not indicate flutter in the velocity region checked. In the STARS analysis, mode 8 is the canard pitch mode. Checking the three root-locus plots, however, mode 7 indicates divergence. Since mode 8 crosses mode 7, coupling is assumed, and thus the canard pitch mode diverges. It is assumed that this coupling phenomenon causes numerical problems for the iterative solution technique used by the p-k method. The other modes are indicated on the root-locus plots. Note, the W3B mode shows flutter in both the k and ASE methods, and the shape of the p-k solution is similar, however flutter is not indicated in the velocity region analyzed.

A study was also performed, as mentioned earlier, to determine the effect of the rigid body mode shapes and forces in the flutter/divergence analysis. Three comparative V-g plots are shown in Figures 3.35 through 3.37. Figure 3.35 shows the W1B mode when the rigid body modes are included in the calculations. All three plots show similar shapes, except only the p-k method shows the flutter instability at 870 kts. Figure 3.36 shows the CP anti-symmetric mode with the inclusion of rigid body modes. The ASE method shows CP divergence at 870 kts, while the k method shows flutter at 850 kts. The p-k method shows divergence at 1,360 kts. Again, there is very poor correlation between the p-k method and the ASE and k methods. Figure 3.37 shows the W3B mode for the rigid body anti-symmetric analysis. The k and state-space methods both predict flutter, and in the p-k method no flutter is indicated as in the elastic anti-symmetric case. A summary of the anti-symmetric flutter analysis including the rigid body mode shapes and forces is given in Table 3.5.

Figures 3.38 through 3.40 show the root-locus plots for the anti-symmetric case including the rigid body mode shapes (modes 1 - 3). The root-locus plots show the ASE, k, and p-k methods in Figures 3.38, 3.39, and 3.40, respectively. Of the rigid body modes,

two are shown diverging for all three cases. Since the W1B mode does not diverge in the three cases, it is assumed that coupling occurs with one or all of the rigid bodies. The other modes are shown, most of them similar to the elastic root-locus plots.

Table 3.4 Comparison of X-29A Flutter/Divergence Solutions.
Anti-symmetric Case

<u>Mode</u>	<u>Instability</u>	<u>STARS (k)</u>	<u>STARS (p-k)</u>	<u>STARS (ASE)</u>	<u>GVS</u>
W1B	Div.	833	920	900	865
CP	Div.	912	1360	814	1017
CBP	Flutter	—	—	—	694
W3B	Flutter	1275	—	1338	1222
F1B	Flutter	—	1273	—	—

Table 3.5 Comparison of X-29A Flutter/Divergence Solutions.
Anti-symmetric Case Including Rigid Body Modes

<u>Mode</u>	<u>Instability</u>	<u>STARS (k)</u>	<u>STARS (p-k)</u>	<u>STARS (ASE)</u>
W1B	Flutter	—	870	—
F1B	Flutter	1926	1317	—
CP	Div.	850 (flutter)	1360	870
W2B	Flutter	1320	—	—
W3B	Flutter	1269	—	1338

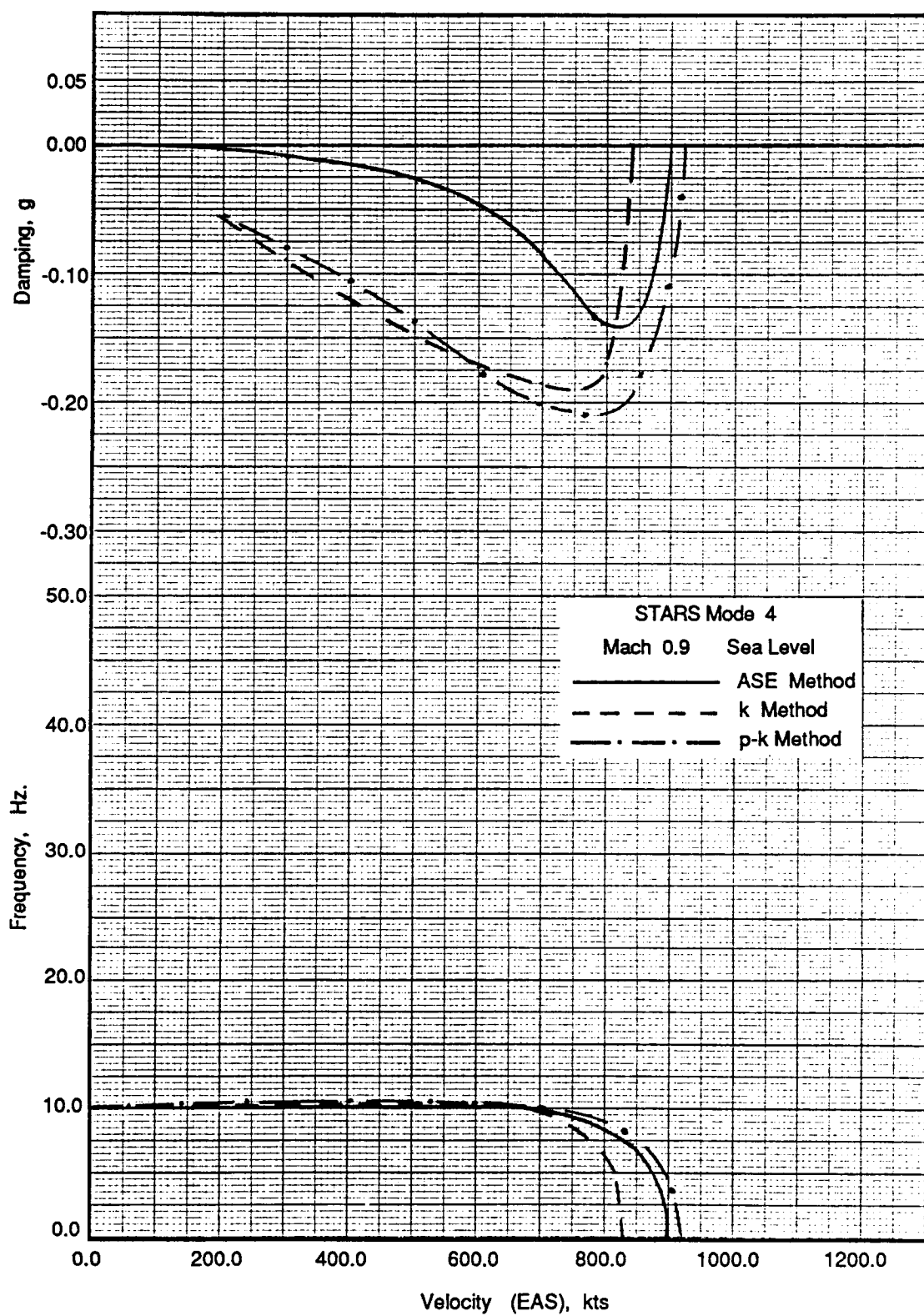


Figure 3.26 Comparative V-g Plot of the Anti-symmetric X29A, W1B Mode

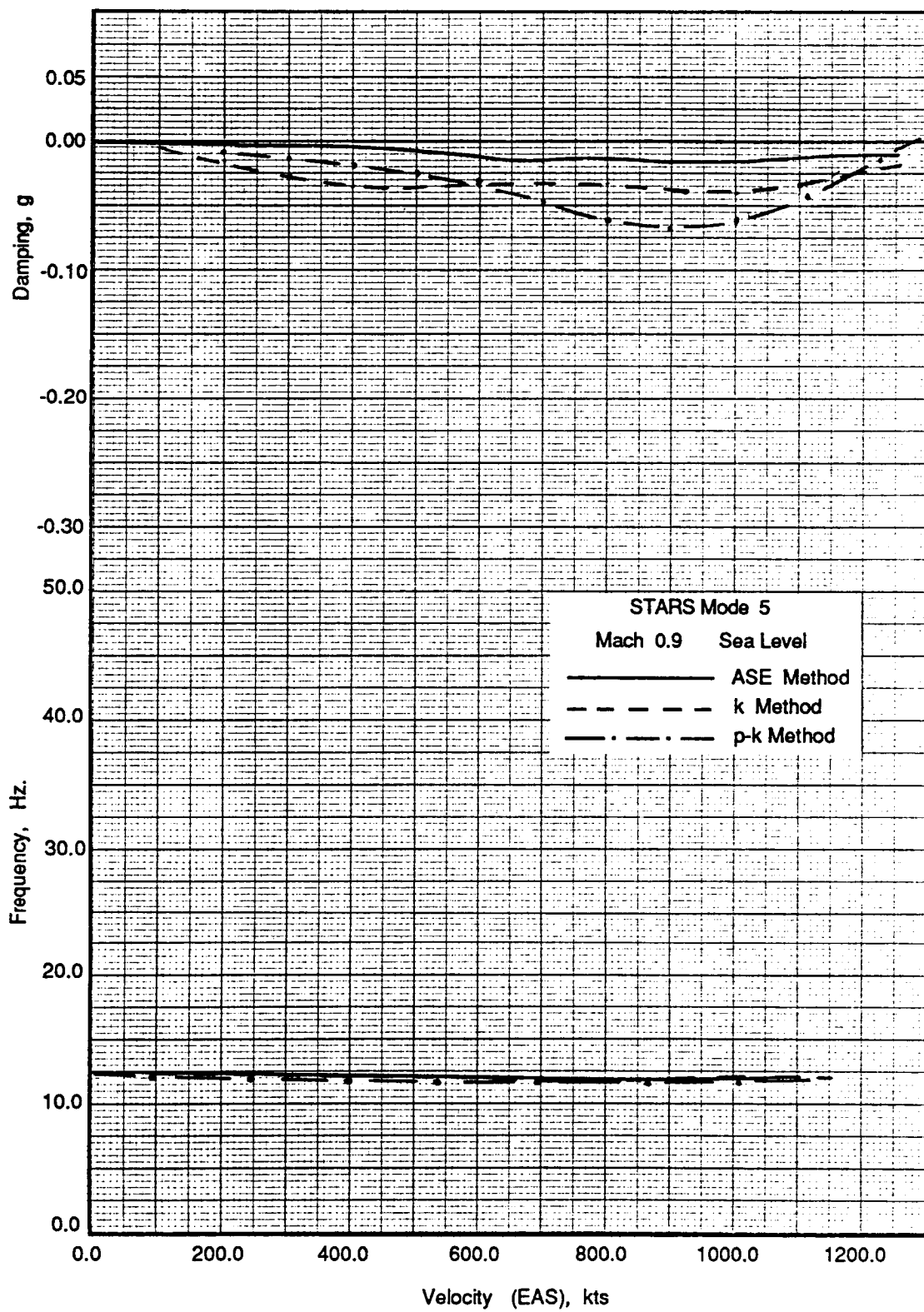


Figure 3.27 Comparative V-g Plot of the Anti-symmetric X29A, F1B Mode

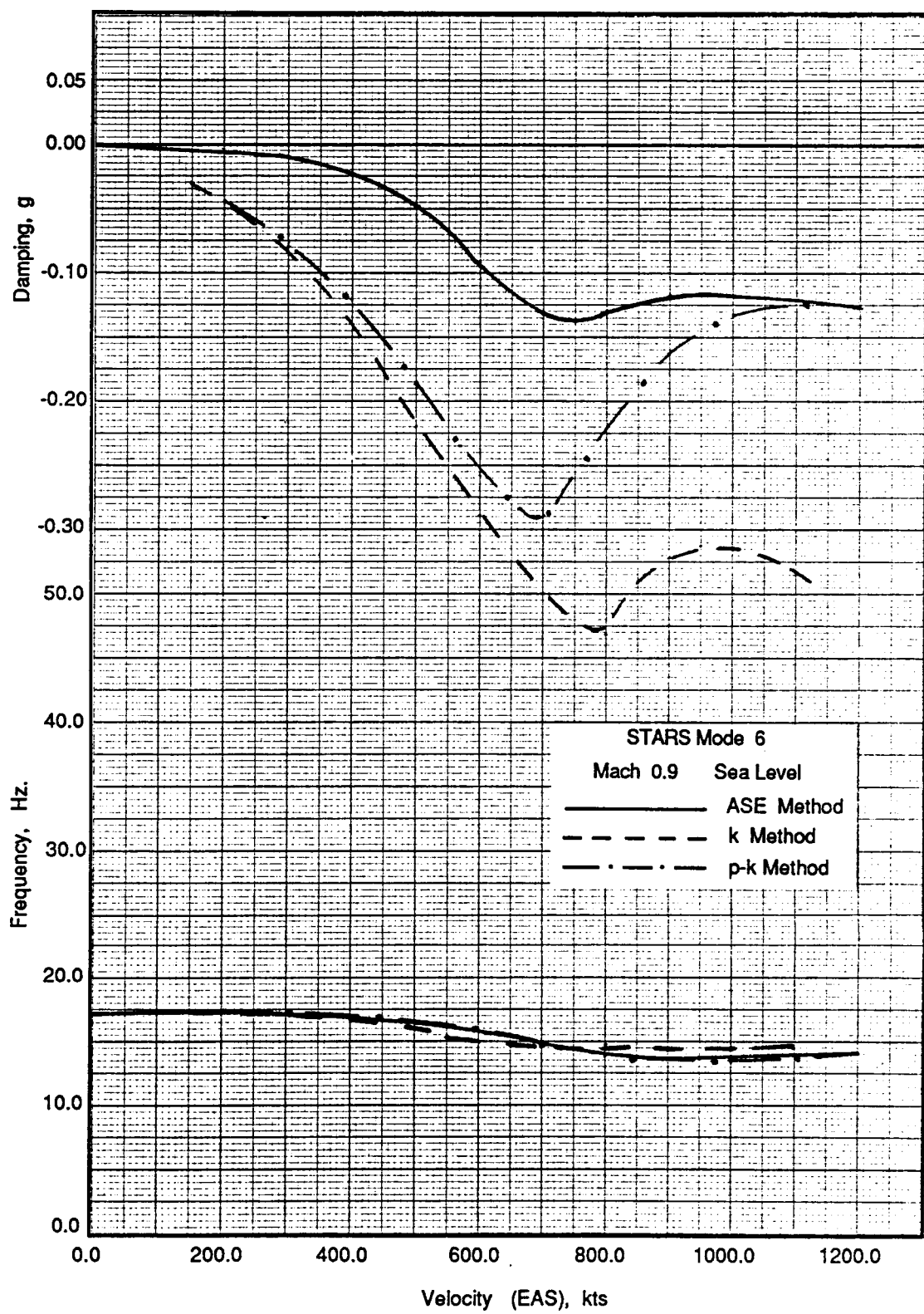


Figure 3.28 Comparative V-g Plot of the Anti-symmetric X29A, Fin 1B Mode

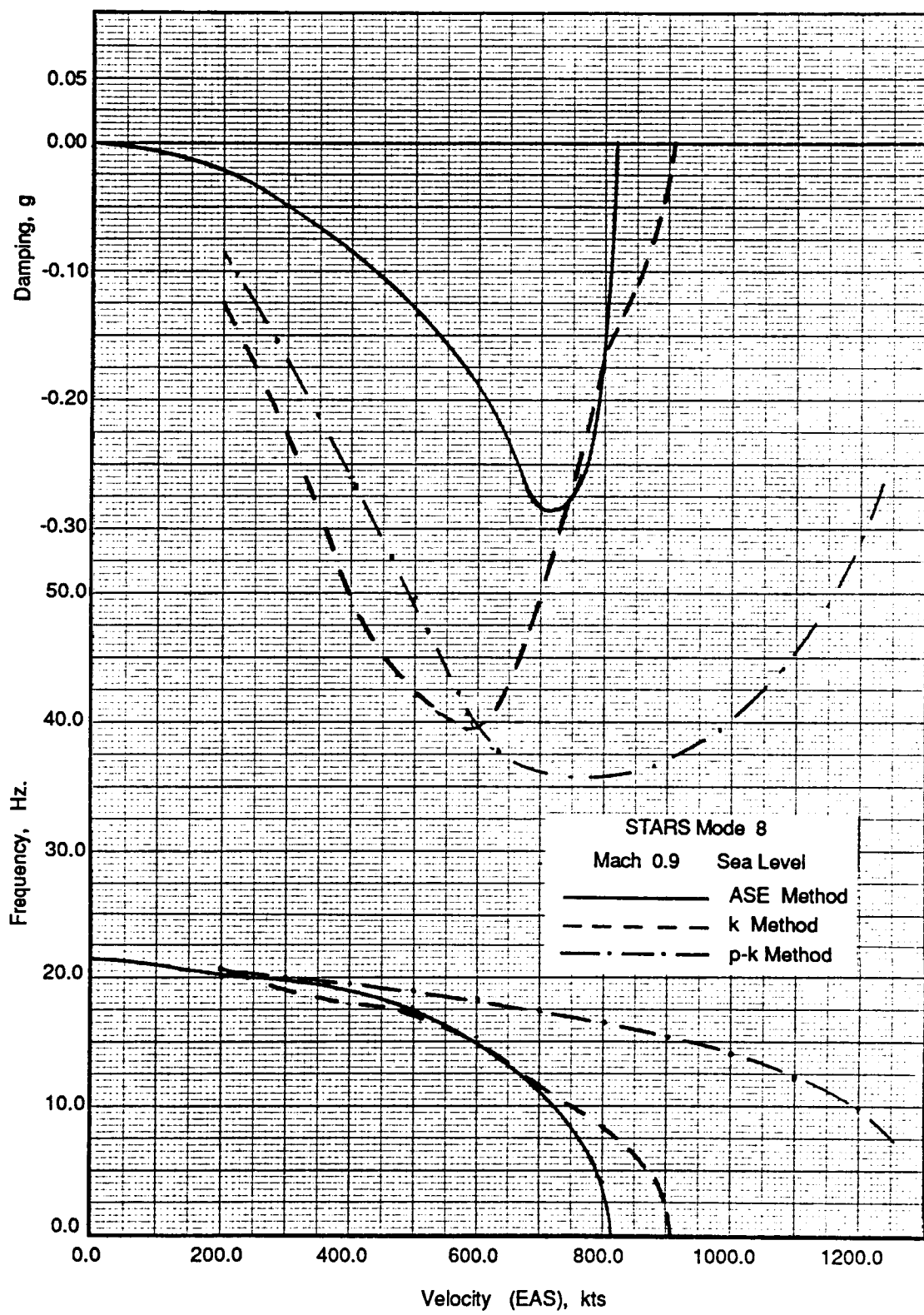


Figure 3.29 Comparative V-g Plot of the Anti-symmetric X29A, CP Mode

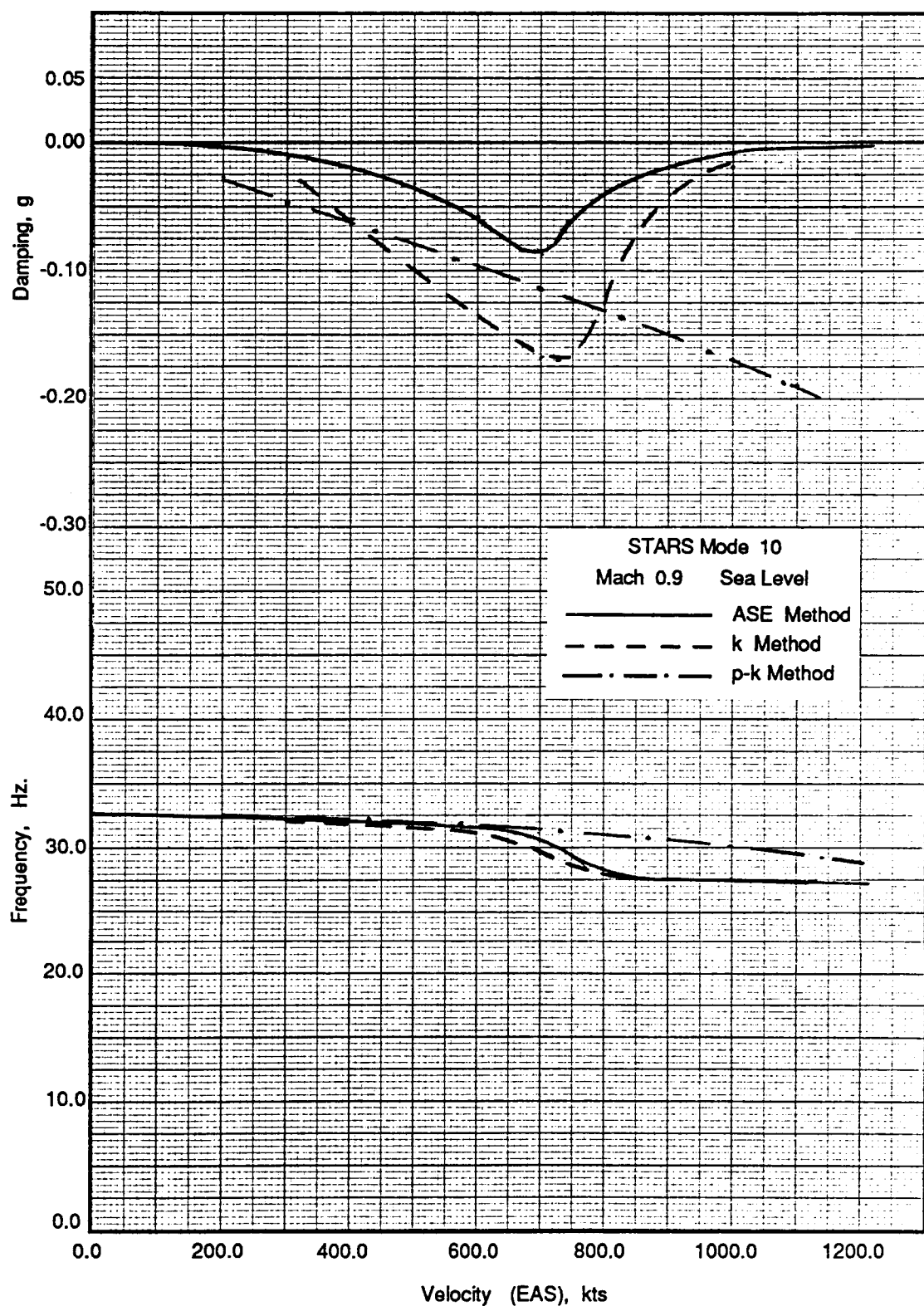


Figure 3.30 Comparative V-g Plot of the Anti-symmetric X29A, W2B Mode

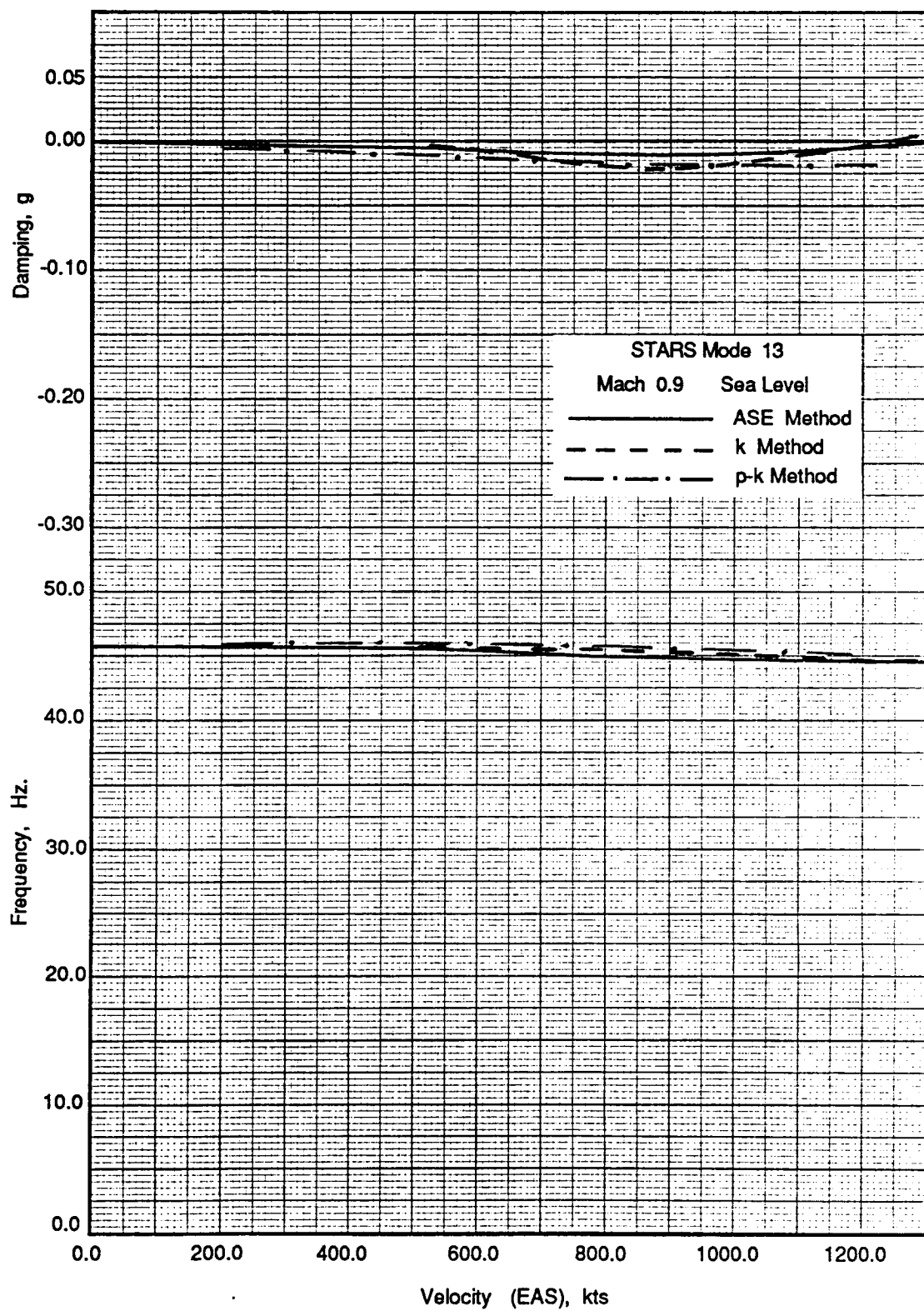


Figure 3.31 Comparative V-g Plot of the Anti-symmetric X29A, W3B Mode

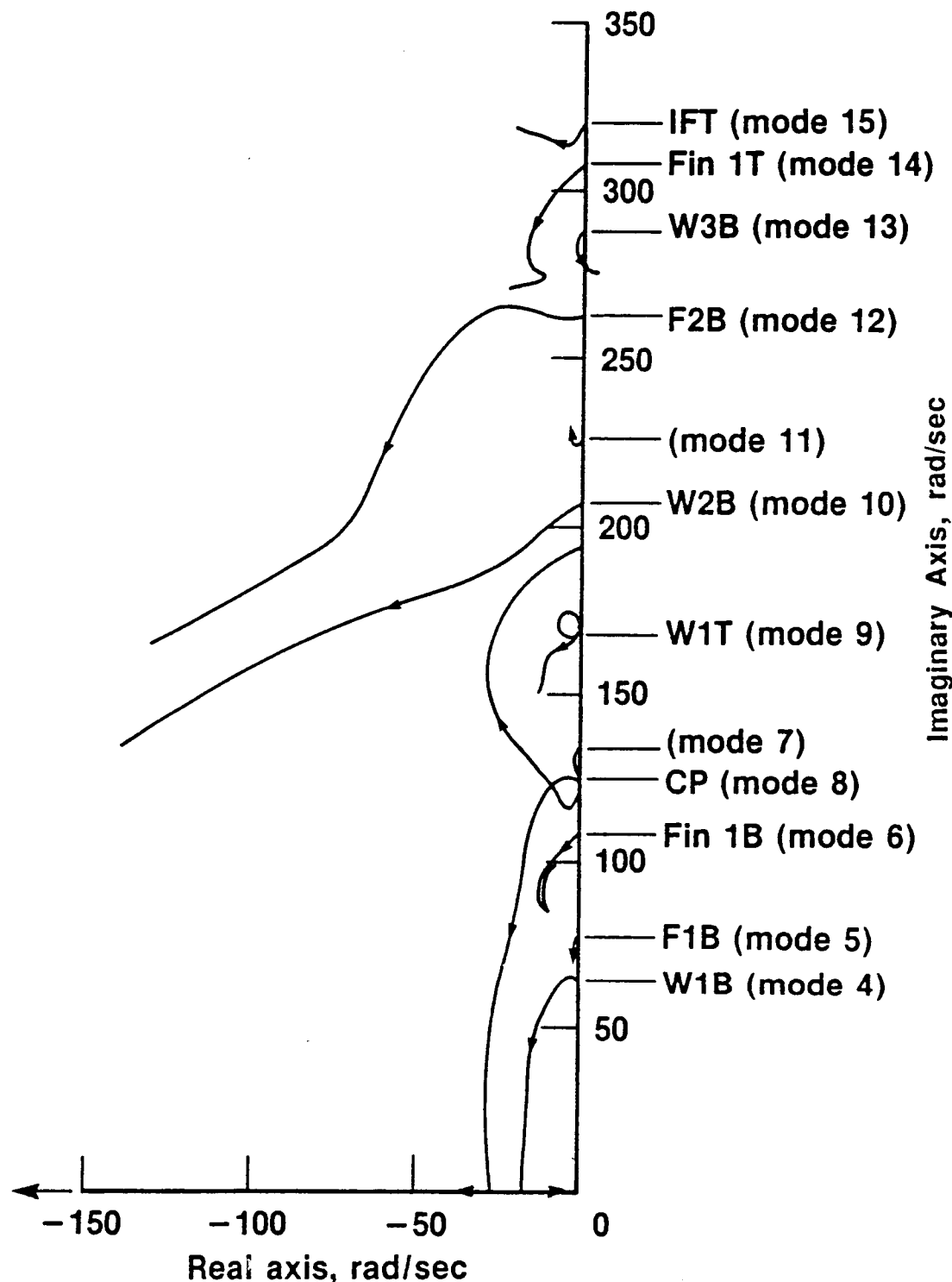


Figure 3.32 Anti-symmetric X-29A Structural Root-Locus,
Elastic Modes -- State-space Method,
Arrows Indicate Increasing Dynamic Pressure

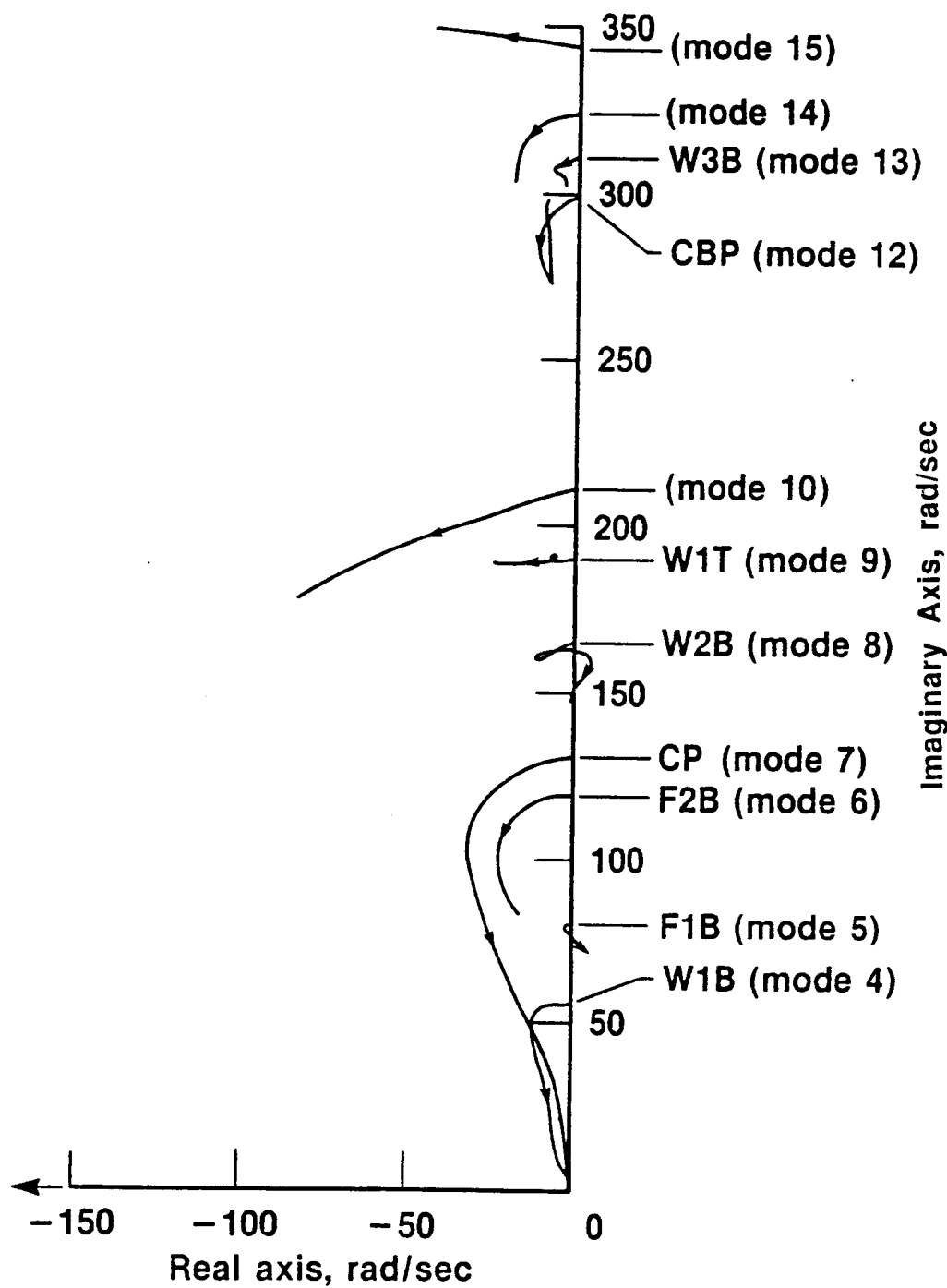


Figure 3.33 Anti-symmetric X-29A Structural Root-Locus,
Elastic Modes -- k Method, Arrows Indicate
Increasing Dynamic Pressure

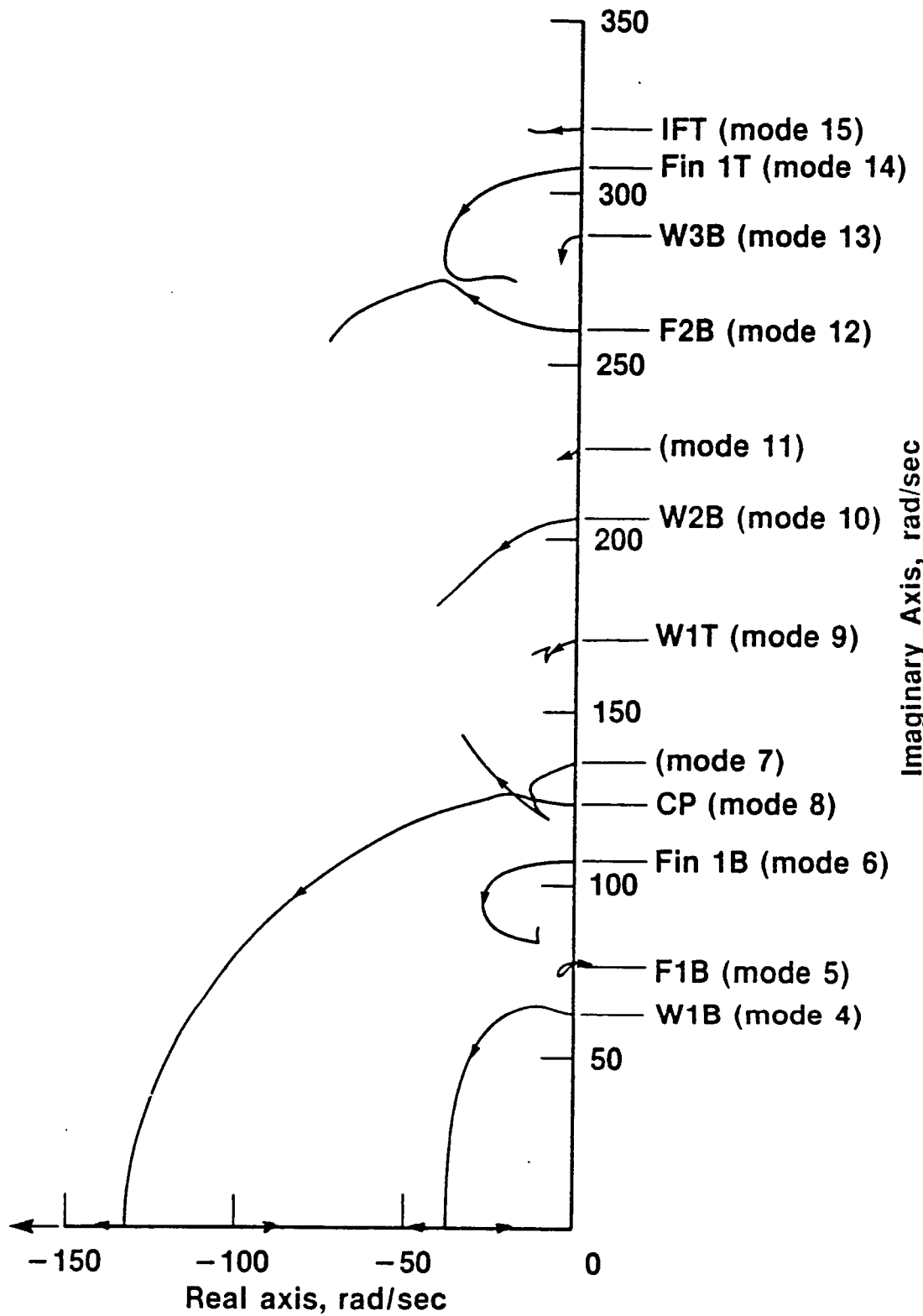


Figure 3.34 Anti-symmetric X-29A Structural Root-Locus,
Elastic Modes -- p-k Method, Arrows Indicate
Increasing Dynamic Pressure

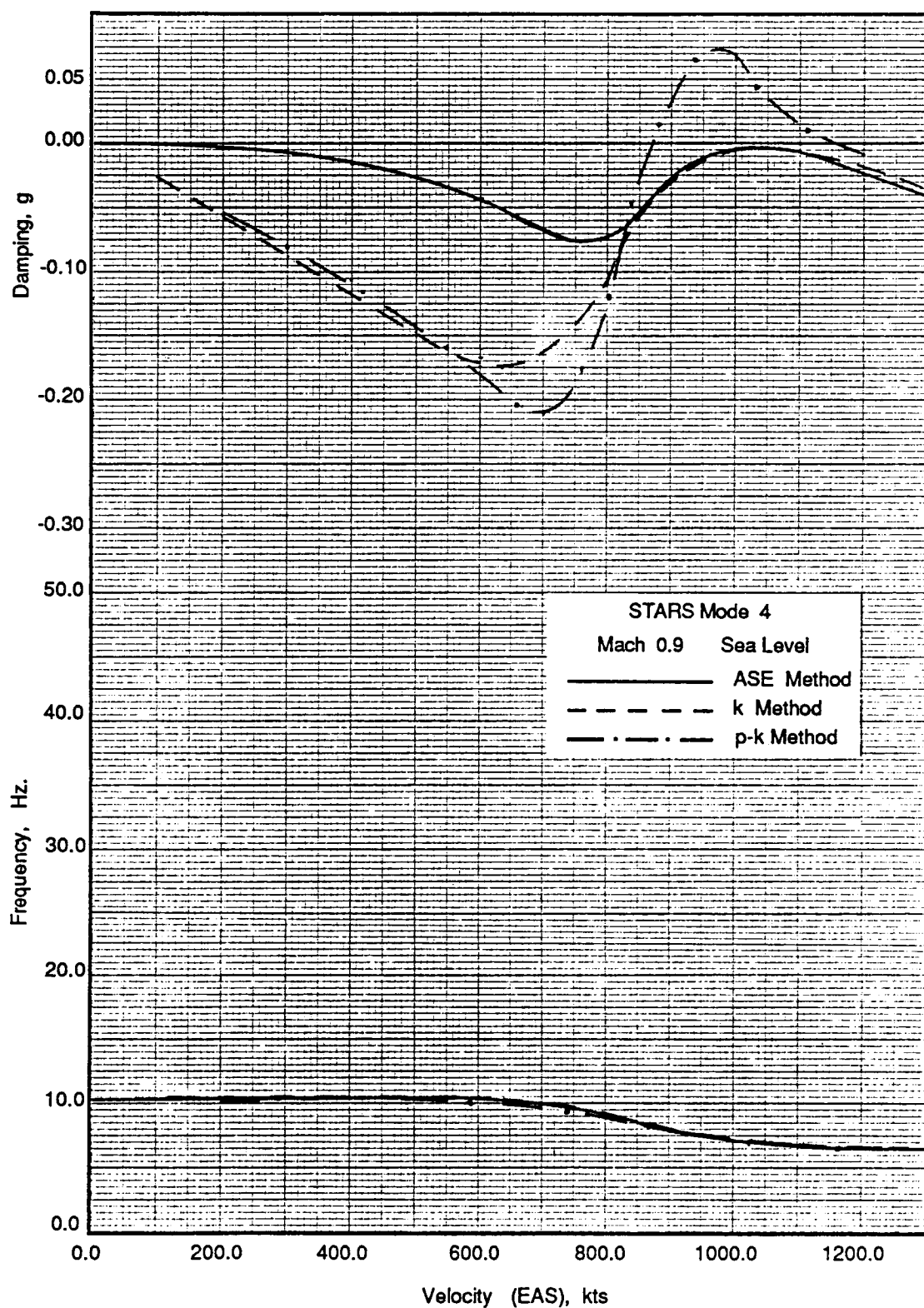


Figure 3.35 Comparative V-g Plot of the Anti-symmetric X29A, W1B Mode (Rigid Body and Flexible Modes)

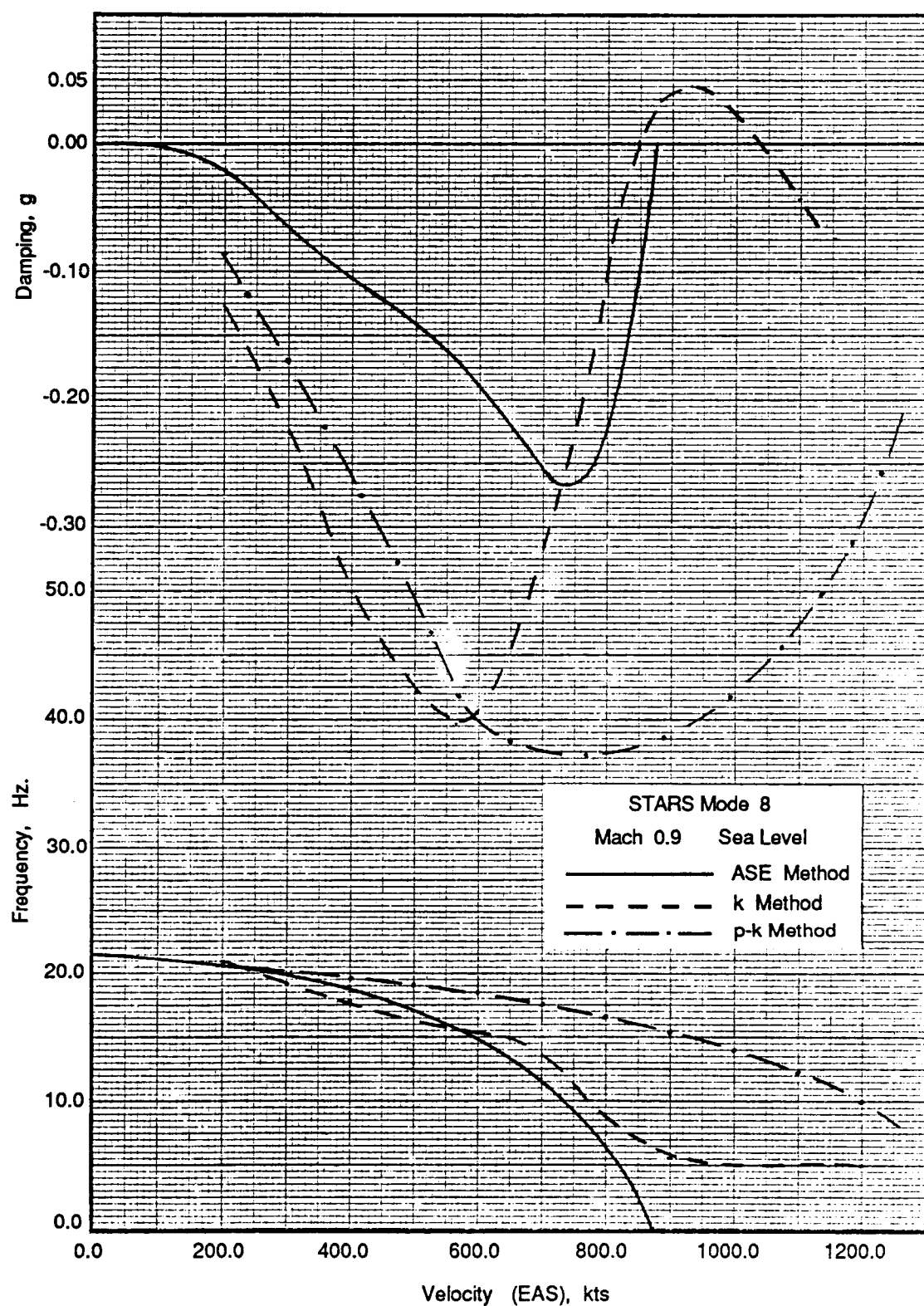


Figure 3.36 Comparative V-g Plot of the Anti-symmetric X29A, CP Mode (Rigid Body and Flexible Modes)

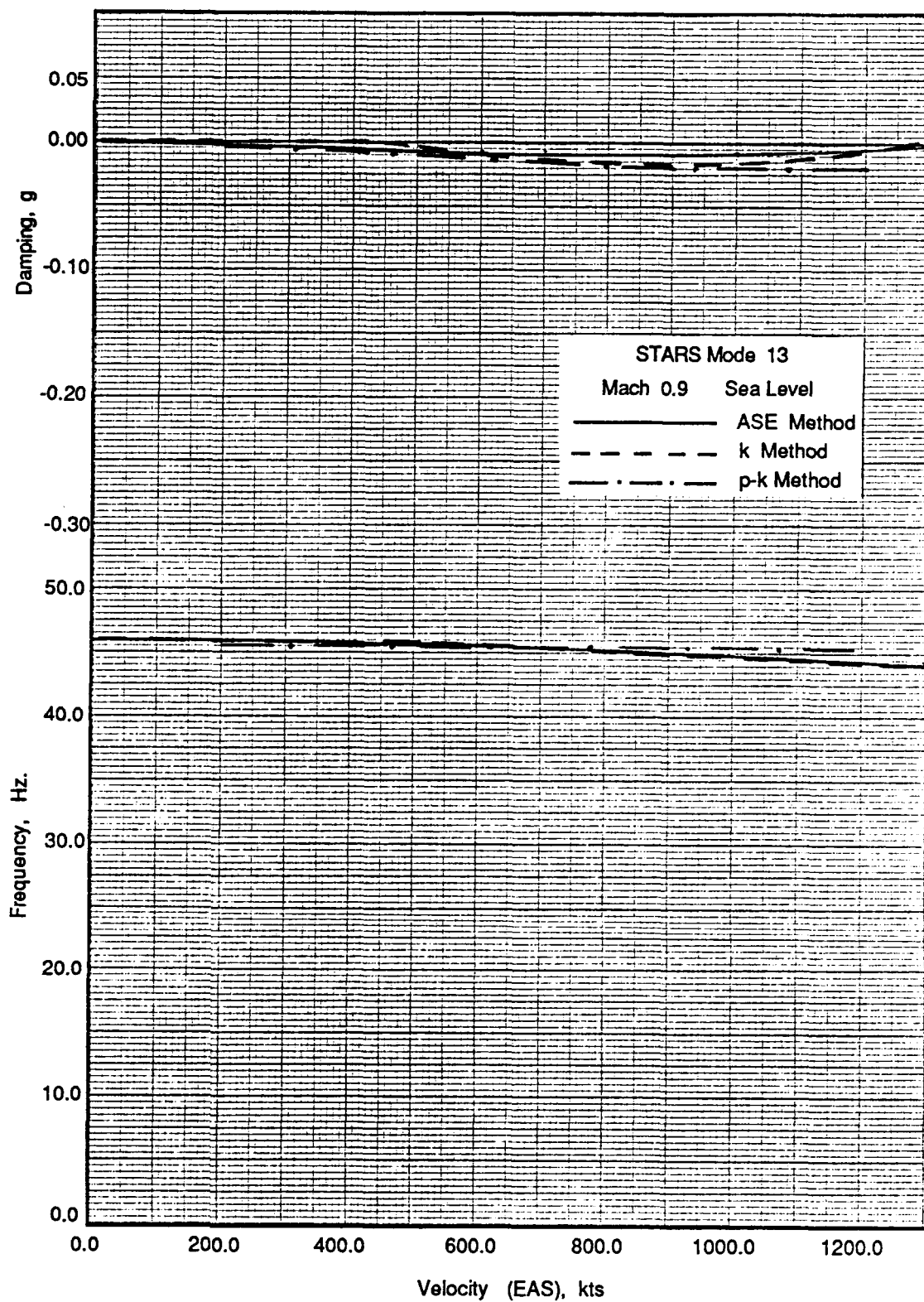


Figure 3.37 Comparative V-g Plot of the Anti-symmetric X29A, W3B Mode (Rigid Body and Flexible Modes)

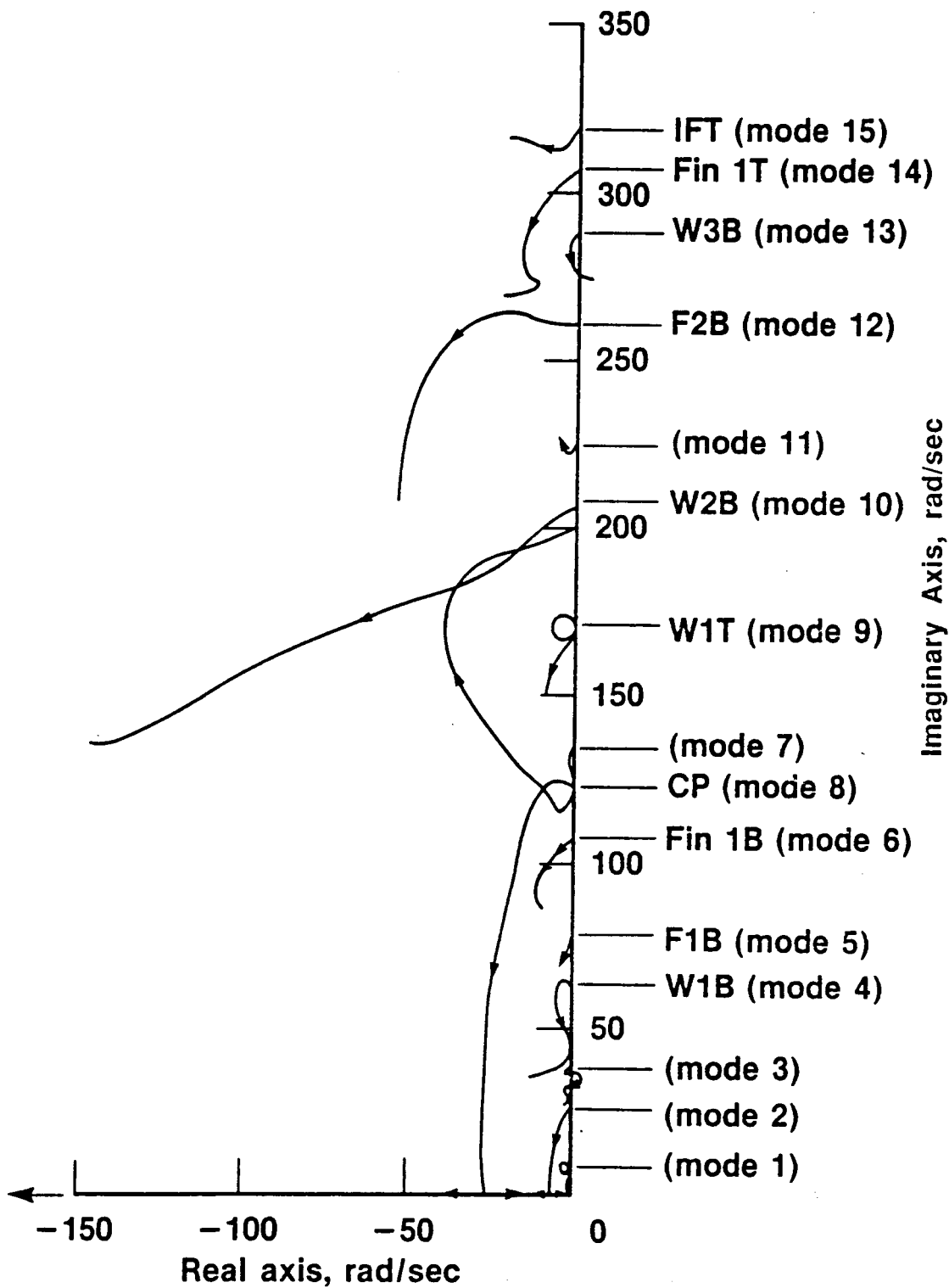


Figure 3.38 Anti-symmetric X-29A Structural Root-Locus Including Rigid Body Modes -- State-space Method, Arrows Indicate Increasing Dynamic Pressure

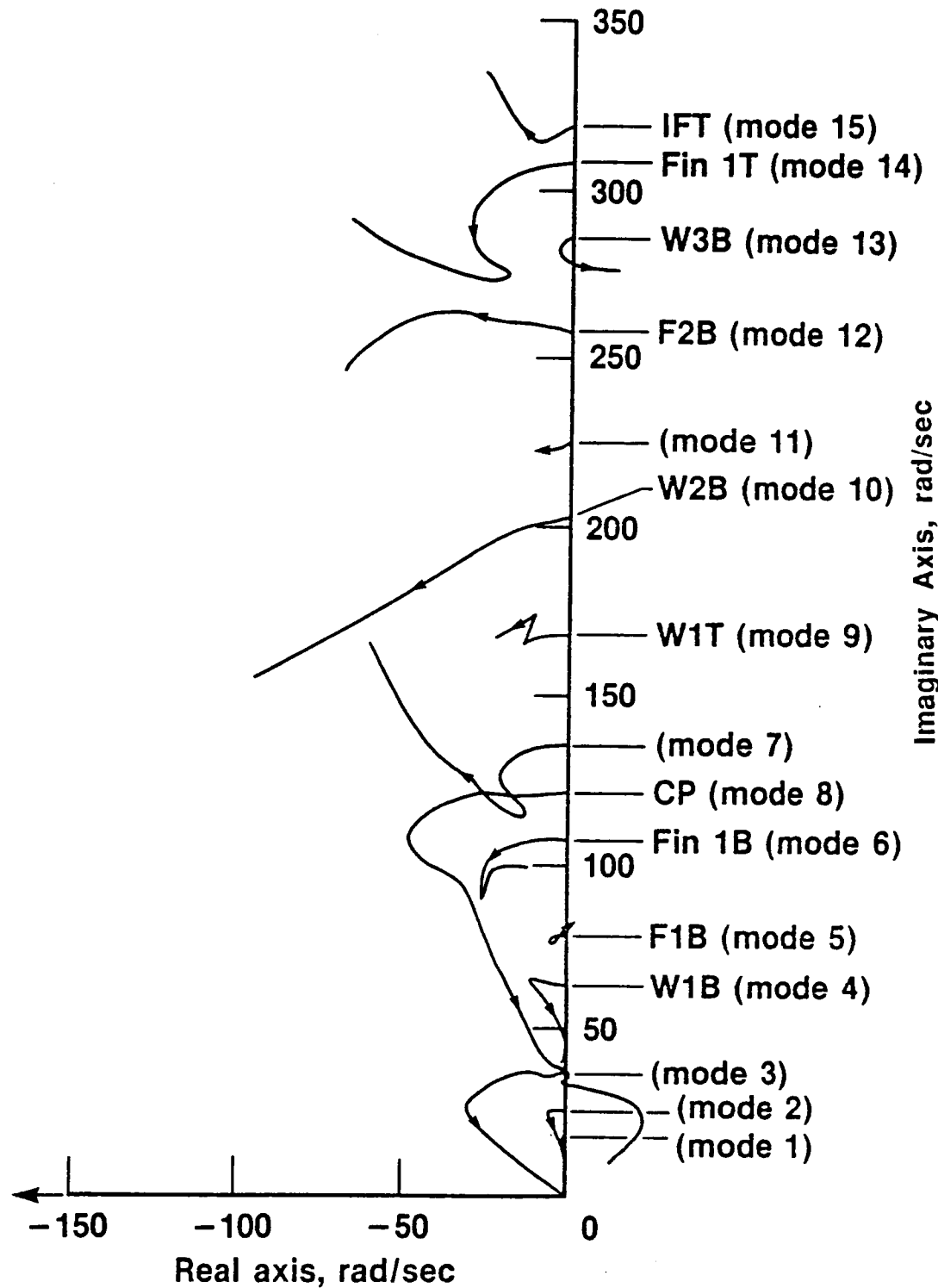


Figure 3.39 Anti-symmetric X-29A Structural Root-Locus Including Rigid Body Modes -- k Method, Arrows Indicate Increasing Dynamic Pressure

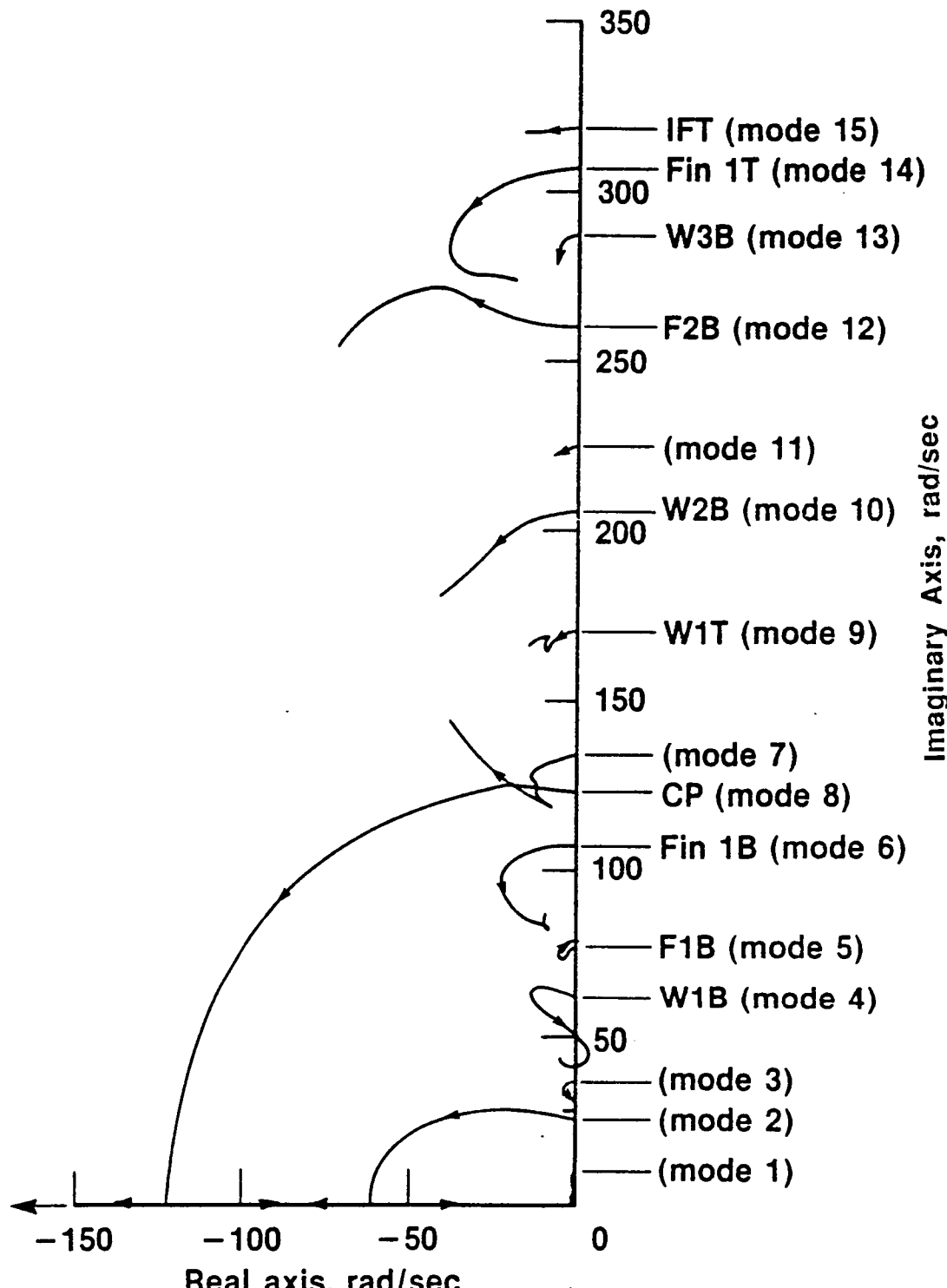


Figure 3.40 Anti-symmetric X-29A Structural Root-Locus Including Rigid Body Modes -- p-k Method, Arrows Indicate Increasing Dynamic Pressure

3.4.3 Conclusions

The theory for three flutter solution techniques (the state-space, k, and p-k methods) performed on the X-29A has been presented. Also presented in Section 3.4 were the results of these three methods. The conclusions about each solution technique are given in this sub-section.

The k-method results for both the symmetric and anti-symmetric cases of the X-29A showed good correlation to the ground vibration survey results. This method assumes that damping and frequency simultaneously approach zero for a divergence instability. The solution of the k-method formulation is relatively quick, and since this method is often used in flutter calculations in the aerospace industry, the results are trusted.

The p-k method results showed good correlation for the symmetric case of the X-29A to the GVS results, while poor correlation was shown for the anti-symmetric case. The anti-symmetric case shows two modes crossing (modes 7 and 8). It is assumed that this crossover causes numerical instabilities for the p-k solution technique. The p-k method uses an iterative solution technique, and thus its solution of the flutter equation is time consuming. The p-k method, though, is believed to show actual damping in the case of divergence, unlike the k-method. The p-k method illustrated non-oscillatory motion before divergence in the W1B and CP modes.

The state-space method has shown good correlation of results to the ground vibration survey results, and to the k and p-k method results. The solution can be obtained efficiently, basically as a side calculation to aeroservoelastic controls analyses. The state-space method showed damping curves similar to the p-k method in the respect that non-oscillatory motion was detected in diverging modes. The damping term, α/β , however, is different than the damping term, g, of the k and p-k methods.

In the anti-symmetric analysis including all the structural modes, the results for all three methods varied significantly to the analysis including only the elastic modes. The differences are assumed to arise from coupling of the rigid body modes to the elastic modes. It was observed, however, that the state-space method was less sensitive to the coupling of the elastic and rigid body modes.

3.5 Aeroservoelastic Controls Analysis

In this section, the interaction between the aeroelastic dynamics and a control system of the X-29A is studied. There are three sub-sections detailing the analyses performed. Sub-section 3.5.1 describes the analyzed X-29A FSW control system. Sub-section 3.5.2 briefly reviews the theory used in obtaining the STARS results. The results of open and closed loop analyses are presented in sub-section 3.5.3. These results indicate rigid body and elastic responses, and are compared with other existing results.

3.5.1 X-29A Flight Control System Description

Due to the unique configuration of the X-29A, a control system design was needed to provide stability, and to ensure safety of the airplane. The relaxed static stability of the X-29A is entirely introduced by the canard control surface, and the wing-body is actually more stable than a typical aft tailed airplane (Ref. 19). Thus, the airplane can be stabilized using existing off-the-shelf actuators and hydraulic systems. To stabilize the airplane, the control system must keep a force from building up on the canard. At subsonic speeds, the canard must retain adequate control power to check any pitching velocity that may develop. At supersonic speeds, the airplane achieves low static stability as seen earlier in Figure 2.4, and therefore retains high maneuverability.

The X-29A flight control system (FCS) is a triple redundant digital fly-by-wire control system, as depicted in Figure 3.41. Each of the three digital computers has an analog backup computer in parallel. The FCS uses seven F-16 Waterlift actuators and two Moog actuators. The F-16 actuators drive the two canards, each with its own actuator, six segmented trailing edge flaperons driven by four actuators, and the rudder (Ref. 8). The Moog actuators drive the two strakes. The all-movable canards on the airplane are the primary aircraft pitch controller, and are augmented by the wing flaperons and strake flaps. Symmetrical deflection of the flaperons also provides variable camber control. Differential deflection of the full-span flaperons provides roll control, and a full-span rudder provides directional control (Ref. 19). The flight control computers, sensors, and the attitude and reference system are mounted in the nose of the airplane. The rate gyros and accelerometers are located aft of the cockpit and in the wheel-well. The pitch gyros are

mounted on the bottom of the airplane keel just forward of the wheel-well for structural isolation. There are two sets of three gyros, a primary set dedicated to the digital computer, and a backup set dedicated to the analog computer, but the latter is also available to the digital computer.

The X-29A FCS has been configured with multiple modes, so in the event of component failure, the system performance degrades to the next level. Normal operation of the X-29A is accomplished via the Normal Digital mode (ND-mode) with the associated option of Automatic Camber Control (ACC). A Normal Power Approach (PA) mode is used for take-off and landing. Two reversion modes have been designed in case of failure of the ND-mode. The Digital Reversion mode (DR-mode) provides digital control with software dissimilar from the ND-mode, and control independent of non-vital sensors. The Analog Reversion mode (AR-mode) provides control in the event of a generic digital control fault. The AR-mode contains a two gain set, Up and Away (UA), and Power Approach (PA) for takeoff and landing. The analyses detailed here were performed using the longitudinal AR-mode, shown in Figure 3.42. In the AR-mode longitudinal system, the stick pitch command activates the deflections of three control surfaces, the canard, flaperon, and strake. The resulting longitudinal pitch rate motion is sensed and fed back to close the loop. Proportional plus integral compensation is provided in the longitudinal AR-mode case, as seen in Figure 3.42.

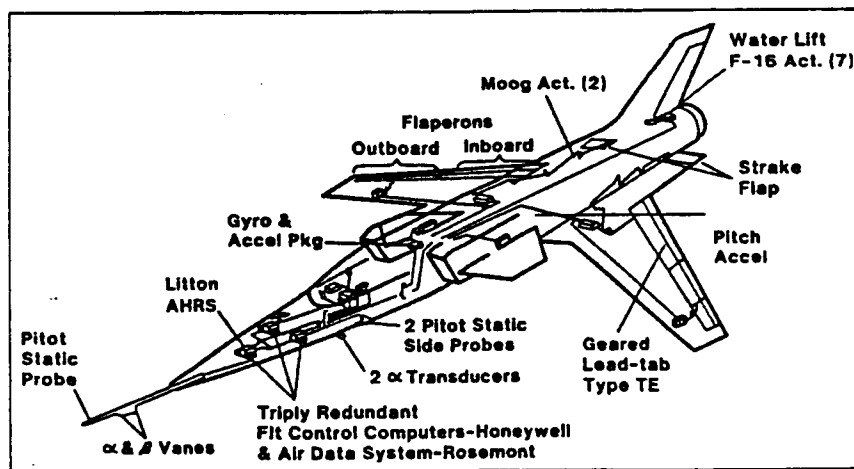


Figure 3.41 X-29A Flight Control System (from Ref. 18)

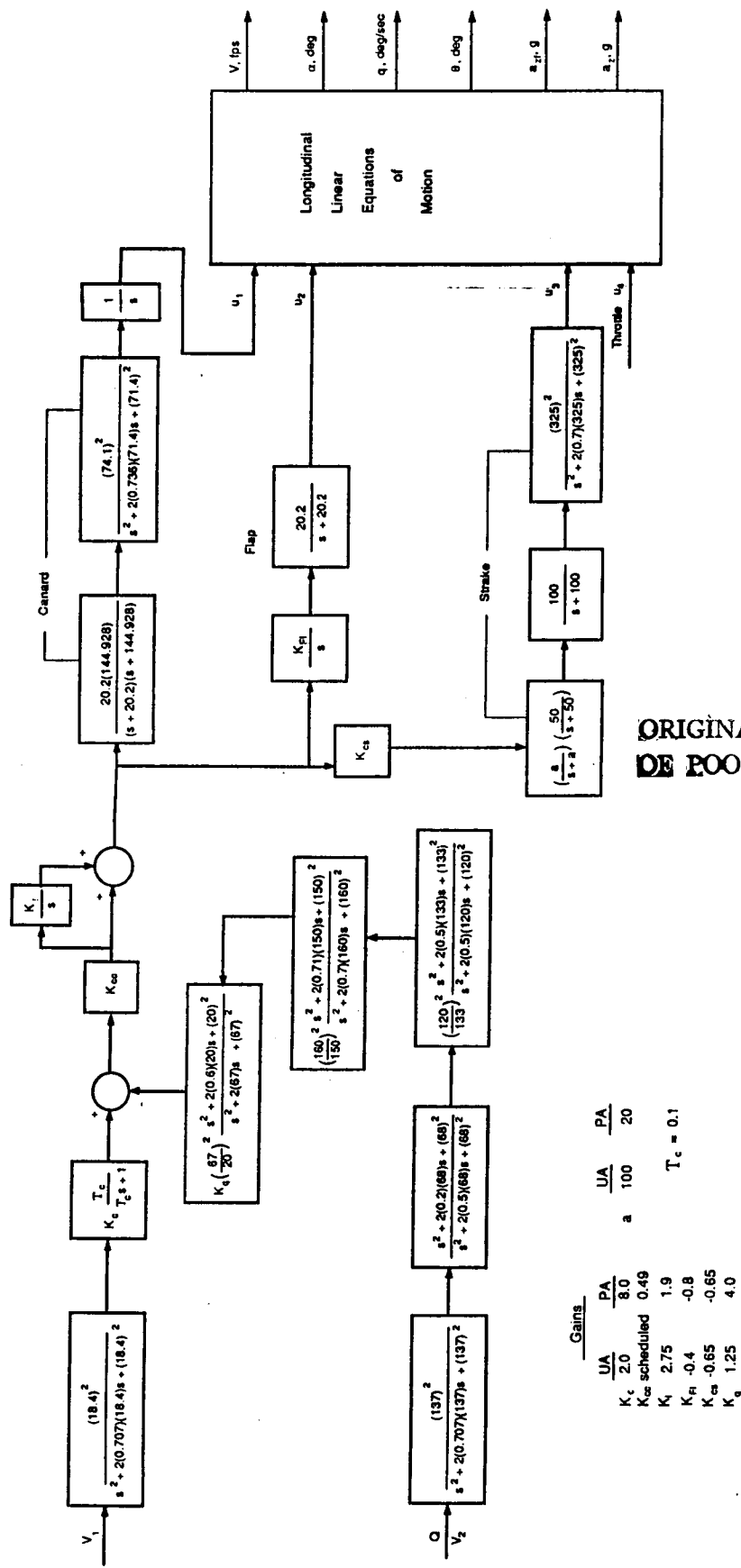


Figure 3.42 Analog Reversion Mode of the Longitudinal FCS, X-29A

3.5.2 Theory of Response Analyses

This sub-section briefly describes the theory used in the open and closed loop analyses performed on the X-29A. Recalling Equation 3.26, the plant dynamics of the aircraft are written in state-space form, transformed from earth-fixed coordinates to body-fixed coordinates, shown below.

$$\dot{\mathbf{X}} = \mathbf{AX} + \mathbf{Bu} \quad (3.26a)$$

In the above equation, \mathbf{A} represents the plant dynamics matrix, and \mathbf{B} represents the control surface influence matrix. A sensor interpolation matrix is developed next, deriving displacement, velocity, and acceleration from the structural data. When applied to Equation 3.26a, the output, \mathbf{y} , is related as shown in Equation 3.29.

$$\mathbf{y} = \mathbf{CX} + \mathbf{Du} \quad (3.29a)$$

where

$$\mathbf{C} = \mathbf{T}_s \phi \mathbf{A} \quad (3.29b)$$

and

$$\mathbf{D} = \mathbf{T}_s \phi \mathbf{B} \quad (3.29c)$$

In the above Equation, \mathbf{C} and \mathbf{D} are matrices signifying output at the sensors due to the body and control surface motions, respectively. Figure 3.43 shows a simplified block diagram for an aircraft with a feedback control system. The open loop transfer function, $H(s)$, can be derived by applying a Laplace transformation to the state-space equations, (Equations 3.26a and 3.29a). The result is shown below.

$$\mathbf{y}(s) = H(s)\mathbf{u}(s) \quad (3.30)$$

where

$$H(s) = \mathbf{C}[sI - \mathbf{A}]^{-1}\mathbf{B} + \mathbf{D} \quad (3.31)$$

The closed loop transfer function, $\hat{H}(s)$, with a controller gain $G(s)$, is derived from the relations in Equations 3.32 and 3.33.

$$y(s) = \hat{H}(s)r(s) \quad (3.32)$$

where

$$\hat{H}(s) = H(s)[I + G(s)H(s)]^{-1} \quad (3.33)$$

In Equation 3.32, $r(s)$ is the reference input. The matrix inversion involved in Equation 3.31 for each value of s could be quite laborious. However, in the solution technique used here, this problem is avoided by first solving the eigenvalue problem for the matrix A (see Equation 3.27), then a coordinate transformation is applied, resulting in the open loop transfer function shown below.

$$H(s) = C\psi(sI - \lambda)^{-1}\psi^{-1}B + D \quad (3.34)$$

where λ and ψ are the eigenvalue and eigenvector matrices, respectively, of A . Note that the term $(sI - \lambda)$ is a diagonal matrix, and thus its inversion is trivial. Therefore, the calculation of $H(s)$ using Equation 3.34 is a much simpler task. With the formulation of the transfer functions, the phase and gain may be calculated and plotted as functions of frequency using typical Bode plots. Such results follow.

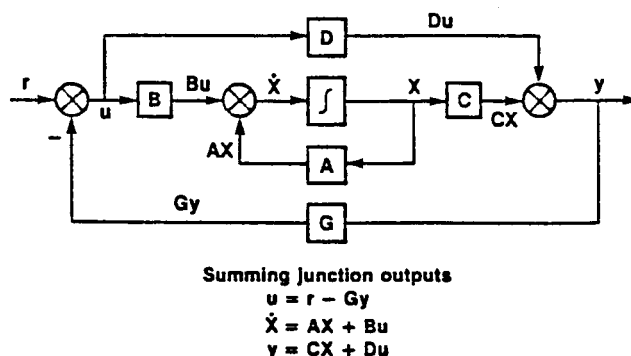


Figure 3.43 Simplified Aircraft Feedback Control System

3.5.3 X-29A Open and Closed Loop Results

The results of the ASE control analysis performed on the symmetric X-29A are presented in this sub-section. In the ASE analysis, the longitudinal analog control laws of the AR-mode are augmented with the plant to compute frequency responses. The plant consists of the rigid body states, elastic structural modes, and two unsteady aerodynamic lag states. The sensed measurements include rigid body and flexible effects. This analysis compares STARS results for plants including rigid body modes and for rigid and elastic modes to Grumman Aerospace Corporation results for both the open and closed loop.

The criteria for the dynamic stability of the X-29A augmented with the airframe was based on MIL-F-9490 (Ref 19). This specification (Ref. 20), when applied to a conditionally stable closed loop system, as on the X-29A, requires gain and phase margins of ± 6 dB and 45 deg, respectively, for all system modes with frequencies below the first structural mode. These requirements, however, were reduced by a factor of two since, among other reasons, the X-29A is not a production airplane, and the flight control system component tolerances are very tight and are extensively checked before and after each flight. Also, per MIL-A-008870A (Ref. 21), the open loop augmented aircraft frequency response curves should not have any gain crossovers at airframe resonances, and a gain margin of at least 6 dB is required. This provision required the design and implementation of notch filters in the flight control system.

The Grumman Aerospace Corporation (GAC) results were determined from their in-house analysis program, SAEL (ServoAeroELasticity) as described in Reference 22. The GAC SAEL results include analytical unsteady aerodynamics based on the ground vibration survey mode shapes, augmented with wind tunnel steady aerodynamics. The STARS open and closed loop results include the analytical unsteady aerodynamics (based on STARS analytical mode shapes) referenced to the controller, and augmented with wind tunnel based steady aerodynamics. Figures 3.44 through 3.48 compare various open loop frequency responses for STARS rigid body and elastic modes to SAEL elastic results. The AR-mode (with q feedback) open loop input and output is indicated on Figure 3.42. Closed loop comparisons of q and n_z feedback are shown in Figures 3.49 through 3.53. Both the open and closed loop results investigate the effectiveness of the structural notch filters by running analyses including and omitting the filters.

Figure 3.44 shows the phase and gain plots for the STARS rigid body open loop analysis including the notch filters. Below the first elastic structural mode (W1B) of 56.3 rad, these plots show gain margins (GM) of -5.85 at 1.43 rad and 4.06 dB at 30.3 rad. The phase margin of 34.95 deg occurs at 13.9 rad. All meet the stability requirements mentioned earlier. Figure 3.45 shows phase and gain plots for the STARS flexible AR-mode open loop, with notch filters. The response is similar to the rigid body open loop, however the flexible effects of the structure are shown at about 160 rad. These plots show gain margins of -3.84 dB at 4.71 rad, and 5.93 dB at 30.53 rad. A PM of 27.3 deg occurs at 10.8 rad. Figure 3.46 shows the phase and gain plots for GAC SAEL results of the flexible AR-mode open loop with notch filters. The SAEL results show gain margins of -4.3 dB at 3.5 rad and 6.4 dB at 29.5 rad. A PM of 35.7 deg occurs at 10.9 rad. Comparing the STARS and SAEL flexible results, relatively good correlation is shown for the phase and gain plots, however, the elastic structural effects vary somewhat. Specifically, the SAEL results indicate greater response at the structure's natural frequencies. This difference could be attributed to the fact that the SAEL results use the ground vibration survey in their calculations, while the STARS results are completely analytical.

Figures 3.47 and 3.48 show the phase and gain frequency responses for the STARS and SAEL AR-mode open loop without the structural notch filters. The STARS results show gain margins of -4.2 dB at 4.3 rad and 6.1 dB at 47.5 rad. The SAEL results show gain margins of -5.7 dB at 2.9 rad and 7.6 dB at 42.7 rad. The STARS analysis shows a PM of 43.0 deg at 11.1 rad, while the SAEL analysis shows a PM of 51.7 deg at 11.5 rad. Thus, the curves show relatively good correlation concerning the phase and gain margins. However, the flexible effects shown in the two analyses vary significantly. The STARS analysis does not indicate any instabilities, i.e., no gain crossovers are exhibited while the SAEL results show two instabilities occurring. The SAEL results show instabilities at approximately 71 rad and 126 rad. These frequencies correspond to the fuselage first bending (F1B) mode and to the noseboom (NB) mode. The differences in the response plots, again, can be explained since the SAEL analyses used the GVS mode shapes, while the STARS analyses were based on its analytical eigenvalues and eigenvectors. The second difference is attributed to the STARS FEM. Since the X-29A FEM did not include the noseboom, this mode was not present in the STARS analysis. Currently, efforts are being made to include the noseboom into the STARS finite element model, thus allowing

comparisons to be made at a later date. The response curves from the closed loop ASE controls analyses performed on the longitudinal X-29A are described below.

The primary purpose of the closed loop analyses is to determine if any adverse airframe/control coupling occurs. For instance, ASE instabilities involving flexible modes may exist for a particular feedback FCS design. These analyses, with notch filters included, would confirm filter effectiveness in suppressing the instability without degrading the rigid body phase and gain margins. Figures 3.49 and 3.50 compare STARS rigid body and flexible closed loop response analyses with n_z feedback and notch filters. Good correlation is shown between the rigid body and flexible phase and gain response plots. The rigid body has a phase crossover at 23.2 rad with a GM of -14.1, while the flexible analysis shows a phase crossover at 23.8 rad with a GM of -13.5 dB. The respective PM are 59 deg and 50 deg occurring at gain crossovers of 33.5 rad and 32 rad. Figures 3.51 through 3.53 show the comparative closed loop plots without notch filters from the stick input with q feedback. Figures 3.51 and 3.52 show the STARS rigid body closed loop and the STARS flexible closed loop phase and gain response plots. Figure 3.53 shows the SAEL flexible closed loop phase and gain response plots. All three show good correlation, however, the SAEL phase and gain plots show more response at the natural frequencies.

The extensive flight testing of the X-29A has given many valuable results, and some of these have been compared to the STARS analytical results. Good correlation has been shown between the STARS closed loop damping and frequency and flight test closed loop damping and frequency results, however, due to security requirements, this information may not be shown.

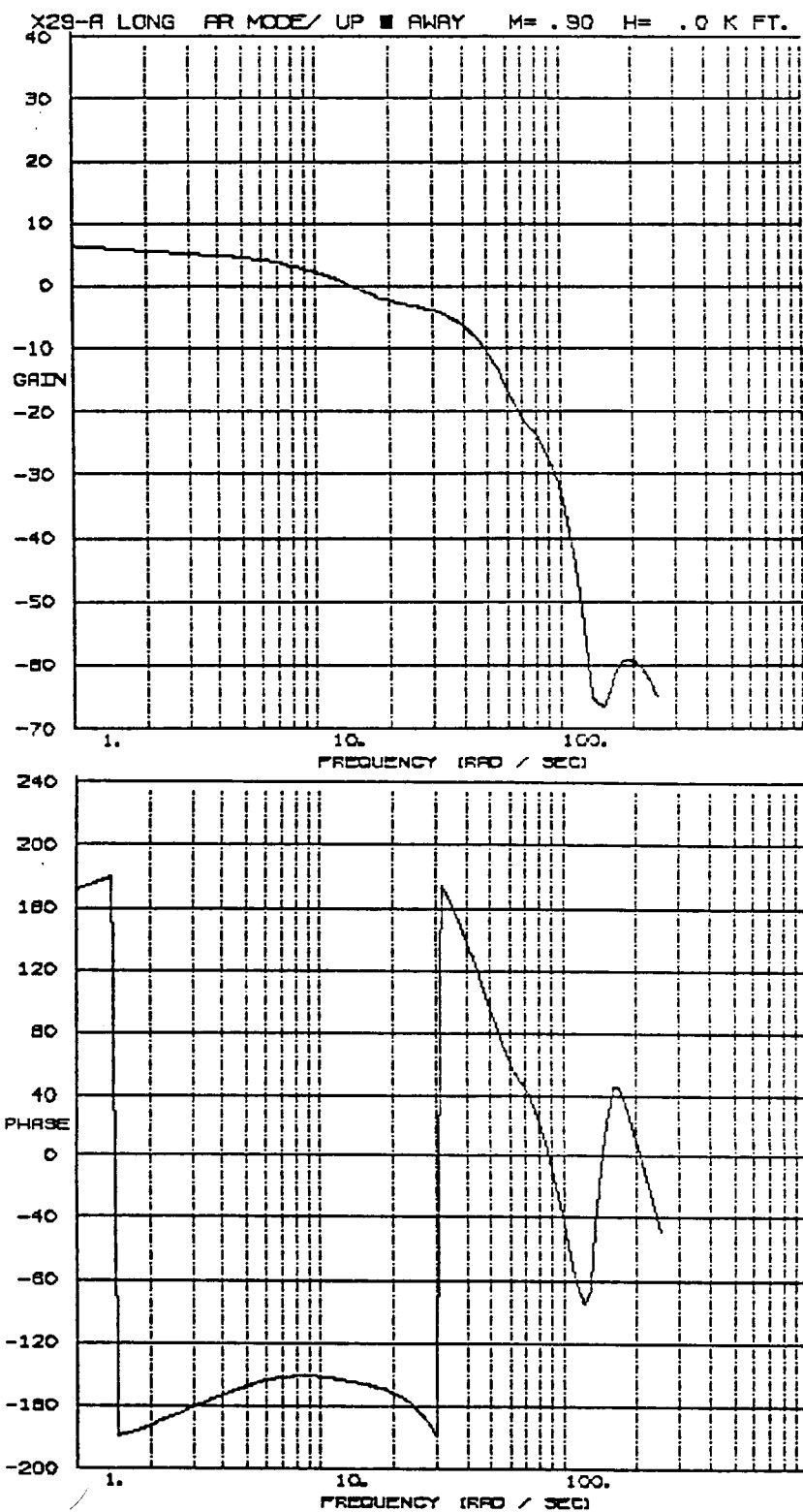


Figure 3.44 STARS Open Loop Frequency Response of the Symmetric X-29A using Analytical Rigid Body Modes

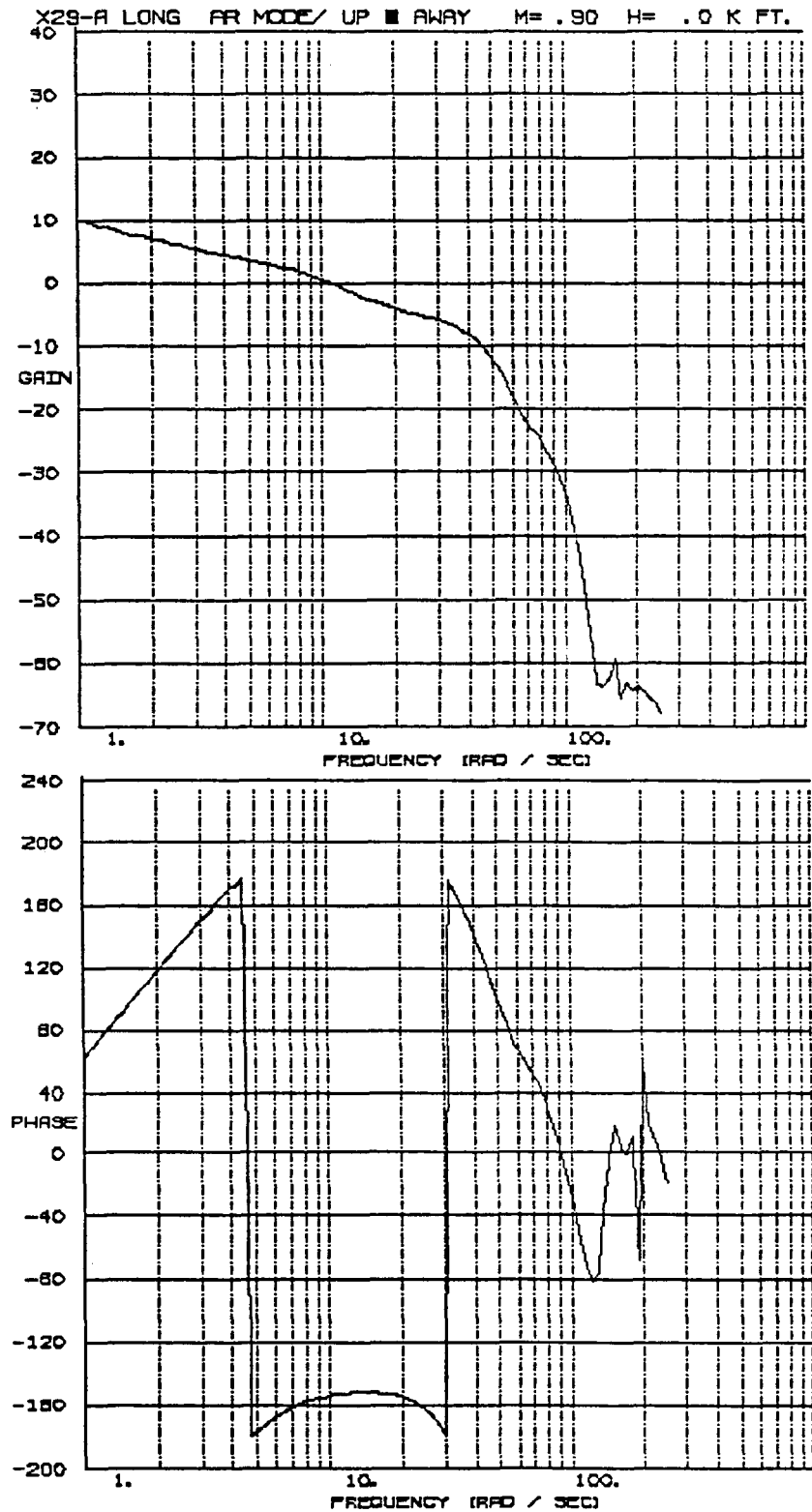


Figure 3.45 STARS Open Loop Frequency Response of the Symmetric X-29A using Analytical Flexible Modes

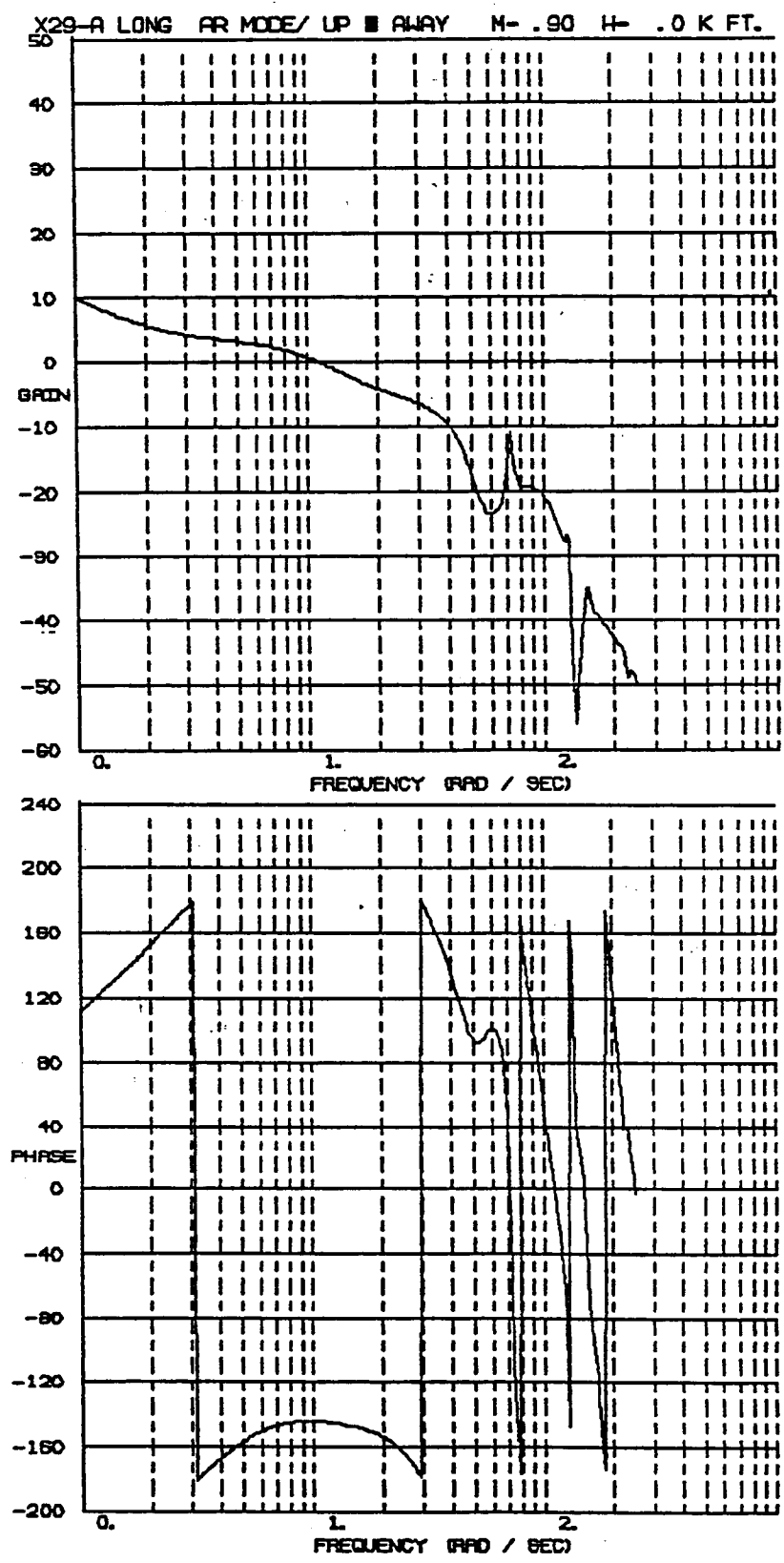


Figure 3.46 SAEI Open Loop Frequency Response of the Symmetric X-29A using GVS Flexible Modes

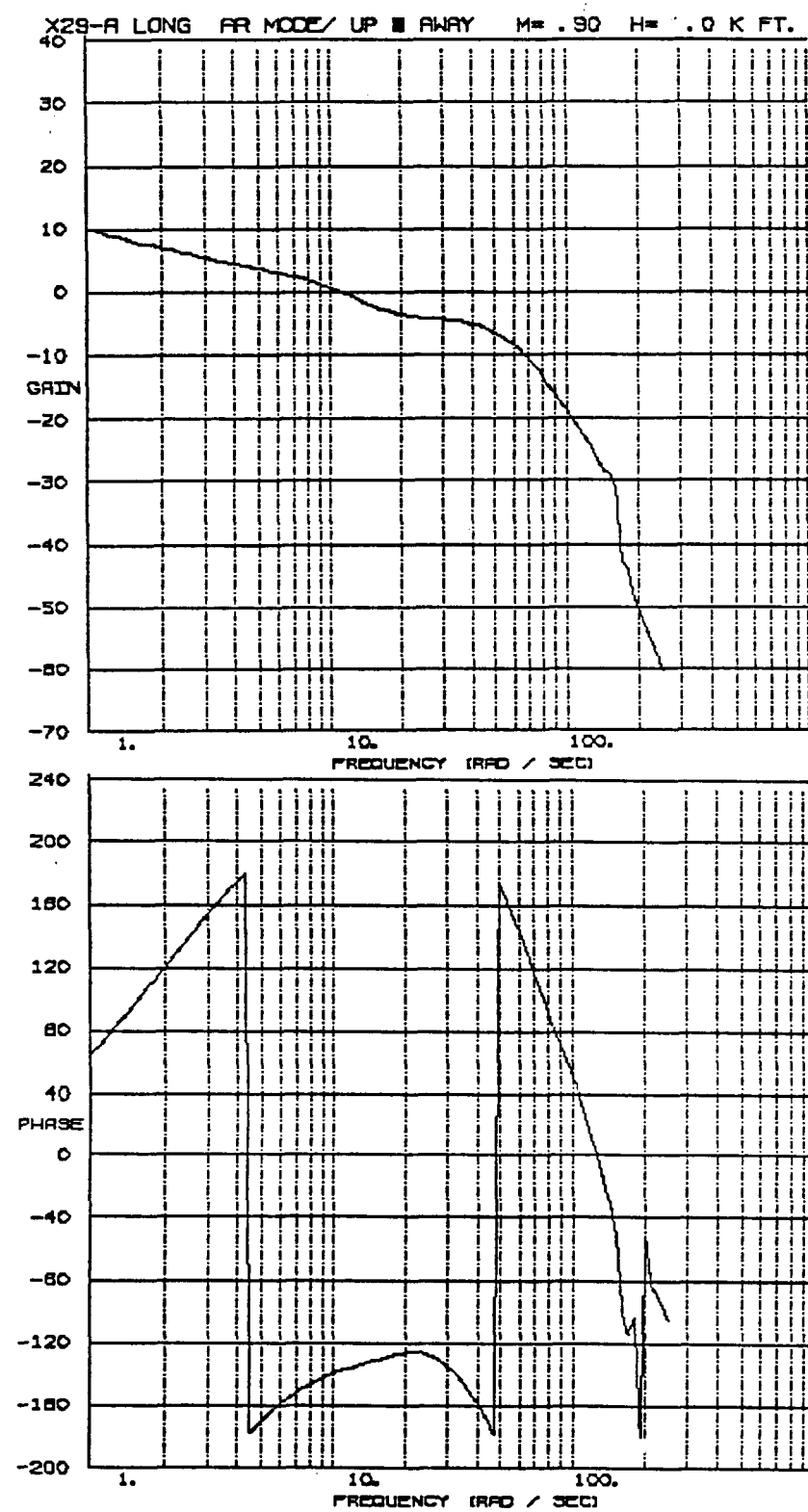


Figure 3.47 STARS Open Loop Frequency Response of the Symmetric X-29A using Analytical Flexible Modes, Excluding Notch Filters

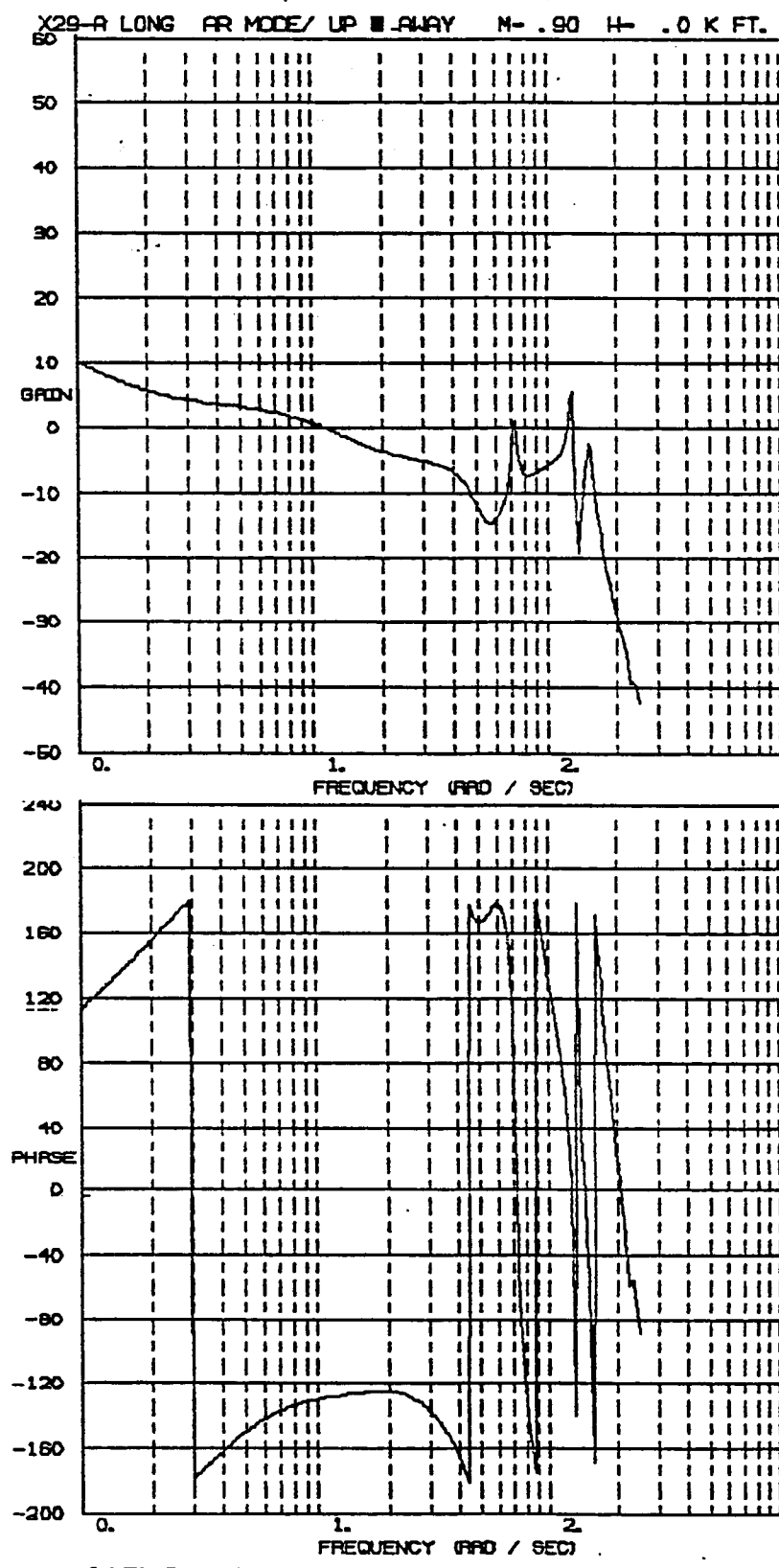


Figure 3.48 SAEI Open Loop Frequency Response of the Symmetric X-29A using GVS Flexible Modes, Excluding Notch Filters

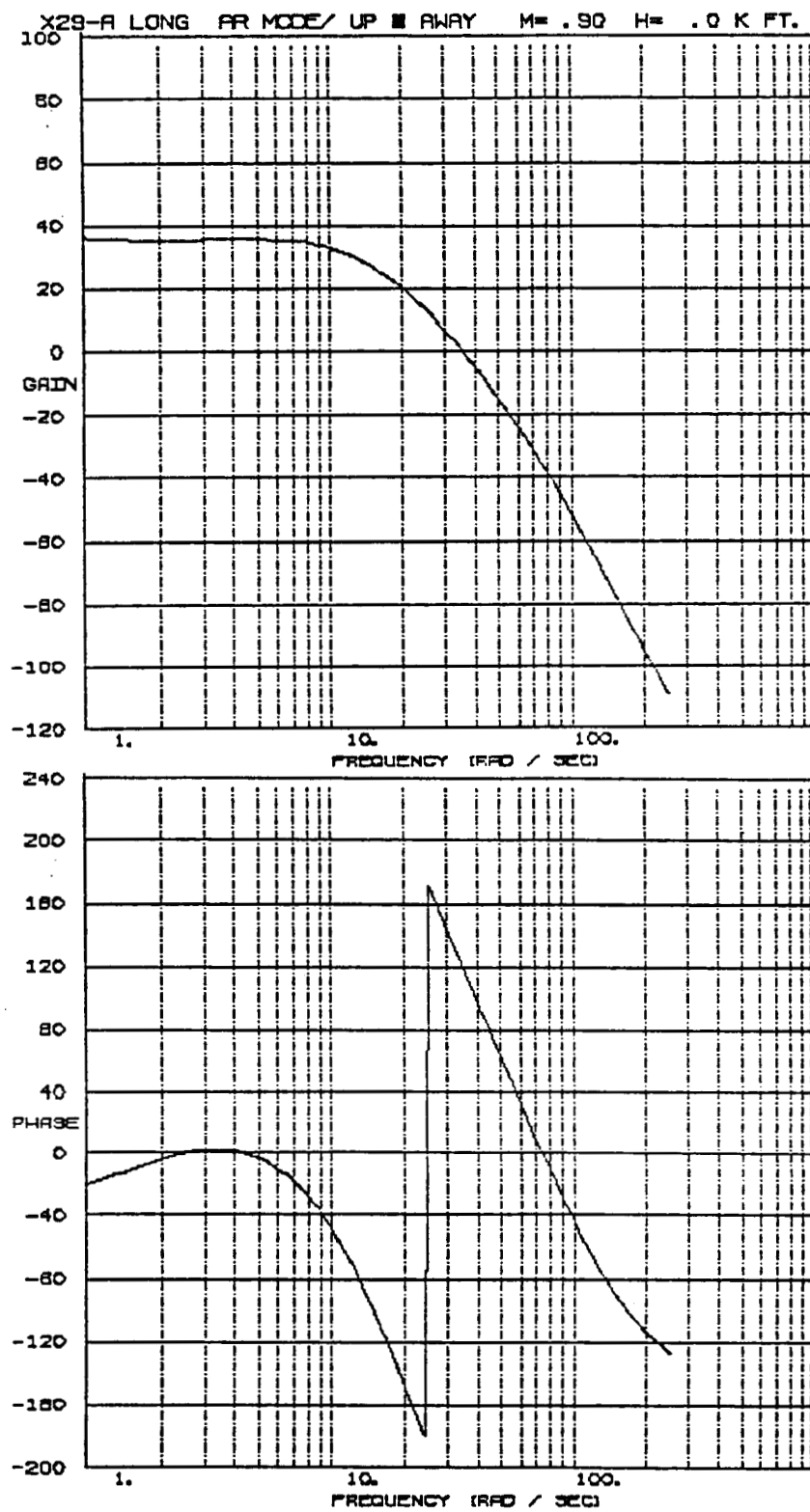


Figure 3.49 STARS Closed Loop Frequency Response for the Symmetric X-29A using Analytical Rigid Body Modes from Stick Position to Sensed Normal Force

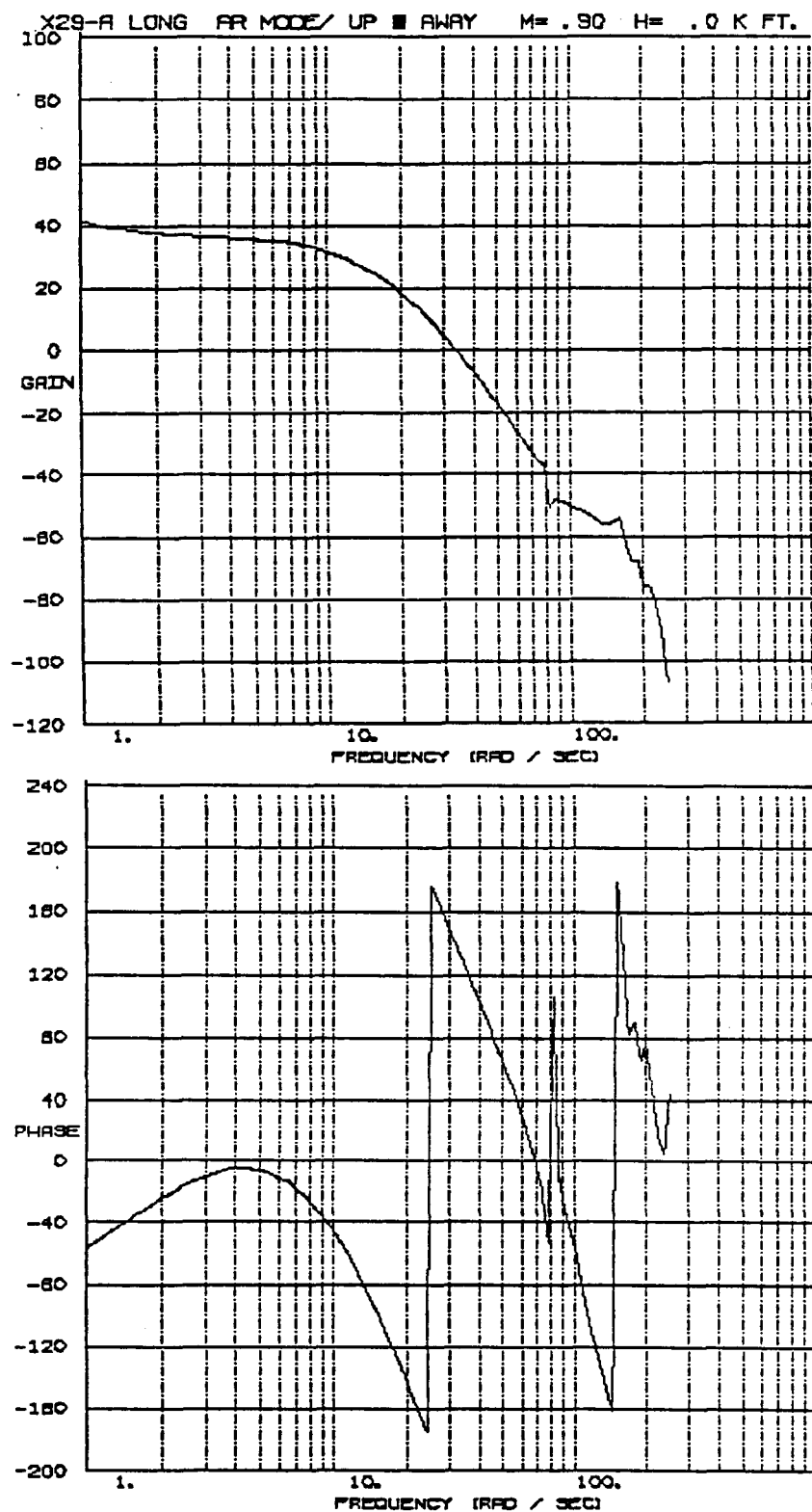


Figure 3.50 STARS Closed Loop Frequency Response for the Symmetric X-29A using Analytical Flexible Modes from Stick Position to Sensed Normal Force

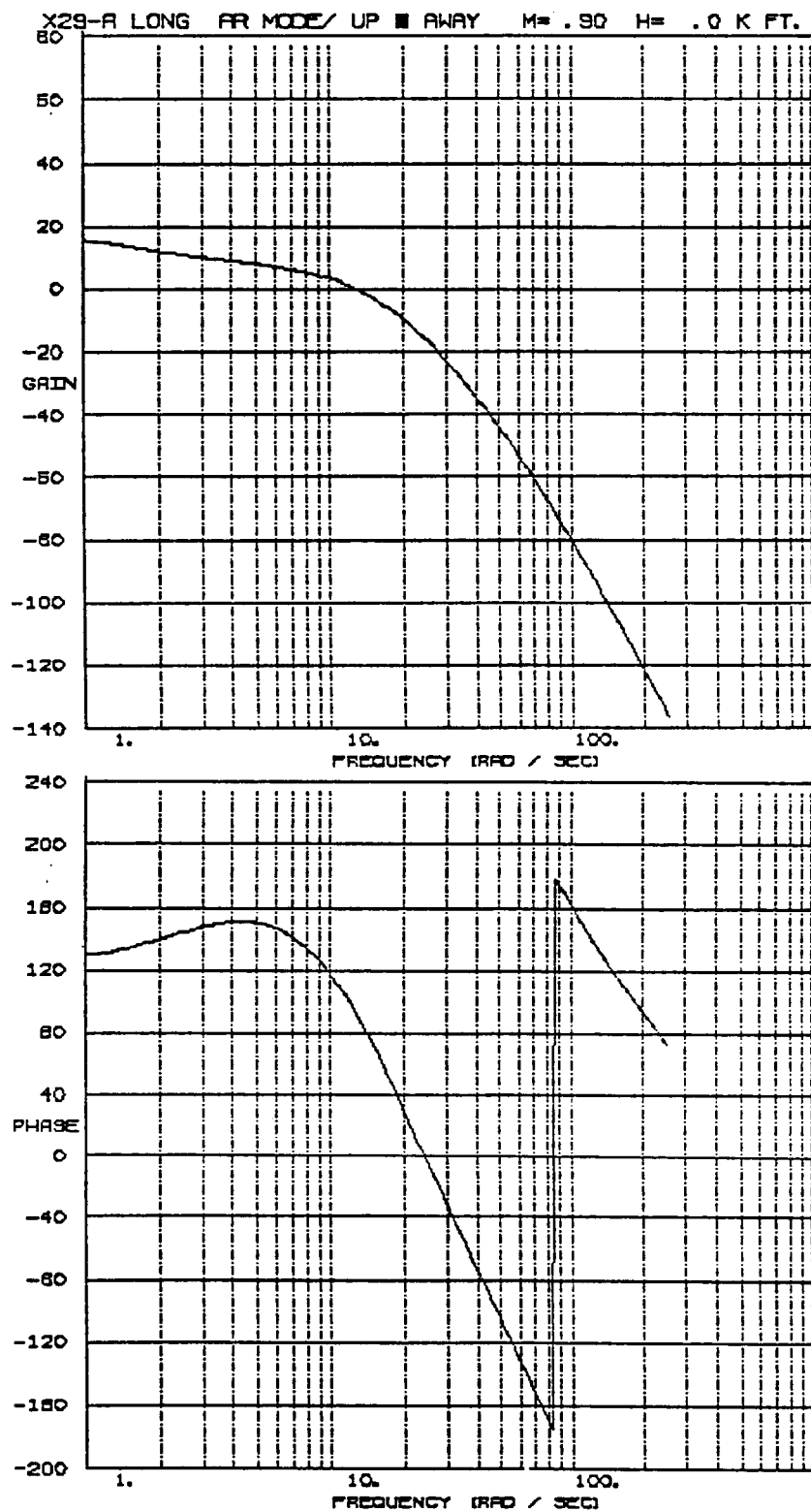


Figure 3.51 STARS Closed Loop Frequency Response for Symmetric X-29A using Analytical Rigid Body Modes from Stick Position to Sensed Pitch Rate, Excluding Notch Filters

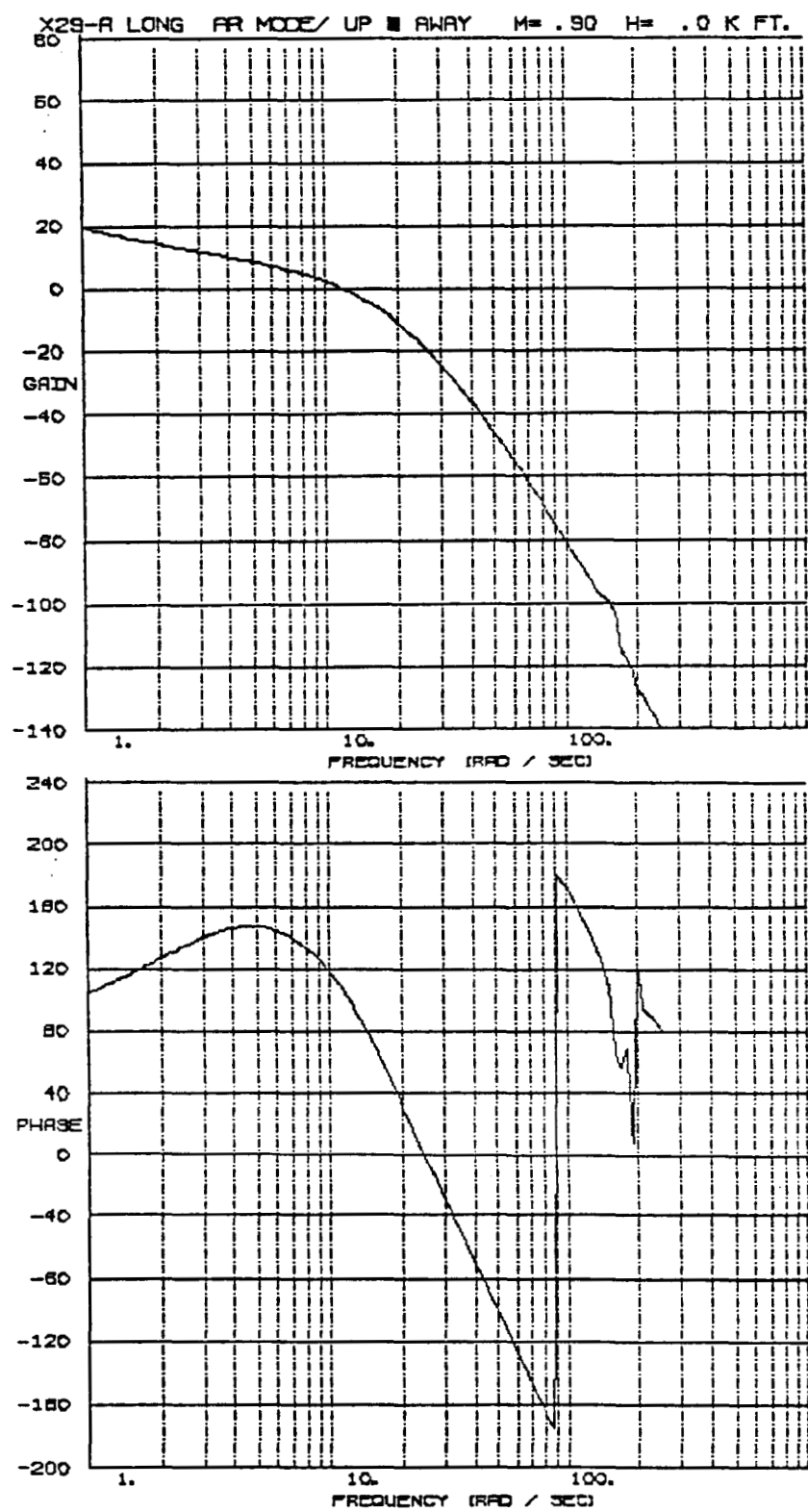


Figure 3.52 STARS Closed Loop Frequency Response for Symmetric X-29A using Analytical Flexible Modes from Stick Position to Sensed Pitch Rate, Excluding Notch Filters

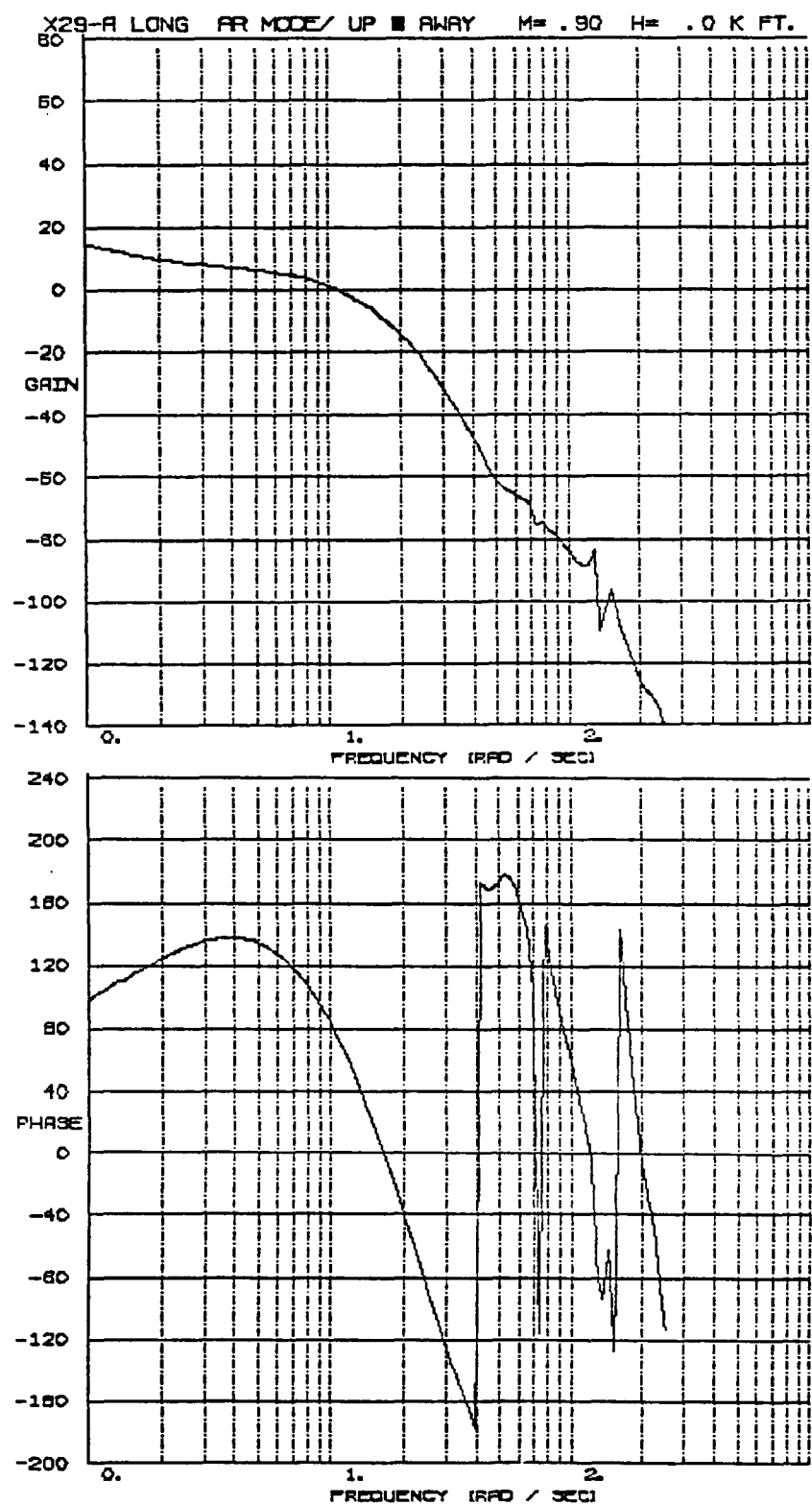


Figure 3.53 Sael Closed Loop Frequency Response for Symmetric X-29A using GVS Flexible Modes from Stick Position to Sensed Pitch Rate, Excluding Notch Filters

4. OBLIQUE WING RESEARCH AIRCRAFT ANALYSES AND RESULTS

4.1 Introduction

The proposed Oblique Wing Research Aircraft's unusual configuration provides the opportunity to study unique aerodynamic and structural problems. Because of the asymmetry associated with oblique wings, aeroelastic behavior and handling qualities are areas which require special consideration. This project starts analyses on the OWRA using the STARS integrated analytical program. Specifically, finite element modeling and free vibration analyses are performed on the OWRA, and the results are discussed in this chapter. Further analyses, such as unsteady aerodynamic calculations, flutter and divergence analyses, and ASE analyses will need to be conducted, however these analyses are not included in this project.

Section 4.2 of this report describes the conversion of the OWRA finite element model from NASTRAN format to STARS format. Also, the validity of the FEM is discussed. In Section 4.3 the approach to reduce the FEM matrix bandwidth is outlined, and the results are discussed. Section 4.4 presents the results of the free vibration analyses.

4.2 The OWRA Finite Element Model

This project started with the arrival of a complete FEM from the NASA contractor working on the OWRA. The FEM data file received was in NASTRAN format, thus the file needed to be converted to STARS format to start the integrated analyses. A computer program, NSTARS, was developed and used in the conversion of the FEM data file. NSTARS is an interactive program written to convert any NASTRAN data file to a format compatible to STARS. After the conversion, the STARS finite element model was thoroughly checked against the NASTRAN data file to ensure no mistakes were made.

The OWRA finite element model consists of a simplified fuselage model (Figure 4.1), a three dimensional pivot pin support structure (Figure 4.2), and a three dimensional wing (Figure 4.3). The complete finite element model (Figure 4.4) consists of 1,380 nodes and 3,897 elements using 32 different material types. The wing uses 757 nodes, while the pivot structure and fuselage use 468 and 152 nodes, respectively. There are 3 third point nodes, making the total of 1,380 nodes. Due to the right wing being swept forward at any skew angle, aeroelastic tailoring of the wing was required, and thus composites were used in the design and analysis of the OWRA FEM. The composites on the STARS FEM were considered anisotropic, and the stiffness of the layers were combined into a single shell.



Figure 4.1 STARS OWRA Finite Element Model of the Fuselage and Empennage

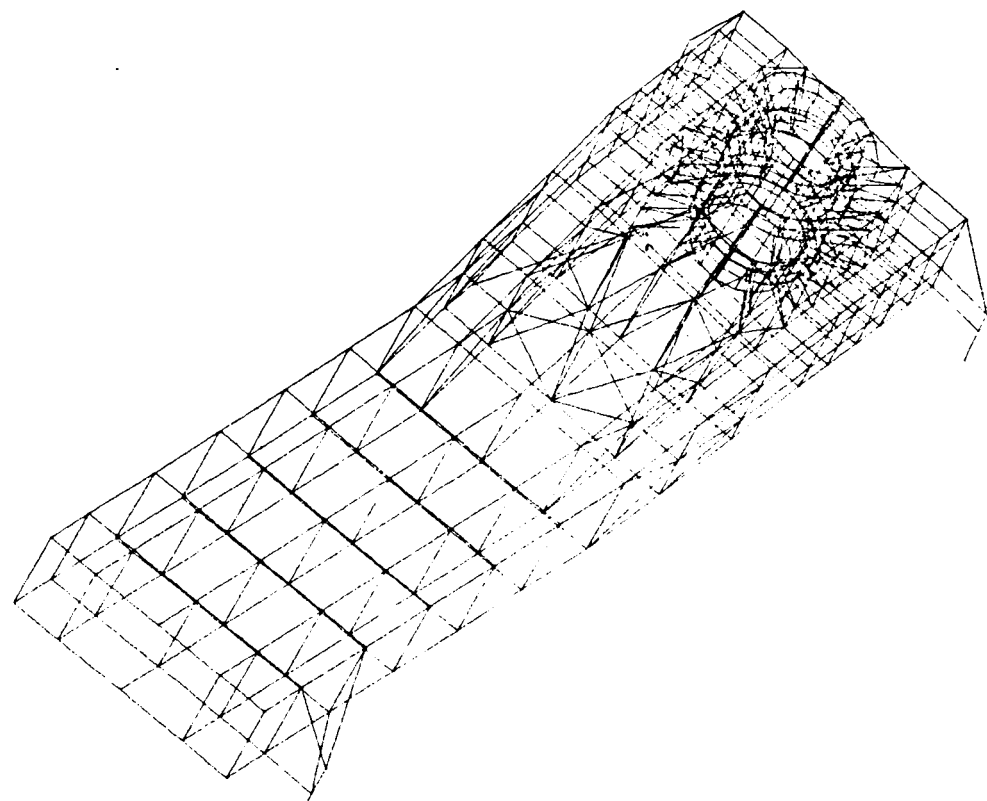


Figure 4.2 STARS OWRA Finite Element Model of the Pivot Structure

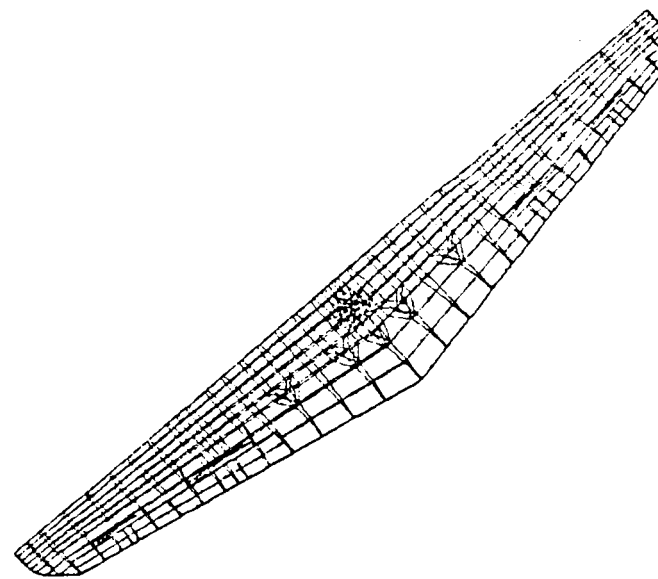


Figure 4.3 STARS OWRA Finite Element Model of the Wing

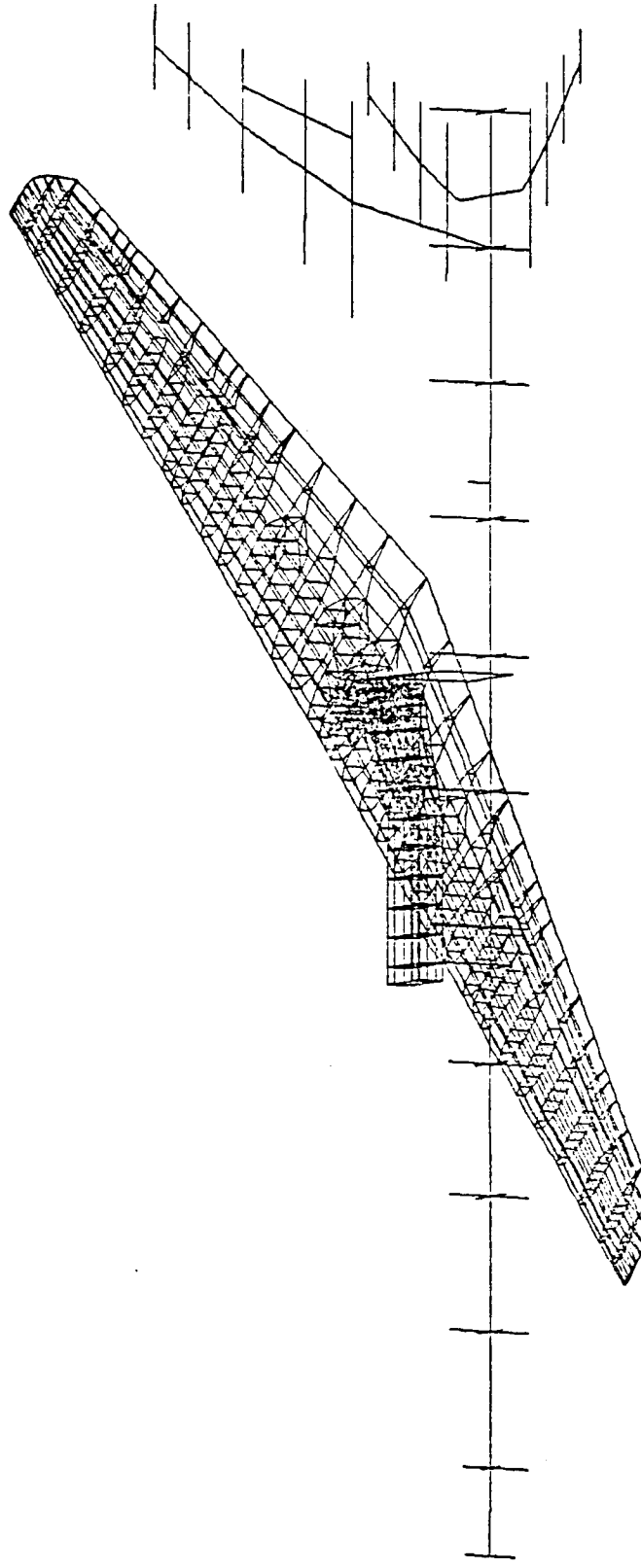


Figure 4.4 STARS Oblique Wing Research Aircraft Complete FEM

At this point, the validity of the STARS FEM was looked into. A simple check of the fuselage was performed to ensure that it was modeled properly. This was achieved by isolating the fuselage and pinning one end to simulate a cantilevered beam. Theoretically, for a cantilevered beam with a load concentrated at the free end, the displacement is proportional to the load. Thus, a simple check for two concentrated loads was performed on the fuselage, and no discrepancies were found. Also, the complete FEM was checked for quadrilateral elements that had a length to width ratio greater than 4:1, as such elements may cause numerical instabilities in the analyses. Several elements were found along the flaps with ratios of approximately 10:1, and necessary corrections were made.

4.3 OWRA Bandwidth Minimization

In this project, the complete FEM was utilized in the structural dynamic free vibration analyses for reasons described below. First, the complete finite element model was used to eliminate any errors associated with the approximate Guyan reduction scheme (see Reference 23) commonly used to reduce the magnitude of the eigenvalue problem in vibration analyses. This reduction scheme was performed by the contractor to arrive at their results given in Reference 9. Second, the highly efficient STARS computer program was deemed feasible for the solution of the OWRA eigenvalue problem, although utilizing the complete FEM results in a 8,262 order problem.

The solution of very large order eigenvalue problems poses many problems, one of which is long solution times. The STARS solution time of the structural eigenvalue problem increases as the square of the half-bandwidth, where the half-bandwidth is given in Equation 4.1.

$$\text{half-bandwidth} = ((n_j - n_i) + 1) * 6 \quad (4.1)$$

where n_j and n_i represent the highest and lowest connected node numbers. To make efficient use of computer CPU time, an attempt to minimize the bandwidth of the complete FEM was performed. Although the STARS program has a minimization scheme, it was deemed helpful to carefully number the nodes by hand with minimum bandwidth in mind. In

earlier oblique wing finite element models, the bandwidth increased dramatically unless particular attention was paid to the wing numbering. Thus, the nodes on the wing were renumbered as described below.

The minimization scheme of the STARS program achieved a half-bandwidth of 648, or a maximum difference of 107. Using this as a guideline, the nodes on the wing were renumbered, alternating wing tips, working towards the pivot substructure. After considerable work, the maximum difference of connecting nodes on the wing was 84, giving a half-bandwidth of 510. This would have reduced the solution time by about 40%. The pivot and fuselage numbers were then renumbered consecutively, corresponding to their original numbers. The STARS program was then run to determine the half-bandwidth, and the result was 1,248. Thus, a node numbering problem was found to be in the pivot substructure. An attempt to renumber the nodes on the pivot below a maximum difference of 107 was performed. However, due to the complexity of this structure, a lower bandwidth was not achieved. As a result, the original node numbering was kept, and the half-bandwidth was 648.

4.4 OWRA Free Vibration Results

The OWRA free vibration analyses utilizing the complete FEM were performed via the STARS program. Since the FEM is not symmetric, both the symmetric and anti-symmetric analyses had to be performed simultaneously on the OWRA. The solution of this large eigenvalue problem proved to be very time consuming, causing a time extension of this project. Several problems contributed to the delays, such as computer management problems (of the NASA VAX 11-750), debugging of the STARS code, and the actual solution of the eigenvalue problem. The first attempts at the solution resulted in several errors in the STARS computer program. The errors turned out to be storage and memory requirement problems, and were easily corrected. However, tracing the errors took approximately one month of continuous debugging effort. With the errors corrected, new attempts to solve the eigenvalue problem were conducted. Due to the length of time required to compute the solution, several more problems arose, particularly with the computer management. Problems such as air conditioning failures and constant system

crashes delayed the results even further. The problems were eventually corrected, and results of a limited free vibration analysis were finally obtained, as described below.

Due to the problems which occurred in the free vibration analysis, a limited eigenvalue solution was ran on the OWRA. The OWRA structural analysis eigenvalue problem was solved by the STARS analytical program using the Sturm sequence and inverse iteration technique (see Reference 1). The Sturm sequence may be used to locate any individual or group of eigenvalues between a lower and upper bound (Reference 24). The free vibration analysis performed gave eigenvalues between the upper and lower bounds of 100 rad/sec and 12 rad/sec, respectively. The results are summarized in Table 4.1.

The results of the STARS free vibration analysis display a similar pattern of eigenvalues, as compared to the results of the Guyan reduced FEM analysis in Reference 9. The mode shapes, however did not correlate well, and refinement of the STARS FEM is needed before continuing the analyses. Due to limited time, the refinement process was not included in this project.

Table 4.1 Results of the OWRA Free Vibration Analysis

<u>STARS Mode</u>	<u>Frequency (Hz)</u>
24	3.467
25	6.006
26	8.498
27	8.498

5. PROJECT MANAGEMENT

5.1 Introduction

The Master of Engineering (M.E.) program at the University of Kansas requires the candidate to assume specific technical and managerial responsibilities of a major project. These responsibilities, which are attained on this project, are delineated in this chapter. The overall objective of this M.E. project is to study the integration of structures, aerodynamics, and controls on two advanced airplane configurations. Due to the increasing design of highly flexible structures using high gain flight control systems, such integrated analyses are becoming important to ensure flight safety. This project accomplishes the integrated study with the use of the integrated numerical STARS program at NASA Dryden Flight Research Facility.

5.2 Project Management

This M.E. project is a joint program between NASA Ames Research Center (NASA-ARC) and the University of Kansas Center for Research, Incorporated (CRINC). The project was initiated by the principal investigator, Dr. Paul E. Fortin, Director of the M.E. program at the University of Kansas, and started with the issuance of a grant from NASA-ARC to CRINC. The research and analyses were performed at NASA Ames DFRF in the Vehicle Technology Branch of the Research Engineering Division. The organizational structure showing the relationship of NASA-ARC to the Vehicle Technology Branch is shown in Figure 5.1.

At NASA DFRF, this candidate performed as the manager of the project described here under the supervision of Dr. Kajal K. Gupta. The responsibilities included project planning and scheduling, and supervising and coordinating the different groups and individuals involved with this project. Figure 5.2 shows the organization of these groups and individuals in relation to this project. A brief description of each follows.

**ORIGINAL PAGE IS
OF POOR QUALITY**

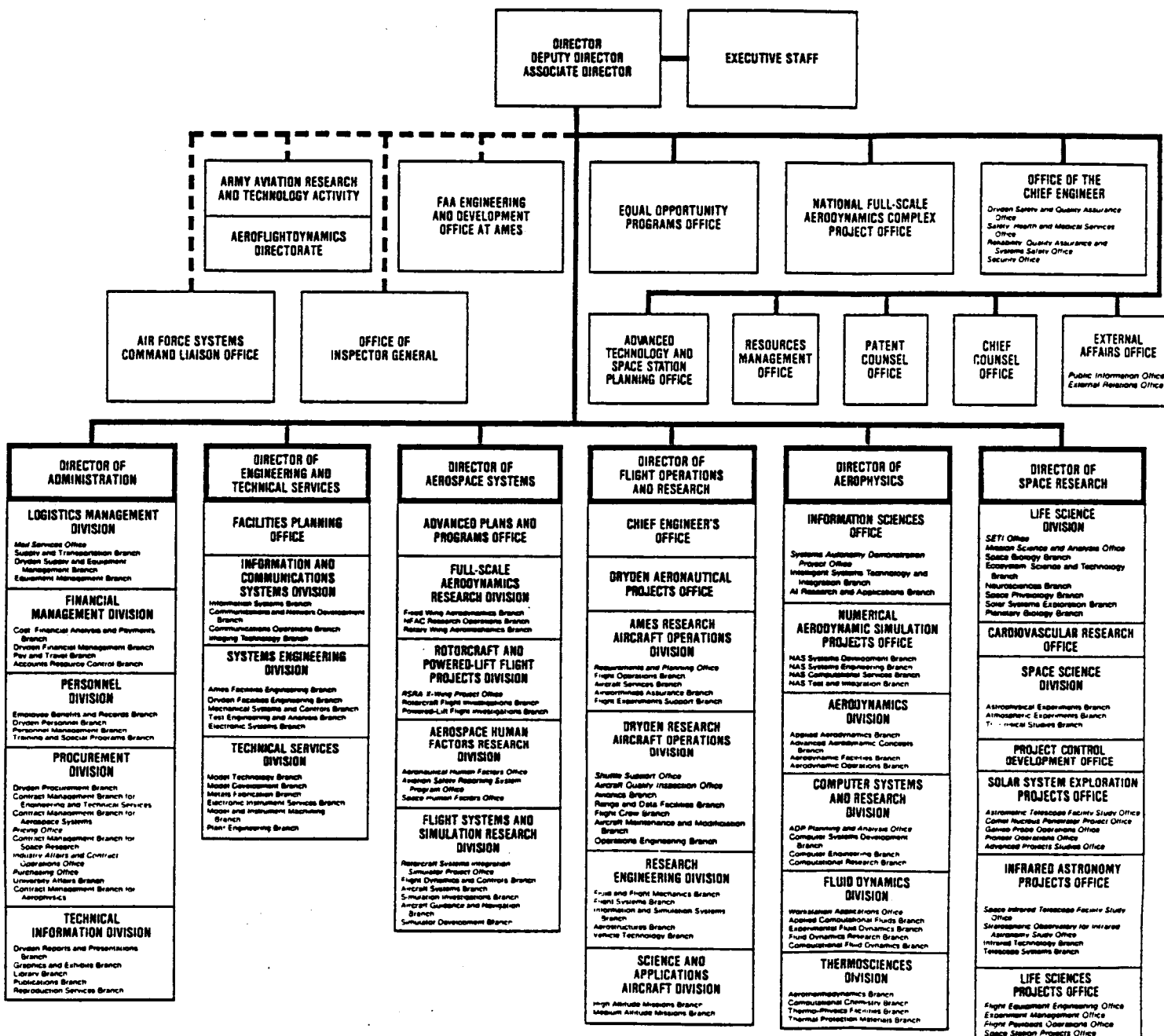


Figure 5.1 NASA Ames Research Center Organizational Chart

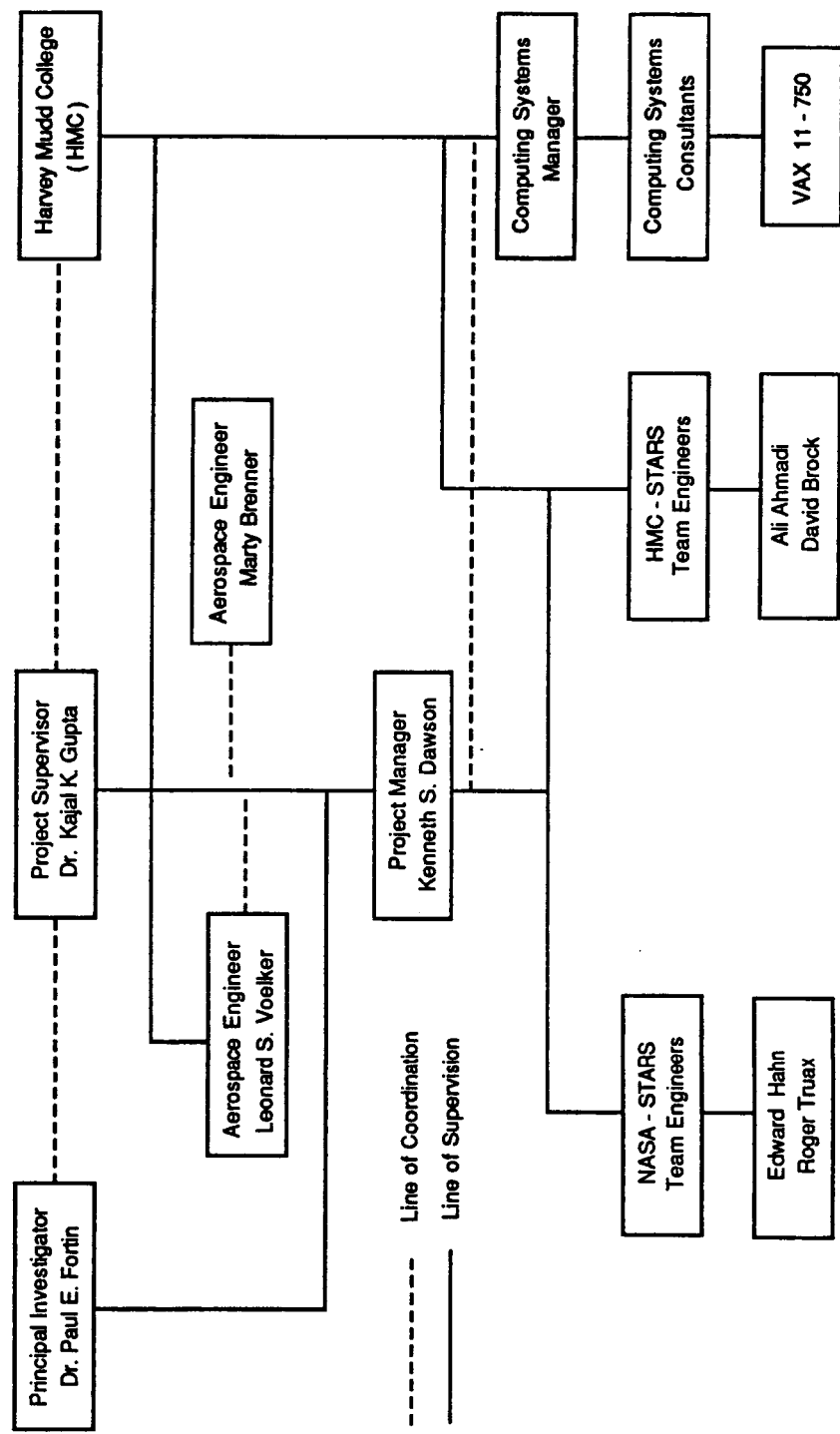


Figure 5.2 Project Management Organization

As stated earlier, the principal investigator is Dr. Paul Fortin. Dr. Fortin provided the administrative and financial direction of the grant, and acted as liaison between CRINC and NASA-ARC, as seen from the communication/coordination line on Figure 5.2. Dr. Kajal K. Gupta, the technical officer and project supervisor, provided the guidance for this project, a section of the STARS project. Harvey Mudd College (HMC) in Claremont, California was under contract to NASA-ARC, also under the supervision of Dr. Gupta. HMC provided professional personnel and staff to support the STARS project, and staff to maintain the NASA VAX 11-750 computer kept at the college. The personnel working on the STARS - Team is also shown in Figure 5.2 Mr. Leonard Voelker, a senior NASA Aerospace Engineer, provided guidance in the development of the X-29A aerodynamics model, and interpretation of the aerodynamic analytical results. Mr. Marty Brenner, a NASA Aerospace Engineer in ASE controls, provided the tools and guidance for the controls analyses. There are various others working on the STARS project, however, only those directly involved on this project are listed. Mr. Ali Ahmadi, a graduate student at the University of Kansas, along with Aerospace Engineers at NASA, Mr. Edward Hahn and Mr. Roger Truax, performed the X-29A finite element and aerodynamic modeling, and completed the vibration analysis. Mr. Hahn and Mr. Truax continued at NASA with the assistance of the aerodynamic and control analyses. Mr. Ahmadi provided technical guidance and was the STARS programming specialist. Mr. David Brock at HMC worked on programming used in the preparation of the OWRA FEM. Also working on this project under supervision were summer hires at NASA DFRF.

Management of the STARS - Team personnel involved no problems, since all were engineers, and quite professional. Little supervision was necessary, and motivation was high. Conflicts, however, did arise in the management of computer resources. There was no direct supervision line from the project manager to the computer systems at HMC, except to back up through the channels. Two specific problem areas were noticed. First, the hours worked by the college staff varied significantly from the NASA staff. Thus, as a result, it could take as long as two hours to inform the computer systems manager of any problems. The second problem area involved the motivation of computer systems staff. Most of the HMC computer staff was very helpful, however, at times it would take repeated instructions and constant supervision to accomplish a task. To accommodate, different management techniques had to evolve for the supervision of the project, as is often done

in project management. Also, the delays were simply managed around, as several tasks were planned to fall back on in case of computer problems. However, constant computer problems close to the end of the project did cause some time delays, as explained in Chapter 4.

5.3 Project Scope and Scheduling

The objective of this project, as stated earlier, is to study the integration of structures, aerodynamics, and controls on two advance airplane configurations, the FSW X-29A and the OWRA. The tasks involved in this are listed briefly below.

1. Review of X-29A finite and aerodynamic modeling, and vibration analysis.
2. Flutter analyses of the symmetric and anti-symmetric X-29A using the k and p-k methods (note anti-symmetric p-k analysis added from proposal, Ref. 23).
3. Flutter analyses of the symmetric and anti-symmetric X-29A via the ASE or state-space method.
4. Aerovielastic controls analyses of the symmetric X-29A for the analog reversion mode. Comparison of STARS results to existing results.
5. Finite element modeling of the OWRA, including conversion of NASTRAN model to STARS model, renumbering of nodes, and checking the numerical validity of the model.
6. Free vibration analysis of the OWRA.
7. Project final report write up.

The schedule of these tasks is shown in Figure 5.3 comparing the proposed schedule (Ref. 25) along with the actual schedule. The actual schedule shows an extension granted to this project. The extension became necessary when problems arose in the vibration analysis of the OWRA. These problems included unexpected delays from debugging programs, and from computer system crashes.

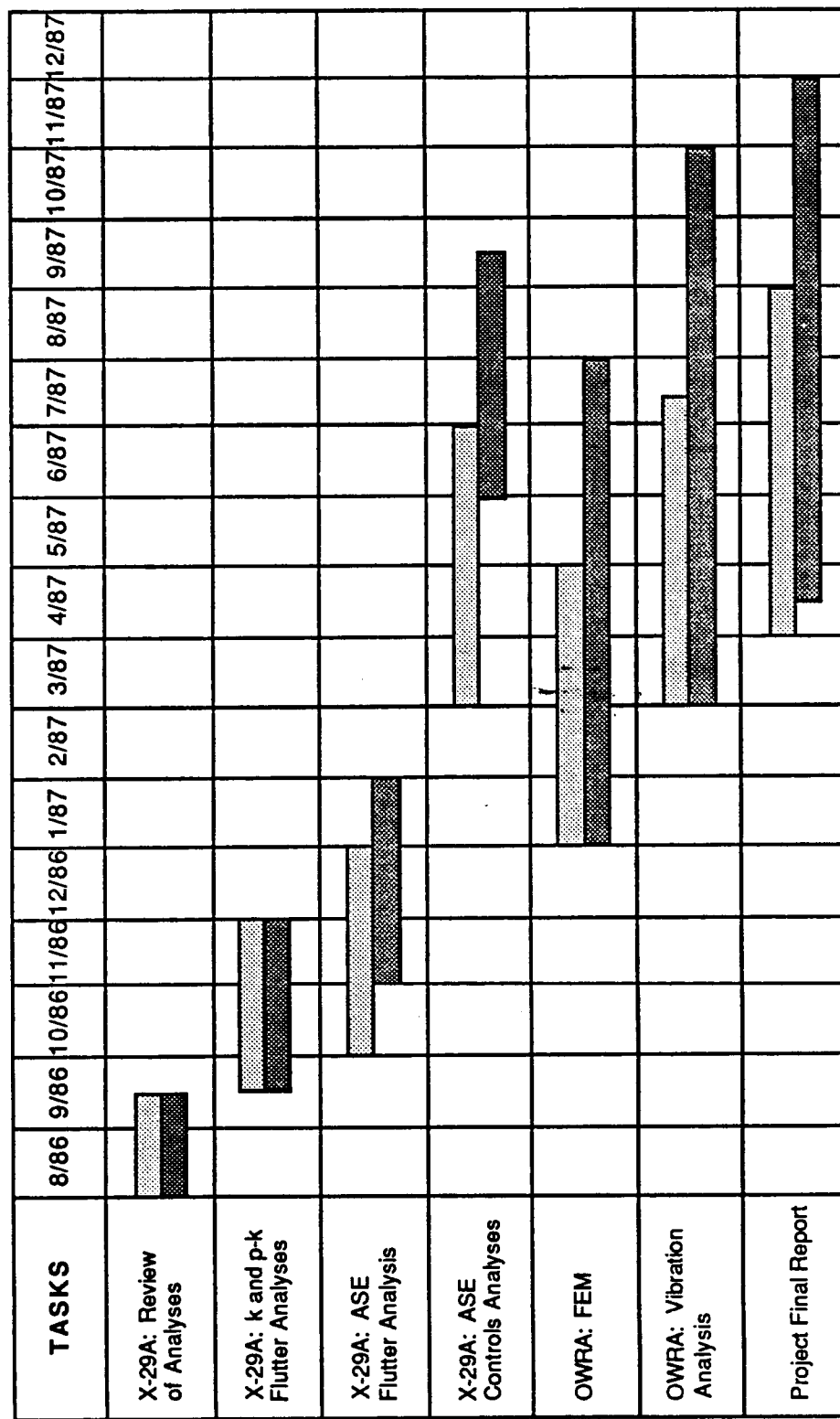


Figure 5.3 Project Schedule, Proposed () and Actual ()

5.4 Project Budget

The initial budget for this grant was negotiated by the University of Kansas Center for Research, Inc. with NASA Ames Research Center. Table 5.1 shows the breakdown of the initial budget, which totaled \$44,050. One major difference between the actual and proposed budget is that the 4 months of 50% time at \$1200/month was changed to 1.5 months of 100% at \$1600/month. This time was initially planned to finish course work at the University of Kansas, however, since there was no need for this, and due to experienced delays, the extra time was spent at NASA DFRF to continue research. This change in the budget and schedule drained the monetary sources, leaving no funds for return travel or miscellaneous costs. Thus, a one and one-half month cost extension of \$4,000 was negotiated between CRINC and NASA-ARC. This extra time was spent doing research for NASA at the Dryden Flight Research Facility, and working out problems from the experienced delays. The supplemental budget for the extension is shown in Table 5.2.

Table 5.1 Initial Project Budget

DIRECT COSTS

Salaries & Wages

Administrative Support	\$ 1,800
Graduate Student	
50% for 7 months (1/1/86 - 7/3/86) @ \$1100/month	3,850
100% for 13 months (8/1/86 - 8/31/87) @ \$1600/month	20,800
50% for 4 months (9/1/87 - 12/31/87) @ \$1200/month	2,400
(100% for 1 1/2 months (9/1/87 - 10/15/87)	
Total Salaries & Wages	\$28,850

Fringe Benefits

19% Administrative	342
13% for 13 months	2,704
1% for 11 months	63

Other Direct Costs

Student moving and travel	1,300
Faculty/Technical Advisor travel	600
Tuition	1,800
Publication, Miscellaneous	300
Total Direct Cost (TDC)	\$35,959

INDIRECT COST @ 22.5% OF TDC 8,091

TOTAL COST: \$44,050

Table 5.2 Supplemental Budget

DIRECT COSTS

Salaries & Wages

Graduate Student
100% for 1 1/2 months (10/15/87 - 11/30/87) @ 1600/month \$ 2,400

Fringe Benefits

13% for 1 1/2 months 310

Other Direct Costs

Student travel (for presenting research results) 490

Total Direct Cost (TDC) \$ 3,200

INDIRECT COST @ 25% OF TDC 800

TOTAL COST: \$ 4,000

6. CONCLUSIONS AND RECOMMENDATIONS

6.1 Project Review

This project has encompassed a study of structures, aerodynamics, and control integration on two advanced airplanes, the Forward Swept Wing X-29A, and the Oblique Wing Research Aircraft. This project was accomplished at NASA Dryden Flight Research Center using the integrated analytical program, STARS. The analyses presented were performed by the candidate and the STARS - Team in a project environment, which well suits the requirements of the Master of Engineering program at the University of Kansas. Specifically, the environment at NASA has given the candidate the opportunity to work in a group, as well as to supervise the progress of this project. The division of each task is delineated below, showing the technical and supervisory skills used.

The tasks performed on the X-29A included finite element modeling, free vibration analysis, subsonic unsteady aerodynamic calculations, flutter and divergence analyses, and an aeroservoelastic controls analysis. The finite element modeling and symmetric/anti-symmetric free vibration analyses were performed by the STARS - Team prior to the start of this Master's project. However, to continue the integrated analyses for this project, this work was reviewed extensively. The unsteady aerodynamic calculations were performed as a group effort by this candidate and the STARS - Team. Specifically, unsteady aerodynamics analyses were performed by the STARS - Team, however, after review of the aerodynamic model, necessary changes were implemented, and further analyses were ran as a group effort. The flutter and divergence analyses included three different solution techniques, the k, p-k, and state-space methods. The k method analyses were performed on the symmetric and anti-symmetric X-29A as a group effort, with this candidate supervising the analyses pertaining to this project. The p-k and state-space techniques were performed on the symmetric and anti-symmetric cases as an individual effort. The ASE controls analysis was performed as a group effort.

The tasks performed on the OWRA included conversion of a NASTRAN finite element code to STARS code, finite element modeling, and free vibration analyses. The conversion

of the finite element model was performed as a group task. Specifically, this candidate supervised the development of the Fortran code for the conversion program, and the conversion of the finite element code, itself. The finite element modeling, i.e., the attempt to reduce the bandwidth, and the checking of the validity of the model was performed as an individual task by this candidate. Also, the free vibration analyses were performed as an individual task, however, debugging of the STARS code was done as a group effort.

Thus, this candidate has applied both extensive technical and supervisory skills on this project. The conclusions and recommendations reached as a result of the work described above are given below for the X-29A and the OWRA.

6.2 X-29A Conclusions

The exhaustive analyses and flight test results compiled on the X-29A has provided the opportunity to compare the results of the STARS integrated analytical program. In this report, comparisons of the STARS free vibration analyses, flutter/divergence analyses, and aeroservoelastic control analyses were made to existing verified tests or analyses. The conclusions and recommendations are listed below.

- 1) The STARS symmetric and anti-symmetric free vibration analyses showed good correlation to the Grumman Aerospace Corporation (GAC) results, and to the ground vibration survey. The STARS and GAC analyses, however, did not identify the noseboom (NB) mode at 20.5 Hz since neither finite element model included this structure.
- 2) With good correlation of eigenvalues and eigenvectors to the GVS, unsteady aerodynamic calculations were performed using a doublet lattice technique. Utilizing the calculated force, stiffness, and mass matrices, flutter and divergence analyses were then performed for the symmetric and anti-symmetric cases via the k, p-k, and state-space techniques.
- 3) The symmetric X-29A flutter and divergence results showed good correlation of the state-space and p-k techniques to the k-method. The p-k and k methods displayed

damping approximately of the same magnitude. The state-space method damping term was generally somewhat different than the k and p-k method, which is attributable to the fact that the proportional term of g, α/β (real part over the imaginary part of the eigenvalue solution) is plotted for the state-space method.

- 4) The anti-symmetric flutter and divergence analyses showed good correlation between the state-space and k methods. The p-k method, however, varied significantly to the k method, probably indicating some numerical instability associated with the aerodynamic model. The inclusion of the rigid body modes in the anti-symmetric case indicates that the lower frequency flexible modes are affected, as illustrated by both the v-g plots and the root locus plots.
- 5) The root locus plots indicate the same pattern of the modes for all flutter/divergence methods. The state-space and p-k methods, however, differ from the k-method in that the divergent modes exhibit non-oscillatory motion prior to divergence.
- 6) In the aeroservoelastic controls analyses, good correlation is shown for both the open and closed loop analog reversion mode between the STARS analytical results and the SAEL results, which uses test data from the GVS. The SAEL results however do indicate more response at the airframe's natural frequencies. Particularly, in the open loop analysis excluding the notch filters, the STARS results do not indicate any instabilities, unlike the SAEL results. The instability occurring at the noseboom frequency does not occur in the STARS analyses since this structure was not included in the FEM.
- 7) The STARS and SAEL results both meet the criteria of gain margins of ± 3 dB and phase margins of 22.5 deg for all system modes below the first structural mode. Also, no gain crossovers occur at airframe resonances, and show a gain margin of at least 6 dB.
- 8) Good correlation of STARS analytical closed loop damping and frequency results were shown to flight test results performed at NASA.

6.3 Proposed Future Research for the X-29A

Based on the above conclusions and general findings while working on this project, the following recommendations are made concerning the FSW X-29A.

- 1) Further analyses should be run to determine if there is a theoretical factor relating the damping term of the state-space analyses (α/β) to the k and p-k analyses (g).
- 2) The anti-symmetric X-29A p-k flutter analysis should be investigated further to determine the cause of the varying results (as compared to the k and state-space methods).
- 3) The STARS X-29A FEM should be updated to include the noseboom structure. Free vibration analyses, followed by a complete ASE analysis should be conducted to match the instability indicated by the SAEL open loop analyses.

6.4 OWRA Conclusions

The analyses performed on the Oblique Wing Research Aircraft for this project included the conversion of a complete NASTRAN finite element model to STARS format. This also included minor checks of the validity of the FEM. A free vibration analysis of the complete FEM was performed on STARS using the Sturm sequence and inverse iteration method. The conclusions of this work are given below.

- 1) A 1,380 node finite element model was used in the free vibration analysis of the Oblique Wing Research Aircraft. This resulted in a 8,262 degrees of freedom eigenvalue problem. The complete FEM was used to eliminate approximation errors of reduction schemes. This approach seemed feasible since the highly efficient STARS was being used.

7. REFERENCES

1. Gupta, K. K., "STARS--A General-Purpose Finite Element Computer Program for Analysis of Engineering Structures," NASA RP-1129, October, 1984.
2. Gupta, K. K., Brenner, M. J., and Voelker, L. S., "Integrated Aeroviscoelastic Analysis Capability with X-29A Analytical Comparisons," AIAA Paper 81-0907-CP, April 1987.
3. Taylor, R. F., Miller, K. L., and Brockman, R. A., "A Procedure for Flutter Analysis of FASTOP-3 Compatible Mathematical Models, Volume I -- Theory and Application," AFWAL-TR81-3063, June 1981.
4. Dunn, H. J., "An Analytical Technique for Approximating Unsteady Aerodynamics in the Time Domain," NASA TP-1738, November, 1980.
5. Weiss, S. J., Tseng, K., and Morino, L., "State-Space Formulations for Flutter Analysis," AIAA Paper 77-177, Presented at AIAA 15th Aerospace Sciences Meeting, Los Angeles, California, January 24-26, 1977.
6. Sefic, Walter J., and Maxwell, Cleo M., "X-29A Technology Demonstrator Flight Test Program Overview," NASA TM-86809, May 1986.
7. Abel, Irving, "An Analytical Technique for Predicting the Characteristics of a Flexible Wing Equipped With an Active Flutter-Suppression System and Comparison with Wind-Tunnel Data," NASA TP-1367, February 1979.
8. Whitaker, A., and Chin, J., "X-29 Digital Flight Control System Design," AGARD Paper CP No. 384, presented at the AGARD Symposium on Active Control Systems, Toronto, Canada, October, 1984.
9. Rockwell International North American Aircraft Operations, "Oblique Wing Research Aircraft Phase B Preliminary Design," Contract NAS2-12229, Draft for Final Report for Period November 1985 - November 1986, NA-87-1033, April 15, 1987.
10. Barber, Marvin R., DeAngelis, V. M., and Traskos, Robert L., "F-8 Oblique-Wing Research Aircraft--A Progress Report," Paper presented at Society of Flight Test Engineers, 17th Annual Symposium, August 11, 1986.
11. Jones, R. T., "Reduction of Wave Drag by Antisymmetric Arrangement of Wings and Bodies," AIAA Journal, Vol. 10, No. 2, February 1972, pp. 171-176.
12. Roukis, Dean, J., "X-29 Ground Vibration Survey Results and Subsonic Flutter Analysis," Grumman Aerospace Corporation report 712-ENG-RPT-84-049, November 1, 1984.

13. Grumman Aerospace Corporation, FASTOP Workshop Manual, Volume I - Theory, Grumman Aerospace Corp., Bethpage, New York.
14. Blisplinghoff, Raymond L., Ashley, Holt, and Halfman, Robert L., *Aeroelasticity*, Addison-Wesley Publishing Company, Inc., 1955.
15. Hassig, Hermann J., "An Approximate True Damping Solution of the Flutter Equation by Determinant Iteration," *Journal of Aircraft*, Vol. 8, No. 11, November 1971, pp. 885-889.
16. Crittendon, J. B., Weisshaar, T. A., Johnson, E. H., and Rutkowski, M. J., "Aeroelastic Stability Characteristics of an Oblique Wing," *Journal of Aircraft*, Vol. 15, No. 7, July 1978, pp. 429-434.
17. Lawrence, A. J., and Jackson, J. P., "Comparison of Different Methods of Assessing the Free Oscillating Characteristics of Aeroelastic Systems," British Aeronautical Research Council, Current Paper No. 1084, December 1968.
18. Gupta, K. K., Brenner, M. J., and Voelker, L. S., "Development and Application of an Integrated Aerosservoelastic Analysis Program," NASA TP (In Press).
19. Chin, J., Chacon, V., and Gera, J., "X-29A Flight Control System Performance During Flight Test," Grumman Aerospace Corporation, 1987.
20. Military Specification MIL-F-9490D, Flight Control Systems--Design Installation and Test of Piloted Aircraft, General Specification, Rev D, June 6, 1975.
21. Military Specification MIL-A-8870B, Airplane Strength and Rigidity Vibration, Flutter, and Divergence, Rev B, May 20, 1987.
22. Zislin, A., Laurie, E., Wilkinson, K., and Goldstein, R., "X-29 Aerosservoelastic Analysis and Ground Test Validation Procedures," AIAA Paper 85-3091, Presented at AIAA Aircraft Design Systems and Operations Meeting, Colorado Springs, Colorado, October 14-16, 1985.
23. Guyan, Robert J., "Reduction of Stiffness and Mass Matrices," *AIAA Journal*, Vol. 3, No. 2, Feb. 1965, p. 380.
24. Wilkinson, J. H., *The Algebraic Eigenvalue Problem*, Oxford University Press, London, 1965.
25. Dawson, Kenneth S., "Proposal to the Aerospace Engineering Department for Master of Engineering Project," University of Kansas, Lawrence, Kansas, March 1987.